Simulation Informed Machine Learning Interpretation of Electrochemical Measurements

Giang Tra Le

A dissertation
submitted in partial fulfillment of the
requirements for the degree of

Doctor of Philosophy

University of Washington

2023

Reading Committee:

Stuart Adler, Chair

David A. C. Beck

Daniel T. Schwartz

Program Authorized to Offer Degree:

Chemical Engineering

University of Washington

Abstract

Simulation Informed Machine Learning Interpretation of Electrochemical Measurements

Giang Tra Le

Chair of the Supervisory Committee:
Stuart Adler
Chemical Engineering

This work resides at the intersection of rigorous physics-based simulation and machine learning. We seek to address problems that have complicated multiphysics and exist in vast parameter spaces. Where the data requirement for machine learning methods can make the experimental burden untenable and the time-sensitive nature or high computational cost limits the practicality of mechanistic physics model. Our overarching objective is to explore solutions to bridge these limitations in electrochemistry research through the integration of machine learning and mechanistic simulation.

Failure detection in solid oxide fuel cell (SOFC) is complicated due to the need to disentangle the failure response from the effect of degradation - gradual change in performance with aging. We used physics models to simulate the behavior of SOFC under three failures that could occur during its operation: fuel maldistribution, delamination and oxidant gas crossover. These simulations revealed deviations in electrochemical impedance spectroscopy (EIS) from behavior of standard circuit elements under failures, underscoring the significance of physics-based modeling in SOFC diagnostics. Leveraging synthetic data of a 6-cell substack, we trained a support vector machine to identify failure modes with a 90% accuracy across degradation effects and operating conditions, discerning imperceptible differences in stack-level EIS responses. Investigation of synthetic data offered insights to failure diagnosis with EIS in determining most responsive frequency range and the efficacy of different

machine learning methods.

In the second project, we reexamined the utility of a reference electrode positioned outside the current path on a thin solid electrolyte. Extensive prior research with this design had demonstrated significant polarization shifts and half-cell EIS distortions from minor electrode misalignment, limiting its usefulness in quantitative assessment of two half-reactions. Employing a physics model to simulate these behaviors in a proton-exchange membrane electrolyzer, we trained a neural network model with simulated data to deconvolute edge effects and determine the true oxygen kinetic overpotential with high accuracy (r^2-score $\geqslant 0.96$). Validation with experimental data from electrolyzer cells of varying membrane thicknesses and misaligned electrodes confirmed the breakdown of oxygen and hydrogen evolution reaction losses to align with literature values. These findings unveil the potential use of this straightforward reference electrode design and intentional anode-cathode misalignment for evaluating individual electrode kinetics in performance or long-term degradation studies.

TABLE OF CONTENTS

LIST OF FIGURES

ACKNOWLEDGMENTS

I am grateful to many who have been part of my graduate school experience over the last five years. I thank the reading committee, Stuart Adler, Daniel Schwartz, and Dave Beck, whose feedback and passion helped me completing this journey.

I add to my appreciation of Stuart Adler for his ample guidance, patience, and support. I am more capable in various avenues of engineering, thanks to the opportunity he gave me to learn, to understand, and to do. I thank him in advocating for my year-long internship at Electric Hydrogen, where I can make good use of the skills and knowledge I have gained.

I thank my lab members: Jon, Brian, Isaac, Anthony, and Maria, for their works and equipment I benefited from, the helpful ideas, and the wisdom they've shared. For the enjoyable time I had in Seattle, I thank them and other friends: Kevin, In, Shri, Jacob, Shripathi, David, Luke, Sage, Kacper.

I thank my collaborators at UC Irvine, Luca Mastropasqua and Jack Brouwer, and collaborators at NREL, Chaiwat Engtrakul, Sarah Blair and Elliot Padgett. I'm indebted for their brilliance, kind hospitality, and hard work.

I thank Electric Hydrogen for the wonderful internship experience and the opportunity to collaborate on reference electrode research with NREL. Many thanks to my many mentors and friends at Electric Hydrogen, who made the year I spent with them incredibly fun and rewarding.

My utmost thank to those closest to me:

To my loving mom and dad, I could not be the person I am today without your hard work, teachings, endless trust and support. For giving me the opportunity to pursue dreams on foreign land, I'm forever indebted.

To my sister, for caring for our family and supporting us, in my presence and in my absence.

To my best friend, Hanh Nguyen, for always listening and sympathizing.

To my amazing partner, Kristian, for being challenging and accepting. The joy you brought has helped me through the toughest moments on this journey.

DEDICATION

To Kristian:

It would have been possible without you, but so much better with.

Chapter 1

INTRODUCTION

This dissertation encompasses two bodies of work that are accompanied with their own motivation and in-depth review of related research. This chapter introduces the fundamental concepts of electrochemical impedance spectroscopy (EIS), background and motivation of the application of mechanistic modeling and machine learning in electrochemistry.

1.1 Electrochemical Impedance Spectroscopy

Electrochemical Impedance Spectroscopy (EIS) is a commonly used characterization technique for studying electrochemistry system.[1–3] It works by applying a sinusoidal excitation signal to the current or voltage while monitoring the response voltage or current signal. In galvanostatic (current-controlled) EIS experiment, the applied input current can be expressed as $\widetilde{I}(t) = \Delta I cos(\omega t)$, where ΔI is the perturbation amplitude, and ω is the perturbation angular frequency. The resulting voltage response can be expressed as $\widetilde{V}(t) = \Delta V cos(\omega t + \theta)$, where ΔV is the voltage response perturbation amplitude, and θ is the phase shift from the excitation signal. The relationship between input and output signals as a function of the input frequency, ω, is defined as the impedance:

$$Z(\omega) = \frac{\widetilde{V}(t)}{\widetilde{I}(t)} = \frac{\Delta V cos(\omega t + \theta)}{\Delta I cos(\omega t)}. \tag{1.1}$$

The impedance, $Z(\omega)$, can be written in the polar coordinates with its magnitude and phase, $Z(\omega) = |Z(\omega)|e^{j\theta}$ or in the Cartesian coordinates as corresponding real and imaginary components, $Z(\omega) = Z'(\omega) + jZ''(\omega)$, where j is the imaginary unity. The impedance of electrochemical system is frequency dependent and often represented by a Nyquist plot,

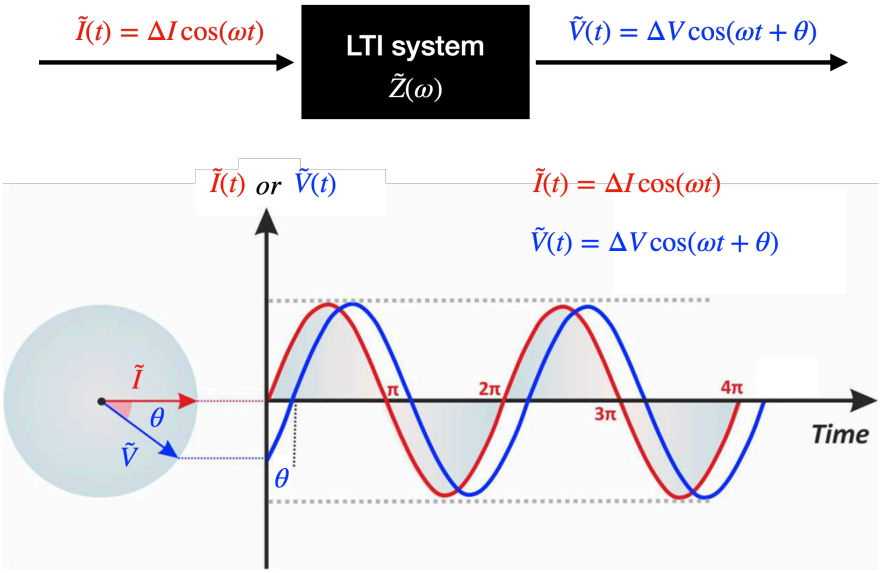

Fig. 1.1 EIS concept schematic. A linear time-invariant (LTI) system impedance response can be analyzed by the input current ($\tilde{I}(t)$) and voltage signals ($\tilde{V}(t)$). Adapted from Lazanas & Prodromidis under the Creative Commons License CC-BY-NC-ND 4.0.[4]

where the negative imaginary component, $-Z''$, is plotted against the real component, Z'. Figure 1.2 shows a common setup to measure the impedance of a working electrode and the EIS Nyquist representation. The EIS results of this system can be used to assess quantitatively the liquid electrolyte resistance (R_u), the capacitance of the electric double layer at the electrolyte/electrolyte interface (C_{dl}), and the kinetics of an electrode via the polarization resistance (R_p) at different applied voltages. This also illustrates the ability of EIS to separate the system response into individual physico-chemical processes by their characteristic timescales. As the electrode kinetic process is slower than the liquid electrolyte electronic/ionic conduction, its contribution starts to appear at lower frequencies. Likewise, in other systems, EIS enabled researchers to identify and investigate separate contributions of materials electronic and/or ionic conductivity,[5,6] kinetic activity,[7,8] and mass transport limitation.[9–11] EIS non-invasive and non-destructive nature due to the minuteness of excitation signal also makes it particularly suitable for in-operando studies.[12–20]

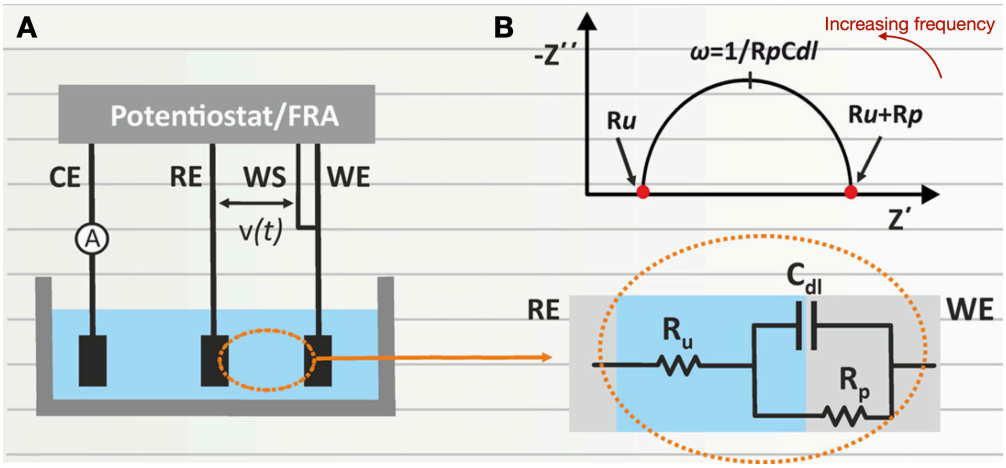

Fig. 1.2 (A) Simple setup to measure EIS response measured from a working electrode (WE) to a reference electrode (RE) in liquid electrolyte. (B) Nyquist plot of EIS and the equivalent circuit representing the system. Adapted from Lazanas & Prodromidis under the Creative Commons License CC-BY-NC-ND 4.0.[4]

1.2 Physics based model of EIS

The assessment of EIS often involves parameter estimation obtained through fitting the impedance spectra into model. The widely used equivalent circuit model (ECM) simplifies the electrochemical system by representing it as a collection of circuit elements. Constant phase elements and modified inductance elements are employed to account for non-idealities such as surface roughness or heterogeneous adsorption.[21–23] More physics-specific elements such as Gerischer,[24,25] de Levie,[26,27] and various Warburg elements, are derived analytical solutions from governing equations and boundary conditions related to transport and kinetic phenomena. Due to its simplicity, ECM is a popular method to transform the spectral data structure of EIS to parameterized values that can be used to quantitatively assess corresponding physico-chemical processes.[5,27,28] Despite its popularity, ECM has drawbacks, including the need for expertise knowledge to select appropriate collection of elements and its non-uniqueness, where different circuits, with or without physical meaning, can provide a good fit for an impedance spectra.[29–31]

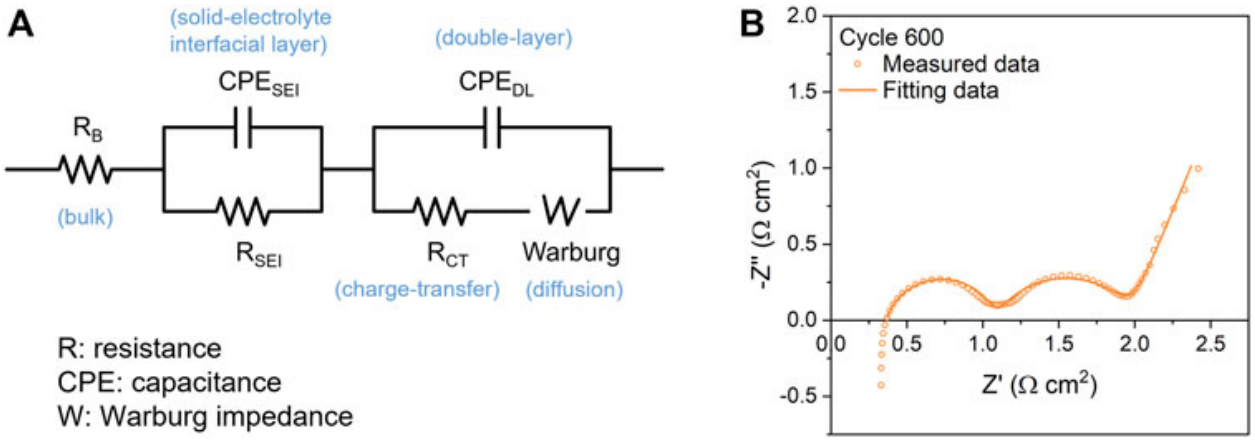

Fig. 1.3 EIS and ECM fit of a Lithium-ion battery. Reproduced from Chen *et al.* under the Creative Commons License CC-BY 4.0.[28]

In contrast, physics-based models establish a direct connection between the physicochemistry of a system and its EIS representation. These models determine the frequency domain responses by solving coupled differential equations, algebraic equations of transport, kinetics, and thermodynamics. Physics-based models excel in simulating complex, interdependent processes and geometric complexities not adequately represented by the generalized ECM elements, as well as connecting trends to internal and external conditions. Many electrochemical systems have been extensively modeled in this manner where the mechanistic understanding proved essential in explaining and predicting trends and behaviors of EIS.[26,32–37]

Fitting a physics-based model to experimental EIS data is often challenging due to the high number of unknowns parameters. For instance, the pseudo-2D model (P2D) used in modeling lithium-ion battery systems impedance responses requires well over 20 parameters to describe the physical, chemical, and electrochemical properties of the cell.[33,37,38] Consequently, effective quantification of P2D model parameters becomes a significant challenge. Researchers often resort to additional characterization and analytical methods, information from ex-situ measurements, or rely on values reported in the literature to estimate these parameters.[37,38] The pseudo-2D model highlights the difficulty in designing experiments to collect sufficient data for determining all physical parameters, as the more complex the

model, the higher the validation requirement for deterministic fitting. Even when sufficient information is available, the convergence of the model can be dependent on a good initial guess and the optimization algorithm, with no guarantee of attaining a unique solution or converging to the global best fit.

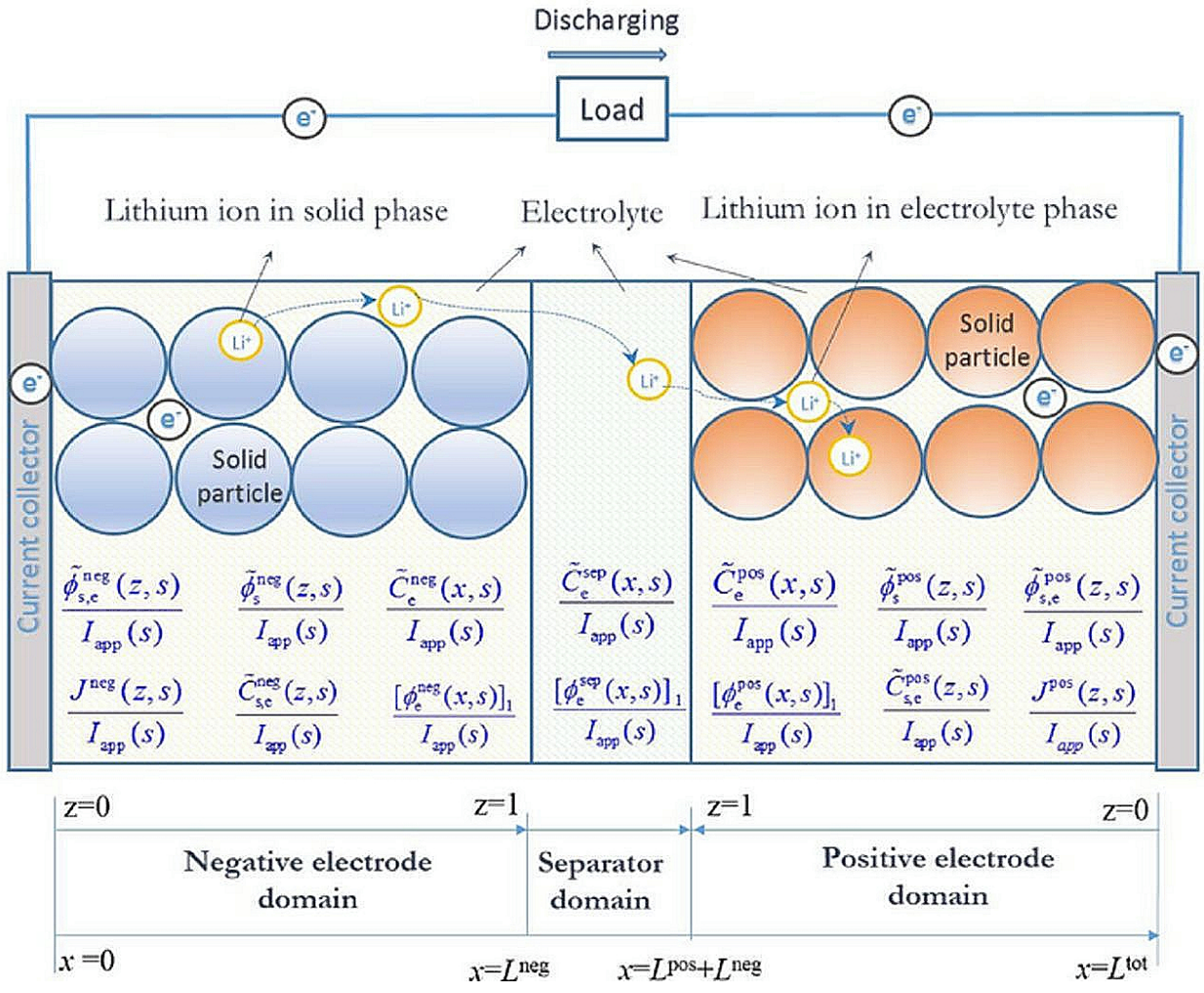

Fig. 1.4 P2D model of Lithium-ion battery. Reproduced from Tran *et al.* under the Creative Commons License CC-BY 4.0.[39]

1.3 Machine learning application in electrochemistry

In recent years, the integration of machine learning within the field of electrochemistry has seen a surge in publications, particularly in diagnostic applications. Mechanistic prediction in this context becomes challenging due to the interplay of various degradation modes and the diverse external and internal conditions that impact the overall state-of-health. In some cases, data-driven machine learning, leveraging electrochemical measurements or operational data, proves adept at predicting state-of-health or remaining useful life without requiring knowledge of the underlying physical mechanisms.[14,20,40,41] Electrochemical impedance spectroscopy (EIS), sometimes included as single-frequency measurement, as frequency sweeps or parameters derived from ECM, have proven effective in data-driven diagnostics for lithium-ion batteries and fuel cell systems.[12,14,20,42–44] To exemplify the potential in incorporating machine learning framework to electrochemical measurements, we will discuss recent advances focus on EIS.

The interpretation of EIS faces inherent challenges due to the complex nature of the electrochemical systems under study. Physico-chemical processes sometimes leave fingerprints on EIS that are visually imperceptible or indistinguishable from one another. From a data structure perspective, the multitude of frequency points in EIS introduces significant dimensionality to training data, as well as escalating the computational cost in mechanistic simulation. Machine and statistical learning approaches have emerged as effective tools to navigate these challenges. Notably, machine algorithms have excelled in EIS pattern recognition, streamlining ECM classification and fitting processes. These advancements not only simplify and expedite ECM implementation but also alleviate subjectivity and the need for expertise in the human selection of appropriate circuits.[45–48]

The utilization of the distribution of relaxation times (DRT) for EIS analysis has gained increased attention and adoption in recent years.[49–52] Incorporation of deep neural networks, Gaussian processes, and Bayesian frameworks has significantly improved the accuracy and reliability of solutions to the inherently ill-posed problem of DRT conversion transforming EIS

into a collection of resistor-capacitor time constants. Additionally, these approaches introduce novel techniques for noise filtering, outlier detection, and finding optimized frequency placement.[29,53–57] Machine learning methodologies further contribute to the field through feature importance analysis, sensitivity analysis, various statistical approaches, offering enhanced insights into the interpretation of complex impedance systems. These approaches provide effective strategies for managing the complexity and high dimensionality inherent in EIS datasets.[12,58–61]

1.4 Combining mechanistic modeling and machine learning

Mechanistic modelling and machine learning are two paradigms that have independently propelled advancements in electrochemistry. Yet there can be even greater potentials in their union. In materials discovery, the integration of machine learning with computational physics and chemistry models creates high fidelity prediction of materials properties, and screening of candidate materials.[62–71] In more recent years, researchers have delved into the use of synthetic data from physics-based simulation to train Lithium-ion battery diagnosis and prognosis models.[72–75] Data-driven surrogate models from these studies and others, although time and resource demanding to gather training data, can be used on demand after.[72,75–77] These works exemplify the opportunities in leveraging the predictive power of physics-based modeling to substitute extensive experimentation and use the pattern recognition power of machine learning to comprehend the complex response of electrochemical systems.

Chapter 2

SIMULATION INFORMED MACHINE LEARNING DIAGNOSTICS OF SOLID OXIDE FUEL CELL SYSTEM

Published with permission from Journal of Electrochemical Society under DOI: 10.1149/1945-7111/ac59f4

Giang Le[1,*]

Luca Mastropasqua [2]

Jack Brouwer [2]

Stuart Alder [1]

[1] Department of Chemical Engineering, University of Washington, Seattle, Washington

[2] National Fuel Cell Research Center, University of California, Irvine, California

[*] Corresponding Author. giangtle@uw.edu

2.1 Introduction

Long-term reliability has been a major factor limiting commercial deployment of solid oxide fuel cell (SOFC) technology.[78,79] Most studies have focused on SOFC degradation mechanisms, in particular the causes (and signs) of long-term degradation in SOFC performance, which tends to be uniform among cell modules in a system.[80–83] Others have involved accelerated testing such as redox cycling, thermal cycling or air-borne contaminant poisoning.[44,84–86] In both settings, post-mortem analysis reveals various failures such as delamination, electrolyte cracking, and fuel depletion.[84–89] These failures are reported to cause fast degradation and catastrophic failure.[81,84,90] A critical step in commercializing SOFC systems is developing

robust diagnostic tools that can detect the onset of these types of critical failures, allowing corrective action before irreversible failure of the entire stack or system.

Electrochemical impedance spectroscopy (EIS) technique is often employed in SOFC degradation studies.[15,17,44,81,91,92] EIS can separate physical processes of different timescales, allowing researchers to deconvolute factors that contribute to SOFC performance.[15,17,44,81,91,92] EIS experiment can be conducted in Galvanodynamic mode by applying an AC current on top of a SOFC load, allowing operando measurement without interrupting power generation.[15,17,44,81,91] Futhermore, experimental and simulation studies have also shown different modes of SOFC failure can have different effects on EIS. Gallo *et al.* reported a large increase in the low frequency gas concentration impedance under high fuel utilization or fuel starvation conditions.[15] Gazzarri & Kesler explored EIS of SOFCs under several different degradation modes including delamination, uniformly distributed surface area loss, and contact degradation. They highlighted distinct EIS changes from each degradation mode on both simulation and experimental results.[93–95]

However, one challenge to using EIS as a diagnostic is the very complex structure of EIS data, which can be difficult to interpret, especially for automated algorithms. Even very detailed equivalent circuit or physics-based models often fail to fully capture all features and frequency dispersion in real EIS data over time,[15,94] and is often simplified to reduce computation time for real-time control.[15,94,96] For this reason, workers have begun to examine data driven approaches where a machine learning model (trained using measured or simulated data) is used to interpret EIS response, rather than using regression to fit the EIS response to a model directly.[14,42,97]

Simulation modeling and machine learning have been increasingly applied in SOFC monitoring and diagnosis literature. Gallo *et al.* used equivalent circuit models to fit EIS data, extracting parameters that were used in a fast dynamic model to predict remaining useful life (RUL) from 5000h of experimental data.[15] Zhang *et al.* and Li *et al.* used a SOFC system model to simulate air and/or fuel leakage in balance of plant (BOP) components. Their deep learning models were effective at recognizing different fault classes from simulated system

variables such as BOP temperature, pressure, voltage and power.[98,99] Polverino *et al.* used a system dynamic model to simulate increased polarization loss and BOP faults to develop signature matrix for on-site system diagnosis.[100] Using voltage history from public experimental anode chlorine and sulfur poisoning studies, Wu & Ye built support vector machine classifier to identify different faults with 97% accuracy rate and built hidden semi-Mark models to predict RUL within ± 20% error.[101]

A significant challenge to using machine learning for SOFC stack failure analysis is the time and expense of gathering training data on real systems undergoing controlled failure over a wide enough range of conditions. For this reason, we take the approach of simulation-informed machine learning as some of the mentioned studies did.[98–101] Simulation-informed machine learning uses machine learning models that learn partly or fully on databases generated from simulation. The use of modeling helps reduce the experimental burden of long-term and accelerated testing and can fill in the under-explored domain of simultaneous occurrence of multiple degradation mechanisms. Machine learning shows great potential in identification of fault patterns without requiring a precise point-by-point fit of the data to a model.[98–101] If successful, simulation-informed machine learning can offer a resource efficient and flexible pathway to SOFC diagnosis.

The success of simulation-informed machine learning depends on various factors including model fidelity, system variability, and measurement uncertainty.[102,103] To overcome these challenges, others have employed various noise filtering, feature selection, and used different machine learning algorithms.[103–106] In this work, we only use simulated data to inform and evaluate a SOFC failure detection tool. We intend to evaluate, adjust and improve the methodology, and apply to experimental data in a future study.

2.2 Methodology

2.2.1 Modeling approach

Solid oxide fuel cell physics model

The SOFC system we model is a 6-cell stack manufactured by SolidPower S.p.a., the description of which is provided elsewhere.[107] The physics we include are based on the prominent processes as interpreted from reported experimental EISs of the same system.[15,108] These physics apply to both regular and defective SOFCs operating on humidified hydrogen fuel gas and air as oxidant gas. As shown in Fig. 2.1, the fuel cell geometry is represented by four parameters: anode channel height h_A, cathode channel height h_C, fuel cell length (along the flow direction, i.e. the x-direction) l, and width w. The geometric values used in the simulation are provided in Appendix Table 2.5. Since the thickness of a SOFC is small compared to its width and length, the 3D problem is approximated in a 2D geometry by pooling variables in the thickness dimension. Many co-flow and counter-flow planar SOFC 2D and 1D models remove the width dimension because there is little variation across the cell when heat loss from SOFC side walls is negligible.[109–111] However, the width dimension is necessary when simulating failures as they can create gradients in the width direction that impact performance and impedance characteristics

A linear relationship between the gas pressure gradient and the volume velocity, $\dot{Q}$, is assumed under laminar flow condition and small pressure drop. Under small temperature and pressure changes, we make the approximation that the volume velocity is proportional to the molar flux, $\dot{N}$, thereby, giving a proportional relationship between the pressure gradient and the molar flux:

$$\dot{N} = \gamma \nabla P = \nabla \widetilde{P} \tag{2.1}$$

where γ is the proportionality constant, P is the pressure, and $\widetilde{P}$ is a reduced pressure term.

Under the assumption of an ideal gas, we apply the following molar continuity equation:[111]

$$0 = -\nabla \cdot \dot{N} + \sum_i \dot{R}_i = -\nabla^2 \widetilde{P} + \sum_i \dot{R}_i \tag{2.2}$$

where $\dot{R}_i$ is the gas consumption or production rate for each gas species i.

The above equation and its boundary conditions determine the molar gas flux as a function of position. One boundary condition is the gas molar flux entering the fuel cell, while the other is the pressure in the downstream anode and cathode gas manifolds.

The reaction rate for each gaseous species is tied to the global hydrogen oxidation electrochemical reaction ($H_2 + 1/2\,O_2 \rightarrow H_2O$):

$$\dot{R}_{H_2} = -\frac{j_F}{2F} \tag{2.3}$$

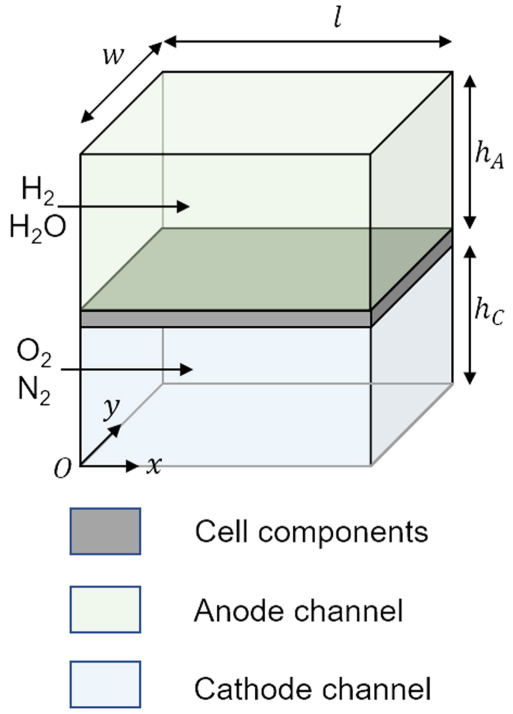

Fig. 2.1 Schematic of SOFC geometry.

$$\dot{R}_{O_2} = -\frac{j_F}{4F} \tag{2.4}$$

$$\dot{R}_{H_2O} = \frac{j_F}{2F} \tag{2.5}$$

where j_F is local Faradaic current density and F is the Faraday constant.

The species mole fractions are governed by species conservation:

$$\frac{Ph}{R_g T_g}\frac{dy_i}{dt} = -\nabla \cdot J_i - \nabla \cdot \left(y_i \dot{N}\right) + \dot{R}_i \tag{2.6}$$

where P is the gas pressure, h is either the anode or cathode channel height, R_g is the universal gas constant, T_g is the lumped gas temperature, y_i is species i mole fraction and J_i is the molar diffusive flux for species i. The diffusive fluxes are evaluated using Fick's law and the binary diffusion coefficient for a two-species system.[112] For a three-species system, diffusive fluxes are evaluated using the Stefan-Maxwell multi-component diffusion model.[113] To account for back diffusion of the anode channel species, we extend the solution in the x-direction in front of the fuel cell gas entrance.[32] Back diffusion of O_2 is deemed negligible due to the smaller concentration gradient and slower diffusion of the cathode gas.

Although the temperature of the gas (T_g) and solid materials (T_s) are treated independently, we use a lumped temperature for all solid components (electrolyte, electrodes, and interconnect). The lumping of the interconnect and cell temperature is justified based on the thermal profiles observed when simulating these temperatures separately. Radiative heat transfer keeps the cell and interconnect temperature within 15 K under simulated operating conditions. Hence, lumping the solid temperatures has minimal effect on the simulated EIS response. The lumped solid temperature T_s is determined through conservation of energy in the solid material:

$$0 = kt_s \nabla^2 T_s + h_{conv}\left(T_g - T_s\right) + j_F\left(-V + \frac{1}{2F}\Delta\overline{H}_{rxn}\right) \tag{2.7}$$

where k is the lumped solid conductivity, t_s is the solid thickness, h_{conv} is the convective

heat transfer coefficient, V is the cell voltage, and $\Delta\bar{H}_{rxn}$ is the molar heat generation from the electrochemical reaction. In lieu of information on the interconnect materials, we use the thermal conductivity of steel and an assumed solid thickness of 2 mm.[114] The resulting thermal profile is deemed reasonable and consistent with the gas inlet and outlet temperatures reported on the same system.[107]

The convective heat transfer coefficient between the gas and solid, h_{conv}, is approximated using the following equation:[111,115]

$$h_{conv} = \frac{Nu \sum_i y_i k_i}{D_H} \tag{2.8}$$

where Nu is the system Nusselt number, k_i is the thermal conductivity of the gas at the gas temperature, and D_H is the hydraulic diameter of the gas channel. We neglect the gas composition dependence for the following reasons: convective heat transfer mainly happens between the cathode gas and the solid due to the cathode much higher flow rate, thermal conductivity of O_2 and N_2 are approximately the same, cathode molar composition doesn't change significantly due to the low air utilization conditions. We use a Nusselt number of 6, a mole fraction of O_2 of 21%, gas thermal conductivity at the inlet temperature, and a hydraulic diameter equals to twice the gas channel height given the flow geometry, to get a convective heat transfer value of 150 W/(m.K).[111,112,115,116]

$\Delta\bar{H}_{rxn}$, the molar heat generation from the electrochemical reaction, is calculated as:

$$\Delta\overline{H}_{rxn}\left(T_g\right) = \overline{H}_{H_2,\ f}\left(T_g\right) + \frac{1}{2}\overline{H}_{O_2,\ f}\left(T_g\right) - \overline{H}_{H_2O,\ f}\left(T_g\right) \tag{2.9}$$

where $\bar{H}_{i,f}$ is the molar enthalpy heat of formation of species i at the gas temperature T_g.

The lumped gas temperature T_g is determined through another energy balance which includes both gas channels:

$$0 = h_{conv}\left(T_s - T_g\right) - \nabla \cdot H - \frac{j_F}{2F}\Delta\overline{H}_{rxn} \tag{2.10}$$

where H is the function of the gas enthalpy flow:

$$H = \sum_i \dot{N} y_i \overline{H}_{i,\ f}\left(T_g\right) \tag{2.11}$$

The transient term in the equations governing temperature are neglected because the temperature dynamics are expected to be much slower than the frequency range investigated with EIS (10 mHz to 100 kHz).[117–119]

The electrochemistry model includes an Ohmic resistance, an activation resistance and capacitance , and the Nernst equation:

$$V = V_0\left(T_s, P\right) + \frac{R_g T_s}{n_e F} \log \frac{P_{H_2} P_{O_2}^{\frac{1}{2}}}{P_{H_2O}} - \eta_{Ohmic} - \eta_{activation} \tag{2.12}$$

where V is the cell voltage, V_0 is the standard cell voltage at the cell operating pressure P and the solid temperature T_s. The second term comes from the Nernstian relationship between the theoretical equilibrium potential and the partial pressures of reactants and products.

The Ohmic overpotential η_{Ohmic} is:

$$\eta_{Ohmic} = j R_{Ohmic} \tag{2.13}$$

where R_{Ohmic} is the lumped Ohmic resistance from fuel cell components and j is the total current density. The local total current density is a sum of Faradaic current density and capacitive current density j_C :

$$j = j_F + j_C \tag{2.14}$$

The electrode activation overpotential $\eta_{activation}$ is expressed empirically using a Butler-Volmer equation for a two-electrons symmetrical reaction:

$$\eta_{activation} = \frac{R_g T_s}{F} asinh\left(\frac{j_F}{2 j_0}\right) \tag{2.15}$$

where j_F is the Faradaic current and j_0 is the exchange current density.

The capacitive current density from the electrode activation overpotential double layer capacitance C_{dl} is given by:

$$j_C = C_{dl}\frac{d\eta_{activation}}{dt} \tag{2.16}$$

The last equation to close out the system of equations is that the applied current, i, equals the area integral of current density over the cell active area A :

$$i = \iint_A j dA \; = \iint_A \left(j_F + j_C\right) dA \tag{2.17}$$

The governing equations and boundary conditions used to solve for each state variable are provided in detail in Appendix Table 2.2

Frequency domain formulation

This section discusses the frequency domain derivation of the system harmonic response to a sinusoidal current perturbation during an EIS experiment. The applied current can be written as:

$$i = i_0 + \frac{\alpha}{2}\left(e^{j\omega t} + e^{-j\omega t}\right) \tag{2.18}$$

where j is the imaginary unity, i_0 is the steady state current or the DC current, α is the dimensionless perturbation amplitude, i^* is a characteristic amplitude defining the scale for α, and ω is the fundamental perturbation frequency.

The steady periodic behavior of any system variable can be treated as a complex Fourier series:[120]

$$X(t,x,y;\alpha,\omega) = X_0 + \sum_{m=1}^{+\infty}\frac{1}{2}\left(X_m(x,y;\alpha)e^{jm\omega t} + \overline{X}_m(x,y;\alpha)e^{-jm\omega t}\right) \tag{2.19}$$

where X_0, X_m and $\bar{X}_m$ are the Fourier coefficients. $\bar{X}_m$ is the complex conjugate of X_m. The amplitude dependence can be removed from the Fourier coefficients by expanding each

coefficient as regular perturbation series in alternating powers of α.[120]

$$X_m(x, y; \alpha) = \sum_{r=0}^{\infty} \alpha^{m+2r} X_{m,m+2r}(x, y) \tag{2.20}$$

The above expansion is substituted into all governing equations to determine the harmonic responses of the system. We also use the Taylor series expansion at the constant term (X_0) of the Fourier series for the voltage and activation overpotential functions in Eqs. 2.12 and 2.15. Terms with $m = 1$ and $r = 0$ represent the linear response of the system to current modulation. The impedance response is:

$$Z(\omega) = \frac{\Delta V}{\Delta I} = V_{1,1} \tag{2.21}$$

The derived harmonic formulation of the governing equations and boundary conditions is provided in Appendix Table 2.3.

Figure 2.2 shows simulated EIS along with a few experimental EIS from our collaborators at the National Fuel Cell Research Center, University of CaliforniaIrvine. These limited experimental data do not fully validate of our model, but demonstrate how the data is representative of real SOFC stack impedance behavior.

Aging degradation simulation

To simulate the uniform degradation phenomenon that occurs over SOFC lifetime, we spanned the electrochemistry parameter space over relevant ranges. These include the exchange current density j_0, the area specific Ohmic resistance R_{Ohmic} and activation double layer capacitance C_{dl}. The electrochemistry parameters and the ranges used in simulating aging are in Appendix Table 2.9. To account for small variations in performance between cells that can come from initial difference in micro-structures or difference in aging rates, we added a 5% standard deviation to these aging-related performance parameters in simulating each cell EIS.

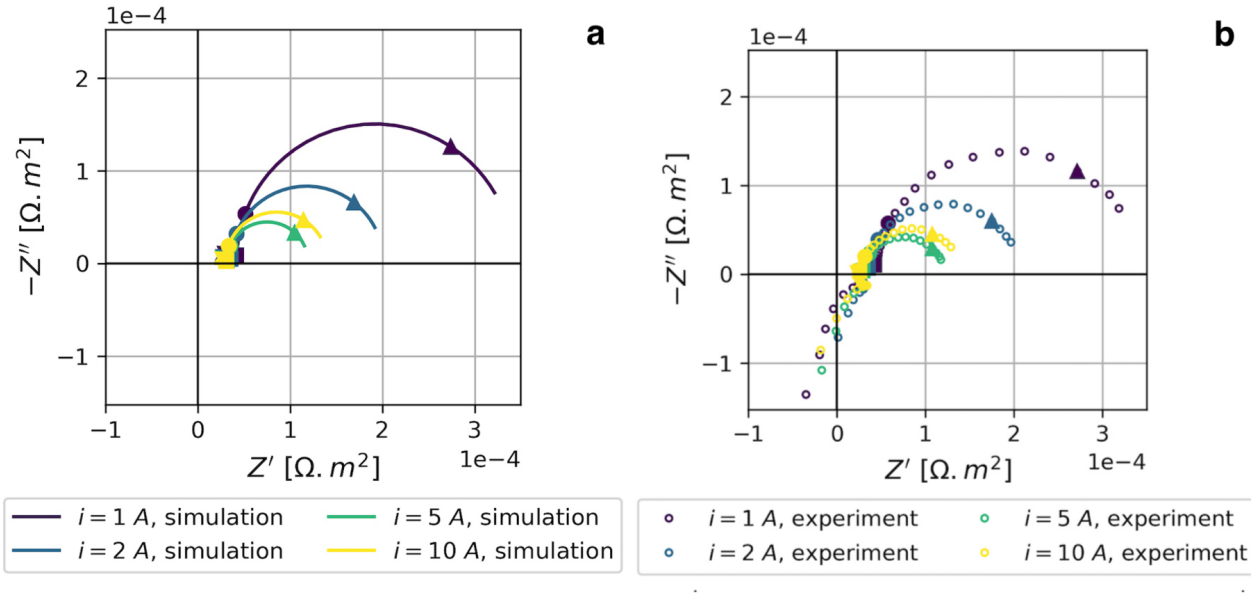

Fig. 2.2 Nyquist plot of healthy cell EIS from simulation (a) and experiment (b). The stack operates with 1.2 Nl min^{-1} 50:50 mole fraction mixture of H_2 and N_2, 18.9 Nl min-1 air, and different current. The ▾, ■, • and ▲ symbols indicate 0.1 Hz, 1 Hz, 10 Hz, and 100 Hz, respectively.

Failure physics models

We examined three different failure models: fuel maldistribution, delamination and oxidant crossover. We simulated EIS for a 6-cell stack that has one of these failures on one of the cells. The choice of number of cells and geometry parameters is intentional to simulate a short stack system manufactured by SolidPower S.p.a (Italy) that we plan to conduct future EIS experiment on.[107] The following three subsections describe the three failure models included in this study. Just as in simulation of aging , these failure simulations also have a 5% standard deviation in the aging-related parameters to account for possible deviation between cells' microstructure or aging rate.

Fuel maldistribution failure model

In the case of fuel maldistribution, one cell receives less fuel than the rest of the stack. Fuel maldistribution is quantified by the parameter r_1 :

$$r_1 = \frac{U_{f,d}}{U_{f,\ stack}} - 1 \tag{2.22}$$

where $U_{f,d}$ is the fuel utilization at the failed cell, and $U_{f,stack}$ is the stack average fuel utilization factor. An intact stack would have an r_1 value of 0.

From conservation of molar flow rate through the stack, the fuel utilization on the rest of the cells $U_{f,o}$ is:

$$U_{f,\ o} = (r_1 + 1)\, U_{f,\ stack} \frac{n_{cell} - 1}{n_{cell}\,(r_1 + 1) - 1} \tag{2.23}$$

where the number of cells in the stack n_{cell} is 6.

Delamination failure model

Figure 2.3 shows a schematic of the modeled delamination in the center of the cell active area.

Delamination is quantified by the parameter r_2 :

$$r_2 = \frac{A_d}{A} \tag{2.24}$$

where A_d is the area of the delaminated region, and A is the cell area. An intact cell would have an r_2 value of 0.

In the delaminated area, both Faradaic and capacitive current density are assumed to be effectively zero.[93,94] Hence, the first harmonic responses for both Faradaic and capacitive current density in this region are also zero.

Oxidant crossover failure model

We simulate a gas leak from the cathode channel to anode channel due to a crack formed in the middle of the cell. The crossover oxygen reacts directly with hydrogen in a parasitic reaction that is the same as the electrochemical reaction ($H_2 + 1/2\,O_2 \rightarrow H_2O$). Oxidant crossover is quantified by the parameter r_3 :

$$r_3 = \frac{\iint_A \dot{R}_{O_2,par} dA}{\iint_A \dot{R}_{O_2,ele} dA} = \frac{L_{O_2}}{\left(\frac{i}{4F}\right)} \tag{2.25}$$

where $\dot{R}_{O_2,par}$ is the local consumption rate of oxygen from the parasitic reaction, $\dot{R}_{O_2,ele}$ is the consumption rate of oxygen from the electrochemical reaction, and L_{O_2} is the total amount of oxygen leaked from the cathode channel. An intact cell would have an r_3 value of 0.

Assuming that crossover oxygen reacts instantaneously, the distribution of the oxygen

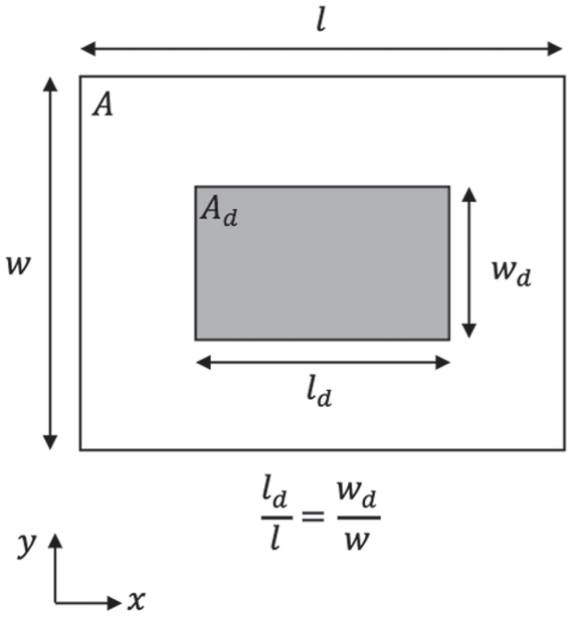

Fig. 2.3 Schematic of delaminated cell. l_d is the length of the delaminated region, w_d is the width of the delaminated region, A_d is the delaminated area, and A is the cell area.

crossover from gas leak is the same as the distribution of parasitic reaction consumption rate. We use a standard bivariate normal distribution function to evaluate the spatial distribution of leaked oxygen:

$$\dot{R}_{O_2,par}(x,y) = L_{O_2}\mathcal{N}\left((x_d,y_d),\sigma^2\right) = L_{O_2}\frac{1}{\pi\sigma^2}\exp\left(-\frac{(x-x_d)^2+(y-y_d)^2}{\sigma^2}\right) \tag{2.26}$$

where $\mathcal{N}\left((x_d,y_d),\sigma^2\right)$ is the distribution function of a standard bivariate normal distribution around the defect coordinate (x_d,y_d) where the crack locates, with equal variance in both direction σ^2. The Gaussian normal distribution has been used to simplify the leakage flow from a crack.[121] The crack is at the center of the cell, i.e. the defect coordinate (x_d,y_d) is $(l/2,w/2)$.

The modified governing equations for a cell with oxidant crossover failure are provided in Appendix Table 2.4.

Simulation methodology

We used COMSOL Multiphysics to simulate the steady state operation and impedance response of SOFC, using the Coefficient Form PDE module and the Domain ODEs and DAEs module. We compared EIS results using different element sizes with COMSOL auto physics-controlled meshing sequence, to choose the appropriate number of finite elements for accurate and efficient simulation. The preset fine element size was selected for all simulations. All EIS were simulated for a frequency range from 10 mHz to 100 kHz at 10 points per decade (ppd). The COMSOL models of nominal planar SOFC and the studied failures have been shared openly to facilitate future use and feedback under the MIT license.[122]

2.2.2 Machine Learning Method

Fixed operating condition diagnostics with stack EIS

We applied machine learning methods to detect single cell failure at the operating condition provided in Appendix Table 2.6. To build the machine learning database, we used our physics model to simulate EIS of a stack that only experienced uniform aging degradation. We also simulated stack EIS with one cell having one of the three failures mentioned previously on top of aging varying the failure level while also varying electrochemistry parameters to simulate aging. To efficiently explore the parameter space, we used the quasi-random Sobol's sampling method and generate a database of 6,000 EIS simulations for this objective.[123] The Sobol's sampling algorithm was taken from SALib open-source python package.[124] The electrochemistry parameter ranges and failure levels examined are in Appendix Tables 2.9 and 2.1.

To label these simulations, we had to establish a detection threshold for each of the failures. A simulation with failure level higher than the chosen threshold is labelled as defective or labelled as normal otherwise. Threshold selection should depend on practical considerations such as the cost of replacing a stack prematurely or the cost of power interruption from catastrophic failure. Due to our lack of knowledge regarding these considerations, we picked these thresholds arbitrarily, with the understanding that these can be modified in the future as dictated by experiental observations on real SOFC stacks. The decision thresholds chosen are provided in Table 2.1.

Table 2.1 Decision (detection) threshold for each failure.

Failure type	Failure parameter	Value range	Decision threshold
Fuel maldistribution	r_1	$0.0 - 0.23$	0.1
Delamination	r_2	$0.0 - 0.75$	0.375
Oxidant crossover	r_3	$0.0 - 0.1$	0.05

From the simulation database, we trained a support vector machine (SVM) classifier to

label impedance as either normal, type 1 (fuel maldistribution), type 2 (delamination) or type 3 failure (oxidant crossover). The classifier takes EIS as real and imaginary parts of the impedance at each frequency. Hence, the machine learning input has 142 features (from 71 frequencies between 10 mHz to 100 kHz at 10 points per decade). In addition to the SVM classifier, we also created neural network (NN) regression models to predict failure level from EIS. These NNs have up to 3 hidden layers, up to 100 neurons per layer, and use the sigmoid activation function.

We used a 60% training 40% testing random split for SVM method. For NN regression, we used a 30% training, 30% validation, and 40% testing split.

Cross-condition diagnostics with pristine and final stack EIS

We explored machine learning failure detection from stack EIS at any operating condition, given that the initial/pristine stack EIS is known. At each operating condition, we simulated stack EIS and EIS of a hypothetical pristine condition point of reference. The electrochemistry parameters assumed for a pristine cell or stack is in Appendix Table 2.10. Just like the last machine learning objective, we simulated EIS of aging stack and stack with one of the failures on top of aging. We used Sobol's sampling to explore the operating condition space (Appendix Table 2.7), the aging electrochemistry parameter space (Appendix Table 2.9) and failure level ranges (Table 2.1).

Different from fixed condition diagnostics, we used two pieces of information to inform the machine learning model. The first is the pristine stack EIS. The second is the difference between the final EIS and the pristine EIS. The total number of features is 284: 142 from the pristine stack EIS, 142 from the frequency by frequency difference between the final EIS and the pristine EIS at the same operating condition. We use the same decision thresholds in Table 2.1 to label the 57,000 EIS database to train SVM diagnostic model. With the same input, we train NNs to predict failure level. These NNs have up to 3 hidden layers, up to 100 neurons per layer, and use the sigmoid activation function.

We used a 60% training 40% testing random split for SVM method. For NN regression,

we used a 30% training, 30% validation, and 40% testing split.

2.3 Results and Discussion

2.3.1 Aging degradation EIS

Figure 2.4 shows the Nyquist representation of some EIS simulations from the fixed operating condition diagnostics' aging database. As seen on Fig. 2.4, by changing electrochemistry parameters, the resulting EIS may have different high-frequency intercepts due to different Ohmic resistances. Aged EIS may have different activation resistances, indicated by the high-frequency activation semi-circle. The low-frequency semi-circle corresponds to gas conversion impedance, also called gas concentration impedance, that arises from the partial gas pressure dependence in Nernst equation.[32]

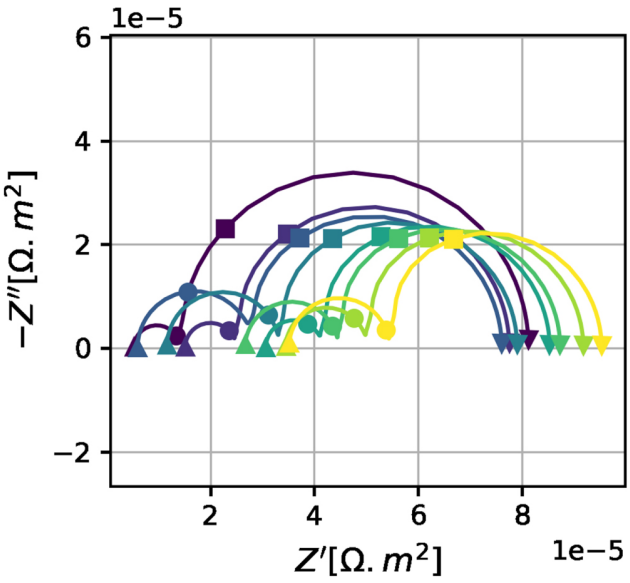

Fig. 2.4 Nyquist plot of cell EIS from the aging degradation simulation database at the same operation. The ▾, ■, • and ▲ symbols indicate 0.1 Hz, 1 Hz, 10 Hz, and 100 Hz, respectively.

2.3.2 Fuel maldistribution failure EIS

To illustrate how fuel maldistribution affect EIS, we created simulations of different failure levels r_1, at the operating condition in Appendix Table 2.6, and with the pristine electrochemistry parameters in Appendix Table 2.10. The simulation results of the defective cell and stack EIS are shown in Fig. 2.5.

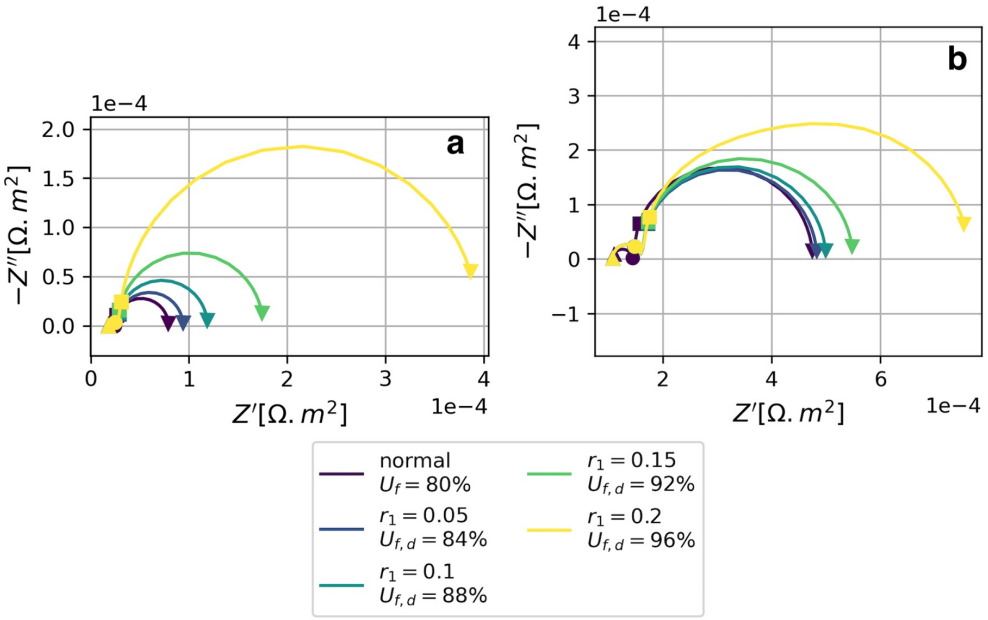

Fig. 2.5 Effect of fuel maldistribution on linear impedance response at the same operation and pristine condition on (a) pristine cell EIS and (b) pristine stack EIS. The ▾, ■, • and ▲ symbols indicate 0.1 Hz, 1 Hz, 10 Hz, and 100 Hz, respectively.

Seen on Fig. 2.5a, the defective cell total impedance increases with increasing failure level. The main contribution to this increase comes from low frequency gas conversion process, due to the decreasing hydrogen and increasing water mole fraction from an increased fuel utilization.[15,32] The stack EIS on Fig. 2.5b not only displays an overall increase of total impedance, but also a shape change in the gas conversion feature. At higher failure levels, the gas conversion feature shifts from a half circle for a normal stack to a more depressed half circle, resembling a constant phase element. This can be explained by the

small difference in gas conversion timescale, or peak frequency, between a normal cell and a defective cell, resulting in a more distributed shape on stack EIS. The gas conversion characteristic timescale is slower with higher the failure level i.e. higher fuel utilization at defect cell. Except for the highest failure level simulation on Fig. 2.5b, the stack EIS exhibits fairly little change.

2.3.3 Delamination failure EIS

To illustrate how delamination affect EIS, we created simulations of different delamination levels r_2, at the operating condition in Appendix Table 2.6, and with the pristine electrochemistry parameters in Appendix Table 2.10. The simulation results of the delaminated cell EIS and the stack EIS are shown in Fig. 2.6.

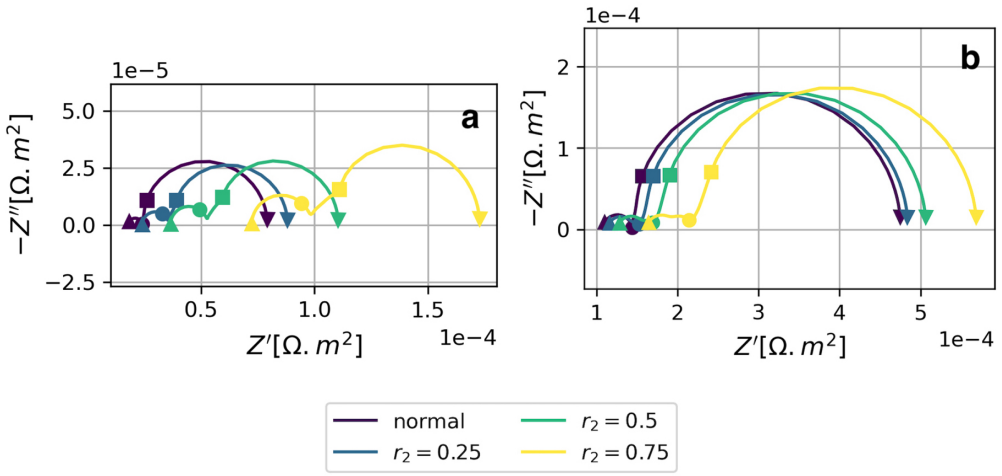

Fig. 2.6 Effect of delamination on linear impedance response at the same operation and pristine condition on (a) pristine cell EIS and (b) pristine stack EIS. The ▾, ■, • and ▲ symbols indicate 0.1 Hz, 1 Hz, 10 Hz, and 100 Hz, respectively.

On Fig. 2.6a, with increasing levels of delamination, we observe an increase in both the Ohmic resistance and the electrode activation resistance. These increased resistances can be explained by the increase in local current density as the same applied current has to pass through a reduced active area. At the lower frequency range, we observe the appearance of

a 45^o slope, typically associated with diffusion process, at timescale faster than gas conversion. The diffusion process relevant to this timescale would be the anode gas diffusion from hydrogen rich, water poor delaminated area in the center toward the outer active area. On Fig. 2.6b, at higher failure levels, there is a frequency dispersion in the activation feature, increase in Ohmic and activation resistances on stack EIS. The 45^o slope diffusion feature from delaminated cell EIS is not visible on stack EIS, but a decrease in the phase angle can be observed for the stack EIS with the most delaminated cell.

2.3.4 Oxidant crossover failure EIS

To illustrate how oxidant crossover affect EIS, we created simulations of different oxidant crossover levels r_3, at the operating condition in Appendix Table 2.6, and with the pristine electrochemistry parameters in Appendix Table 2.10. The simulation results of the delaminated cell EIS and the stack EIS are shown in Fig. 2.7.

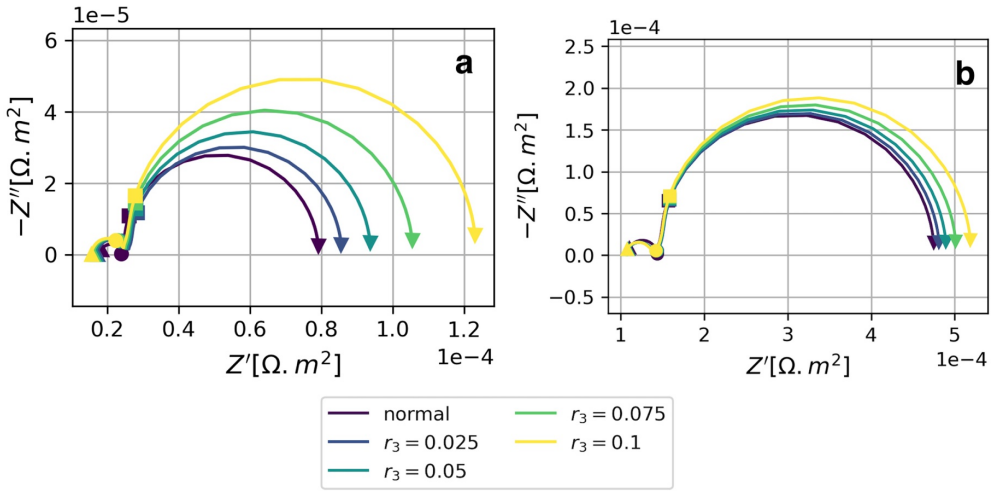

Fig. 2.7 Effect of oxidant crossover on linear impedance response under the same operating condition on (a) pristine cell EIS and (b) pristine stack EIS. The ▾, ■, • and ▲ symbols indicate 0.1 Hz, 1 Hz, 10 Hz, and 100 Hz, respectively.

Seen on Fig. 2.7a, compared to the last two failures, the change in EIS behavior seen in these simulations is less substantial, despite at the max simulated failure level ($r_3 = 0.1$),

hydrogen is near depletion at the crack position ($\min(y_{H_2}) = 0.055$). The main change in cell and stack impedance mainly comes from the gas conversion feature. For these, changes in stack EIS are near imperceptible and appear to be quite similar to behavior of smaller levels of fuel maldistribution (Fig. 2.5b and Fig. 2.7b).

2.3.5 Fixed operating condition diagnostics with stack EIS

The result of the SVM diagnosing the stack EIS is summarized in Fig. 2.8. On the confusion matrix, with corresponding predicted and true labels, is the number of simulations and the accuracy rate normalized by class size in parentheses. The matrix diagonal values are the number of simulations correctly labelled. The model performs well, with diagonal accuracy rate above 90% for both training and testing data, and few mislabeled EIS. When inspecting the false negatives, i.e. mislabeled stack EIS with failure level above detection threshold, we find that they are only mislabeled as normal. The failure levels of these false negatives are also distributed around the detection threshold, suggesting a sensitivity limit.

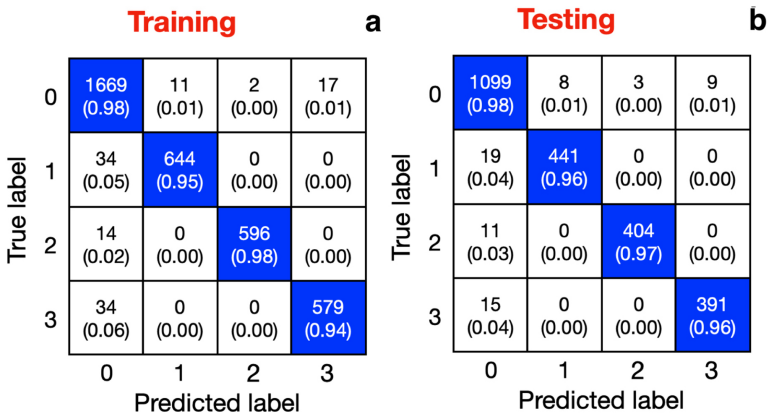

Fig. 2.8 Confusion matrix of SVM classification in fixed operating diagnostics with (a) training dataset and (b) testing dataset. The matrix value is the number of simulations with the corresponding true and predicted label and in parentheses is the accuracy rate normalized by the class size. Labels: 0normal stack, 1stack with fuel maldistribution, 2stack with delaminated cell, and 3stack with oxidant crossover.

Given the continuous nature of failure level, we also attempted to use NN regression

models. Seen on Fig. 2.9, our NNs can predict failure level with high R2-score. Under fixed condition, neural networks are able to deconvolute simulated EIS information to give highly accurate failure level prediction.

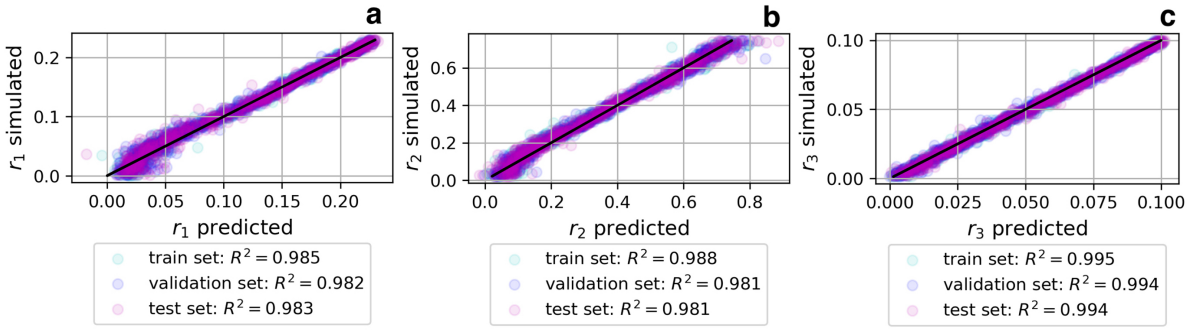

Fig. 2.9 Fixed operating condition NN prediction versus simulated failure level for (a) fuel maldistribution, (b) delamination, and (c) oxidant crossover.

2.3.6 Cross-condition diagnostics with pristine and final stack EIS

We find that using only the final EIS input is not sufficient to make good diagnostics across operating conditions. Therefore, as mentioned in the Machine Learning Method section, we used the difference between final and pristine stack EIS and the pristine stack EIS. These two pieces of information prove to be sufficient for the SVM classifier to diagnose the stack EIS. We suspect that the need for additional input from the pristine stack EIS is because EIS varies significantly with operating condition.

The result of our SVM is shown on Fig. 2.10. Among the three failures, delamination stands out as being labelled correctly at a higher rate (0.98), and no delaminated stack EIS is mistaken for another failure type, only mislabeled as normal. This may be linked to the distinctive decrease in phase angle at the onset of gas conversion impedance arc as mentioned in Delamination failure EIS section. On the other hand, fuel maldistribution and oxidant crossover can be mislabeled as one another. This may be linked to similar EIS trends observed between these two failures as discussed in previous sections.

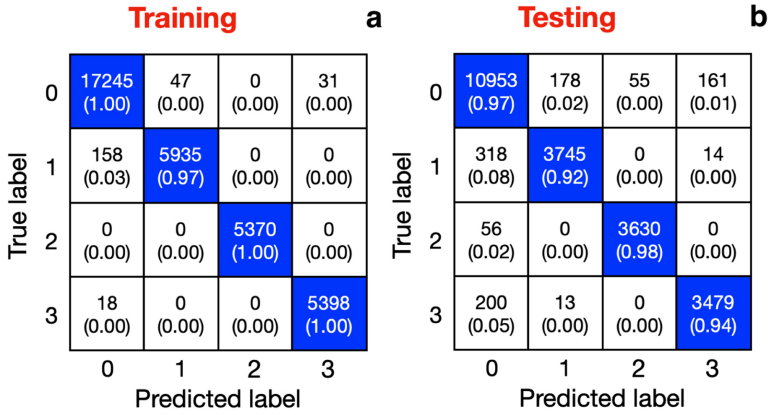

Fig. 2.10 Confusion matrix of SVM classification in cross-condition diagnostics with (a) training dataset and (b) testing dataset. The matrix value is the number of simulations with the corresponding true and predicted label and in parentheses is the accuracy rate normalized by the class size. Labels: 0normal stack, 1stack with fuel maldistribution, 2stack with delaminated cell, and 3stack with oxidant crossover.

Figure 2.11 reports the results of cross-condition failure level NN regression. Generally, these models under-perform compared to fixed condition NN models. Delamination failure NN stands out as being more accurate, with R2-score above 0.99.

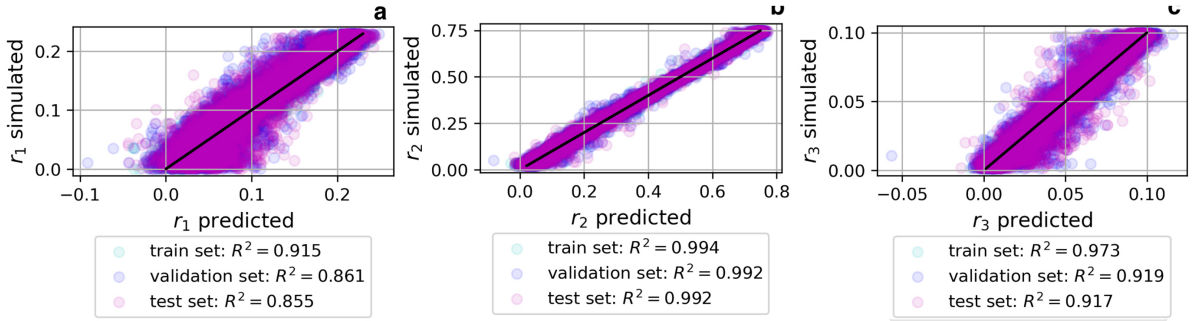

Fig. 2.11 Cross-condition NN prediction versus simulated failure level for (a) fuel maldistribution, (b) delamination, and (c) oxidant crossover.

Both machine learning models, NN and SVM underperform compared to fixed operating condition diagnostics. This suggests that cross-condition diagnostics is more challenging even when additionally informed by a pristine stack EIS.

2.3.7 Noise-injected fixed operating condition SVM model

The simulation-assisted models are intended for diagnosis of experimental EIS that often contains measurement noise. Noise injection in machine learning, particularly neural networks, has shown to regularize and improve the robustness of the model.[125–127] Therefore, we provide here an investigation on how SVM perform when Gaussian noise is added in training data and how models trained with different noise level perform on noisy testing data.

We used the same 6,000 EIS database we introduced in fixed operating condition diagnostics and the same 60% training, 40% testing split. We added Gaussian noise to the training data and train SVM on noisy training data to obtain noise-injected SVM models. With the addition of Gaussian noise, the SVM model input, X, is:

$$X = X_{EIS}\left(1 + \mathcal{N}\left(0, \sigma^2\right)\right) \tag{2.27}$$

Where X_{EIS} is the simulated EIS data as described in the Machine Learning Method section, $\mathcal{N}\left(0, \sigma^2\right)$ is the normal distribution function with a mean of 0 and standard deviation of σ, which we refer to as noise level.

The noise-injected SVM models were tested on the noise-free testing dataset. In Fig. 2.12, we compare the results of the SVM model trained with noise injection with the original SVM model trained on noise-free data. Prediction accuracy for the testing data decreases slightly with increasing level of noise injection. However, even at 5% noise level, the accuracy remains high - 92.5%. The trade-off in decreased accuracy could be balanced if the noise-injected model generalizes better to noisy EIS input. Therefore, we evaluated the performance of the noise-injected SVM models with noisy testing dataset and summarized the results in Fig. 2.13. Unsurprisingly, for all SVM models, accuracy decreases with the increasing noise level in the testing data. The models that are trained with noisy training data have better accuracy when tested with noisy data. The SVM model trained on noise-free data is the least accurate model with noisy testing data, suggesting that noise injection can help SVM to generalize better to noisy data. At test noise levels less than 5%, the SVM model trained with

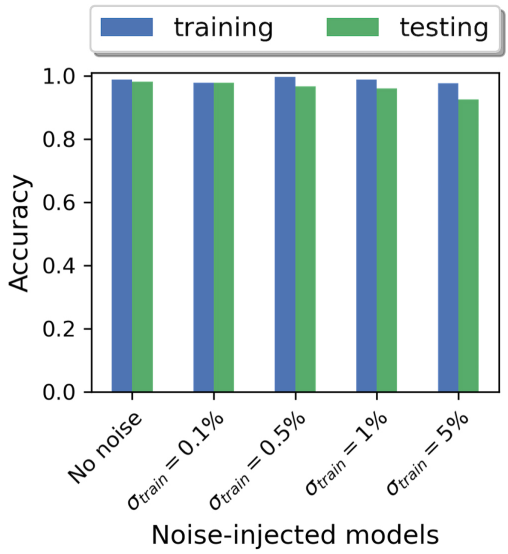

Fig. 2.12 SVM training and testing results of SVM models with various levels of Gaussian noise injection.

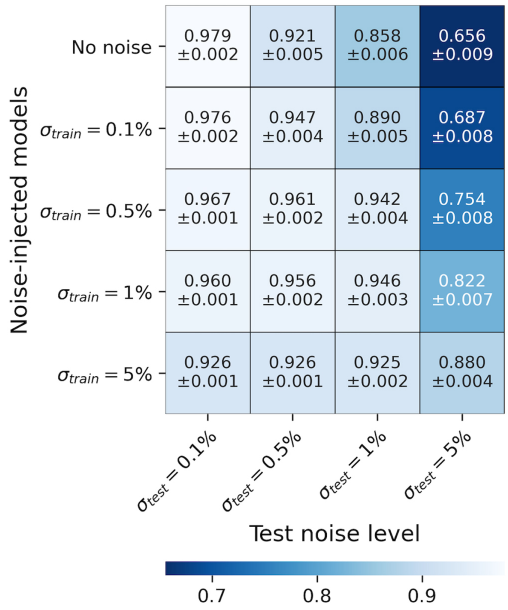

Fig. 2.13 Testing accuracy of noise-injected SVM models. Testing accuracy is averaged between 100 iterations of Gaussian noise addition to the noise-free testing dataset.

5% Gaussian noise is less accurate compared to the other SVM models. This suggests that too much noise injection can also worsen the model performance when the EIS measurement is not as noisy.

2.3.8 Feature importance for fixed operating condition diagnosis

Feature importance analysis can offer some insights to future design of diagnostic protocol. For the fixed-operating condition diagnostic, the SVM model uses the linear kernel. Therefore, the importance of each feature can be ranked by the magnitude of their corresponding coefficients.[128] Figure 2.14 shows the 10 features with the top coefficients, i.e. most important, from the 142 EIS input for fixed operating condition diagnosis.

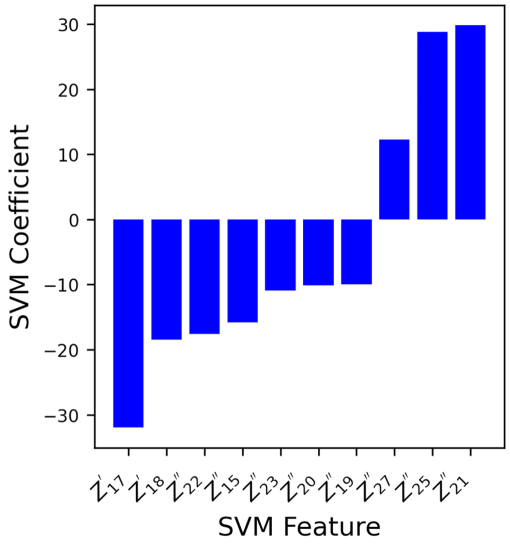

Fig. 2.14 Top features for fixed operating conditions diagnostics according to SVM classifier. The superscript ' refers to the real part of the impedance and superscript '' refers to the imaginary part. The subscript denotes the index of the frequency, starting from 0.01 Hz being 1.

As seen on Fig. 2.14, a combination of imaginary and real parts of the impedance contributes to SVM diagnosis. These frequencies range from 0.50 to 5 Hz and this range is highlighted on the Nyquist plot of a pristine stack in Fig. 2.15. From Fig. 2.5b and

Fig. 2.6b, this frequency range is where we can observe a decrease in the phase angle in the stack EIS with both fuel maldistribution and delamination failures, which could explain its significance to the SVM model. However, not much significance in stack EIS behavior in this frequency range can be observed for oxidant crossover behavior in Fig. 2.7b, underscoring the SVM model pattern recognition ability over visual inspection.

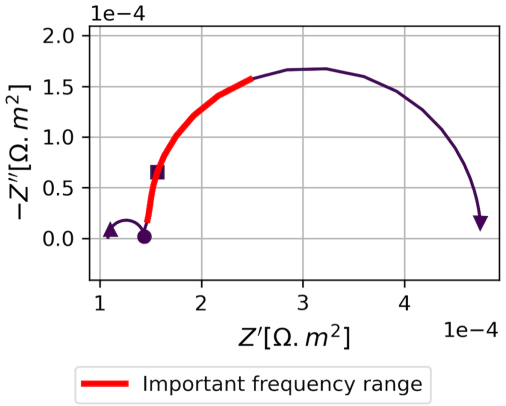

Fig. 2.15 The most important frequency range to fixed operating condition SVM diagnosis, illustrated on a normal stack EIS. The ▾, ■, • and ▲ symbols indicate 0.1 Hz, 1 Hz, 10 Hz, and 100 Hz, respectively.

2.4 Conclusions

In this work, we used physics models to simulate the behavior of SOFC under several failures that could occur during its operation: fuel maldistribution, delamination and oxidant crossover. These simulations show that failures can lead to features in EIS that deviate from standard circuit elements behavior, emphasizing the need for physics-based modeling in SOFC diagnostics. We spotlight the challenge of using system level measurement for diagnostics over single cell measurement as diverging cell behavior can appear less prominent on stack EIS. We demonstrate some initial results of machine learning stack diagnosis on our simulated EIS database. Support vector machine is able to distinguish between different failure types across operating conditions and variations in electrochemistry parameters. In

this study, in addition to the stack EIS, cross-condition diagnostic also needs information from the EIS of a pristine stack point of reference.

The SVM model analysis offers some insights to failure diagnosis using EIS. For fixed operating condition SVM diagnosis, we find that adding Gaussian noise to training data may increase the model robustness against random noise in EIS. SVM also identifies the frequency range that is significant to failure recognition in our fixed operating condition diagnosis. Feature importance study using simulation-informed machine learning as we demonstrate here may inform more efficient data collection in real-time diagnosis.

In future work, we will move toward adapting our simulation-informed machine learning framework on experimental EIS taken from healthy and defective stacks. We will explore using other algorithms and preprocessing techniques to increase resilience against potential deviation from the physics model prediction and measurement noise. We also plan to investigate the effect of detection threshold on the diagnostic tool's effectiveness.

2.5 Acknowledgments

This work was supported in part by a gift from Microsoft Corporation and the Clean Energy Institute Fellowship. We also acknowledge the valuable feedback we received from Prof. David Beck, Department of Chemical Engineering, University of Washington.

2.6 Appendix

2.6.1 Appendix A: Model Equations

Table 2.2 Steady state governing equations and boundary conditions for SOFC with H_2/H_2O fuel and O_2/N_2 oxidant gas.

Reduced anode gas channel pressure - $\widetilde{P}_A$:

$$0 = -\nabla^2 \widetilde{P}_A \qquad \text{A1-1}$$

BC at $x = 0$:

$$-\mathbf{n} \cdot \nabla \widetilde{P}_A = \dot{N}_{Ax,\ in} \qquad \text{A1-2}$$

where $\dot{N}_{Ax,\ in}$ is the anode gas inlet flow rate, calculated from the fuel utilization factor and the inlet hydrogen mole fraction $y_{H_2,in}$:

$$\dot{N}_{Ax,\ in} = \frac{i}{2F} \frac{1}{y_{H_2,in} U_f} \frac{1}{w} \qquad \text{A1-3}$$

BC at $x = l$:

$$\widetilde{P}_A = 0 \qquad \text{A1-4}$$

BC at $y = 0$ and $y = w$:

$$-\mathbf{n} \cdot \nabla \widetilde{P}_A = 0 \qquad \text{A1-5}$$

Reduced cathode gas channel pressure - $\widetilde{P}_C$:

$$0 = -\nabla^2 \widetilde{P}_C - \frac{j}{4F} \qquad \text{A1-6}$$

BC at $x = 0$:

$$-\mathbf{n} \cdot \nabla \widetilde{P}_C = \dot{N}_{Cx,\ in} \qquad \text{A1-7}$$

where $\dot{N}_{Cx,\ in}$ is the cathode gas inlet flow rate, calculated from the air utilization factor and the inlet oxygen mole fraction $y_{O_2,in}$:

$$\dot{N}_{Cx,\ in} = \frac{i}{4F} \frac{1}{y_{O_2,in} U_a} \frac{1}{w} \qquad \text{A1-8}$$

BC at $x = l$:

$$\widetilde{P}_C = 0 \qquad \text{A1-9}$$

BC at $y = 0$ and $y = w$:

$$-\mathbf{n} \cdot \nabla \widetilde{P}_C = 0 \tag{A1-10}$$

Hydrogen mole fraction - y_{H_2}:

$$0 = D_{H_2,H_2O} \frac{Ph_A}{R_g T_g} \nabla^2 y_{H_2} - \nabla \cdot \left(y_{H_2} \nabla \widetilde{P}_A \right) - \frac{j}{2F} \tag{A1-11}$$

BC at $x = 0$:

$$y_{H_2} = y_{H_2,\ back\ diffusion} \tag{A1-12}$$

BC at $x = l$, $y = 0$ and $y = w$:

$$\mathbf{n} \cdot \nabla y_{H_2} = 0 \tag{A1-13}$$

Water mole fraction - y_{H_2O}:

$$0 = D_{H_2,H_2O} \frac{Ph_A}{R_g T_g} \nabla^2 y_{H_2O} - \nabla \cdot \left(y_{H_2O} \nabla \widetilde{P}_A \right) + \frac{j}{2F} \tag{A1-14}$$

BC at $x = 0$:

$$y_{H_2O} = y_{H_2O,\ back\ diffusion} \tag{A1-15}$$

BC at $x = l$, $y = 0$ and $y = w$:

$$\mathbf{n} \cdot \nabla y_{H_2O} = 0 \tag{A1-16}$$

Oxygen mole fraction - y_{O_2}:

$$0 = D_{O_2,N_2} \frac{Ph_C}{R_g T_g} \nabla^2 y_{O_2} - \nabla \cdot \left(y_{O_2} \nabla \widetilde{P}_C \right) - \frac{j}{4F} \tag{A1-17}$$

BC at $x = 0$:

$$y_{O_2} = y_{O_2,\ in} \tag{A1-18}$$

BC at $x = l$, $y = 0$ and $y = w$:

$$\mathbf{n} \cdot \nabla y_{O_2} = 0 \tag{A1-19}$$

Lumped solid temperature - T_s:

$$0 = kt_s \nabla^2 T_s + h_{conv} \left(T_g - T_s \right) + \frac{j}{2F} \left(-V + \Delta \overline{H}_{elec} \right) \tag{A1-20}$$

BC at $x = 0$ and $x = l$:

$$-\mathbf{n} \cdot (-k \nabla T_s) = h_{conv} (T_g - T_s) \tag{A1-21}$$

BC at $y = 0$ and $y = w$:

$$-\mathbf{n} \cdot (-k \nabla T_s) = -\Phi_{wall} \tag{A1-22}$$

where Φ_{wall} is the thermal flux from the fuel cell wall.

Lumped gas temperature - T_g:

$$0 = h_{conv}\left(T_s - T_g\right) - \nabla \cdot H(T_g) - \frac{j}{2F}\Delta\overline{H}_{elec} \quad \text{A1-23}$$

BC at $x = 0$:

$$T_g = T_{g,in} \quad \text{A1-24}$$

Local current density and voltage equations:

$$V = V_0\left(T_s, P\right) + \frac{R_g T_s}{n_e F}\log\frac{P_{H_2}P_{O_2}^{\frac{1}{2}}}{P_{H_2O}} - \eta_{Ohmic} - \eta_{activation} \quad \text{A1-25}$$

$$\eta_{Ohmic} = jR_{Ohmic} \quad \text{A1-26}$$

$$\eta_{activation} = \frac{R_g T_s}{F} asinh(\frac{j}{2j_0}) \quad \text{A1-27}$$

$$j_C = 0,\ j = j_F \quad \text{A1-28}$$

$$i = \iint_A j dA \quad \text{A1-29}$$

The above equations determine local current density j, and cell voltage V.

Table 2.3 Linear impedance response governing equations and boundary conditions (BC) for SOFC with H_2/H_2O fuel and O_2/N_2 oxidant gas.

Reduced anode gas channel pressure:

$$0 = \widetilde{P}_{A,1,1} \tag{A2-1}$$

Reduced cathode gas channel pressure:

$$0 = -\nabla^2 \widetilde{P}_{C,1,1} - \frac{j_{F,1,1}}{4F} \tag{A2-2}$$

BC at $x = 0$, $y = 0$ and $y = w$:

$$\mathbf{n} \cdot \nabla \widetilde{P}_{C,1,1} = 0 \tag{A2-3}$$

BC at $x = l$:

$$\widetilde{P}_{C,1,1} = 0 \tag{A2-4}$$

Hydrogen mole fraction:

$$\frac{Ph_A}{R_g T_g}(j\omega)\, y_{H_2,1,1} = D_{H_2,H_2O}\frac{Ph_A}{R_g T_g}\nabla^2 y_{H_2,1,1} - \nabla \cdot \left(y_{H_2,1,1}\nabla \widetilde{P}_A + y_{H_2}\nabla \widetilde{P}_{A,1,1}\right) - \frac{j_{F,1,1}}{2F} \tag{A2-5}$$

BC at $x = 0$:

$$y_{H_2,1,1} = 0 \tag{A2-6}$$

BC at $x = l$, $y = 0$ and $y = w$:

$$\mathbf{n} \cdot \nabla y_{H_2,1,1} = 0 \tag{A2-7}$$

Water mole fraction:

$$\frac{Ph_A}{R_g T_g}(j\omega)\, y_{H_2O,1,1} = D_{H_2,H_2O}\frac{Ph_A}{R_g T_g}\nabla^2 y_{H_2O,1,1} - \nabla \cdot \left(y_{H_2O,1,1}\nabla \widetilde{P}_A + y_{H_2O}\nabla \widetilde{P}_{A,1,1}\right) + \frac{j_{F,1,1}}{2F} \tag{A2-8}$$

BC at $x = 0$:

$$y_{H_2O,1,1} = 0 \tag{A2-9}$$

BC at $x = l$, $y = 0$ and $y = w$:

$$\mathbf{n} \cdot \nabla y_{H_2O,1,1} = 0 \tag{A2-10}$$

Oxygen mole fraction:

$$\frac{Ph_C}{R_g T_g}(j\omega)\, y_{O_2,1,1} = D_{O_2,N_2}\frac{Ph_C}{R_g T_g}\nabla^2 y_{O_2,1,1} - \nabla\cdot\left(y_{O_2,1,1}\nabla\widetilde{P}_C + y_{O_2}\nabla\widetilde{P}_{C,1,1}\right) - \frac{j_{F,1,1}}{4F} \quad \text{A2-11}$$

BC at $x = 0$:

$$y_{O_2,1,1} = 0 \quad \text{A2-12}$$

BC at $x = l$, $y = 0$ and $y = w$:

$$\mathbf{n}\cdot\nabla y_{O_2,1,1} = 0 \quad \text{A2-13}$$

Local current density and voltage equations:

$$V_{1,1} = \frac{\partial V}{\partial y_{H_2}} y_{H_2,1,1} + \frac{\partial V}{\partial y_{H_2O}} y_{H_2O,1,1} + \frac{\partial V}{\partial y_{O_2}} y_{O_2,1,1} + \frac{\partial V}{\partial j_F} j_{F,1,1} + \frac{\partial V}{\partial j_C} j_{C,1,1} \quad \text{A2-14}$$

$$j_{C,1,1} = C_{dl}\,(j\omega)\,\frac{\partial \eta_{activation}}{\partial j_F} j_{F,1,1} \quad \text{A2-15}$$

$$1 = \iint_A \left(j_{F,1,1} + j_{C,1,1}\right) dA \quad \text{A2-16}$$

The above equations determine the first harmonic responses of local Faradaic current density $j_{F,1,1}$, capacitive current density $j_{C,1,1}$ and cell voltage $V_{1,1}$.

Table 2.4 Modified steady state governing equations for an oxidant crossover failure cell with H_2/H_2O fuel and O_2/N_2 oxidant gas.

Oxygen gas leak distribution:

$$\dot{R}_{O_2,par}(x,y) = L_{O_2} \cdot \mathcal{N}\left((x_d, y_d), \sigma^2\right) = L_{O_2} \frac{1}{\pi\sigma^2} \exp\left(-\frac{(x-x_d)^2 + (y-y_d)^2}{\sigma^2}\right) \quad \text{A3-1}$$

Reduced anode gas channel pressure:

$$0 = -\nabla^2 \widetilde{P}_A + \frac{1 - y_{O_2,d}}{y_{O_2,d}} \dot{R}_{O_2,par} \quad \text{A3-2}$$

where $y_{O_2,d}$ is the oxygen mole fraction at defect position.

Reduced cathode gas channel pressure:

$$0 = -\nabla^2 \widetilde{P}_C - \frac{j}{4F} - \frac{\dot{R}_{O_2,par}}{y_{O_2,d}} \quad \text{A3-3}$$

Hydrogen mole fraction:

$$0 = -\nabla J_{H_2} - \nabla \cdot \left(y_{H_2} \nabla \widetilde{P}_A\right) - \frac{j}{2F} - 2\dot{R}_{O_2,par} \quad \text{A3-4}$$

The molar diffusive fluxes J_{H_2} and J_{H_2O} are calculated based on Stefan-Maxwell equations for multi-component gas mixtures of H_2, H_2O and N_2.

$$0 = -\nabla J_{H_2O} - \nabla \cdot \left(y_{H_2O} \nabla \widetilde{P}_A\right) + \frac{j}{2F} + 2\dot{R}_{O_2,par} \quad \text{A3-5}$$

Oxygen mole fraction:

$$0 = D_{O_2,N_2} \frac{P h_C}{R_g T_g} \nabla^2 y_{O_2} - \nabla \cdot \left(y_{O_2} \nabla \widetilde{P}_C\right) - \frac{j}{4F} - \dot{R}_{O_2,par} \quad \text{A3-6}$$

Lumped gas temperature:

$$0 = h_{conv}\left(T_s - T_g\right) - \nabla \cdot H\left(T_g\right) - \frac{j}{2F} \Delta\overline{H}_{elec} + 2\dot{R}_{O_2,par} \Delta\overline{H}_{elec} \quad \text{A3-7}$$

2.6.2 Appendix B: Model Parameters

Table 2.5 SOFC geometric parameters.

Symbol	Parameter	Value	Units
A	Cell active area	8.0×10^{-3}	m^2
l	Cell length	0.09	m
w	Cell width	0.0889	m
h_A	Anode height	1.5×10^{-3}	m
h_C	Cathode height	1.5×10^{-3}	m

Table 2.6 Fixed operating condition diagnostics' operating condition.

Symbol	Parameter	Value	Units
P	Gas pressure	1.013×10^5	Pa
$T_{g,in}$	Gas inlet temperature	1023.15	K
$y_{H_2,in}$	Anode gas inlet hydrogen mole fraction	0.8	1
$y_{O_2,in}$	Cathode gas inlet oxygen mole fraction	0.21	1
i	Cell current	20	A
U_f	Fuel utilization	80%	1
U_a	Air utilization	15%	1

Table 2.7 Cross-condition diagnostics' operating condition range.

Symbol	Parameter	Value	Units
P	Gas pressure	1.013×10^5	Pa
$T_{g,in}$	Gas inlet temperature	1023.15	K
$y_{H_2,in}$	Anode gas inlet hydrogen mole fraction	$0.5 - 0.99$	1
$y_{O_2,in}$	Cathode gas inlet oxygen mole fraction	0.21	1
i	Cell current	$10 - 30$	A
U_f	Fuel utilization	$50 - 80\%$	1
U_a	Air utilization	$5 - 20\%$	1

Table 2.8 Physical parameters.[101]

Symbol	Parameter	Value	Units
D_{H_2,H_2O}	H_2 H_2O binary diffusion coefficient	7×10^{-4}	m^2/s
D_{O_2,N_2}	O_2 N_2 binary diffusion coefficient	1.7×10^{-4}	m^2/s
kt_s	Lumped solid conductivity	0.05	W/K
h_{conv}	Heat transfer coefficient between gas and solid	150	$W/(m^2.K)$
κ	Heat transfer coefficient between the solid and gas temperature at the fuel cell entrance and exit	2.5	$W/(m.K)$
Φ_{wall}	Thermal flux from the fuel cell wall	0	W/m

Table 2.9 Aging degradation electrochemistry parameter range.

Symbol	Parameter	Value	Units
R_{Ohmic}	Ohmic specific resistance	$2.0 \times 10^{-5} - 1.4 \times 10^{-4}$	$\Omega.m^2$
j_0	Exchange current density	$1.0 \times 10^3 - 1.0 \times 10^4$	A/m^2
C_{dl}	Double layer capacitance	$1.0 - 100$	F/m^2

Table 2.10 Pristine cell electrochemistry parameters.

Symbol	Parameter	Value	Units
R_{Ohmic}	Ohmic specific resistance	2.0×10^{-5}	$\Omega.m^2$
j_0	Exchange current density	1.0×10^4	A/m^2
C_{dl}	Double layer capacitance	100	F/m^2

Chapter 3

MACHINE REINTERPRETATION OF REFERENCE ELECTRODE MEASUREMENT WITH INTENTIONAL MISALIGNMENT IN PROTON-EXCHANGE MEMBRANE ELECTROLYZER

3.1 Introduction

Separating contributions from each half-cell reactions in proton-exchange membrane (PEM) electrolyzer system are of great interest to researchers. Using a reference electrode (RE) to study individual electrode reaction separately is a simple practice in aqueous electrochemistry system. However, the design of one in solid electrolyte such as PEM is subjected to geometric constraints by the micron-thin electrolyte. One typical design is that shown in Figure 3.1, where the membrane electrode assembly (MEA) is extended and the reference electrode is placed outside of the active current path.

Extensive modelling works have shown the challenges in the quantitative interpretation of measurement with this straight-forward design. The creation of a potential field along the electrolyte material by a direct current (DC) necessitates considering the electrolyte

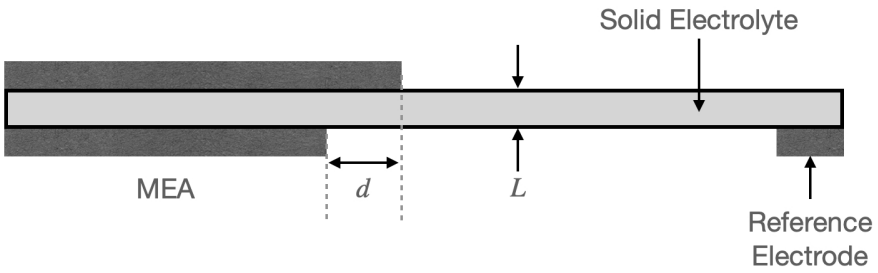

Fig. 3.1 Typical reference electrode arrangement in solid electrolyte systems.

potential distribution in reference electrode measurements. Practically, misalignment of between electrodes' edges are unavoidable due to fabrication limitations. For thin electrolyte, the slightest misalignment can result in inconsistent measurements for identical systems. In solid oxide fuel cell (SOFC), studies have demonstrated that asymmetrical current distribution along the electrode edge biases the potential measured by the reference electrode significantly toward the overhanging electrode.[129,130] Offsetting the two electrodes on both ends by a misalignment factor, represented by the d/L ratio, greater than 4, the simulated voltage difference measured between reference electrodes reflect a Nernst potential, rendering reference measurement meaningless.[130] In another publication, Adler showed that the edge effect also creates frequency dispersion and inductive artifacts in half-cell impedance that can lead to erroneous interpretation.[131] The severity of impedance distortion, not only depends on electrodes' misalignment, but also discrepancies between electrodes kinetic resistance and response time constant. Even when the electrodes are perfectly aligned, impedance distortion persists for asymmetric electrodes.[131] He & Van Nguyen investigated the edge effect in PEM fuel cell systems, where kinetics are slower and non-linear, leading to outcomes distinct from the linear kinetics observed in SOFCs. He & Van Nguyen simulation suggested that the d/L ratio must significantly exceed 20 for the reference potential to equate that at the overhanging cathode.[132] Additionally, the reference electrode measurement is a complex function of cell voltage and misalignment factor.[132]

In PEM literature, there have been other adaptations of reference electrode design, such as embedding dynamic hydrogen electrodes between half-MEAs.[133–138] Researchers have reported stability in reference electrode performance and successfully qualitatively and quantitatively assessed cell electrochemistry. Each electrodes polarization contributions can be quantified once the electrolyte Ohmic drop from each half has been accounted for with high frequency resistance measurements.[135–138] Through FEM simulation in Lithium-ion system, Ender *et al.* found that wire-type and mesh-type reference placed between active electrodes like these, are also less prone to impedance artefacts compared to the extended electrolyte or point-type design. However, these adaptations are limited to multiple-membrane-layer cells,

while commercial PEM fuel cells and electrolyzers are transitioning toward thinner, single-membrane cells. In addition, embedded wire, mesh or micro-electrodes can deteriorate or shift over long-term testing, and cannot be fixed post assembly. In more recent works, a non-embedded setup has been used to study PEM fuel cell and electrolyzer. Workers used Nafion salt-bridge and Nafion impregnated porous transport layers (PTL), providing an ionic path to the catalyst layer surface inside the active area on either anode and cathode side.[139–141] Nevertheless, the extensive modification of hardware and components is harder to adapt and can impact phenomena specific to the PTL-catalyst interface.

In this work, we revisit the use of an external reference electrode with intentionally misaligned electrodes in PEM electrolysis. The external reference electrode is preferred for its flexibility with different MEAs and cell components, requiring minimal modifications to a regular setup. Building upon simulations by He & Van Nguyen, in a similar kinetic regime as ORR in PEM fuel cell, we may use a reference electrode to study OER in PEM electrolysis with reproducible anode-cathode misalignment. We also want to investigate the distortion from asymmetry in half-cell EIS for the non-linear OER kinetic, presented previously by Adler for SOFC, and Ender *et al.* for Lithium-ion battery.[131,142]. Our objective is to deconvolute these distortions cause by the anode-edge potential distribution and determine the true kinetic overpotential of the half-cell reactions.

This research is motivated by the expanding literature on machine learning applications in electrochemistry. In PEM fuel cells literature, researchers effectively employed data-driven techniques for fault detection and diagnosis.[14,98,99,101] In battery state of health monitoring, there are many reports of successful machine prediction from battery charge discharge curves and impedance spectroscopy.[13,37,40,41,43,72–75,143–147] These works laid out various frameworks to process and analyze polarization and impedance data, from applying statistical model, sensitivity analysis, dimensionality reduction, etc, to address different research problems. Even more promisingly, authors were able to predict battery behavior from partly or entirely synthetic data, generated from physics-based models or generative AI.[37,40,72–75,145–147] Similar to electrochemical systems diagnosis, reference electrode data are compounded by factors

that change through long-term testing, operating conditions or cell-to-cell variation, such as kinetics degradation, membrane thickness or conductivity. Fitting data to physics model with a lot of unknown parameters can be demanding in both time and computational resources. Insteaed, our approach involves training a machine learning surrogate model with synthetic data from FEM simulation to predict the OER kinetic, then evaluate its applicability on experimental data.

3.2 Experimental

3.2.1 Catalyst Coated Membrane Fabrication

Catalyst coated membranes (CCMs) were ultrasonic spray-coated directly onto different membranes: Nafion^{TM} 212 (Chemours), Nafion^{TM} 115 (Chemours), and Nafion^{TM} 117 (Chemours). The cathode catalyst was was Pt on high surface area carbon (Pt/HSC, Tanaka Kikinzoku Kogyo, TEC10E50E) with targeted ionomer (Nafion D2020) to carbon ratio of 0.45:1, and targeted catalyst loading of 0.1 mgPt cm^{-2}. Anode catalyst was unsupported Ir oxide (Alfa Aesar) with ionomer (Nafion D2020) to catalyst ratio of 0.27:1, and targeted loading of 0.4 mg Ir cm^{-2}. Fabrication details are described else where.[148,149] The geometry of the catalyst layers (CL) is described in Fig. 3.2.

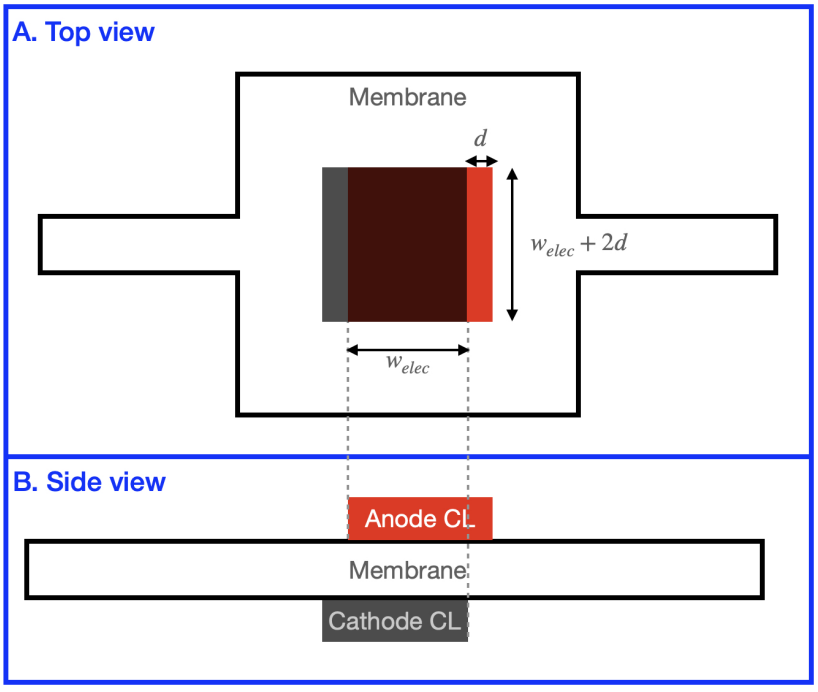

Fig. 3.2 Schematic of catalyst coated membrane from (A) the top view and (B) the side view. w_{elec} denotes the width where anode and cathode catalyst overlap and d denotes the electrode overhang distance.

The catalyst layers were positioned so that one would overhang over the other on each side. The MEAs were fabricated with an overlapping electrode width of w_{elec} = 13.42 mm, an overhang distance of d = 4.47 mm, and but varying misalignment factor (d/L ratio) as Nafion 212, 115 and 117 have nominal thickness of 50, 127 and 183 μm respectively.[150]

3.2.2 Electrolysis Cell Assembly

Figure 3.3 provides the cross-section view of the electrolysis cell assembly. The cell components, aside from the CCM, based of the Future Generation Membrane Electrode Assembly ("FuGeMEA") suggestion by the U.S. Department of Energy's H2NEW consortium.[151] The anode porous transport layer (PTL) was 5 cm^2 platinum coated titanium felt (Bekaert, 2GDL100.25) which had 56% porosity and 250 μm thickness. The cathode gas diffusion layer (GDL) was 5 cm^2 carbon paper (AvCarb, MGL280) which was 280 μm thick pre-compression, at approximately 20% compression. The flow field plates (FFP) were Pt/Au (anode/cathode) coated titanium.

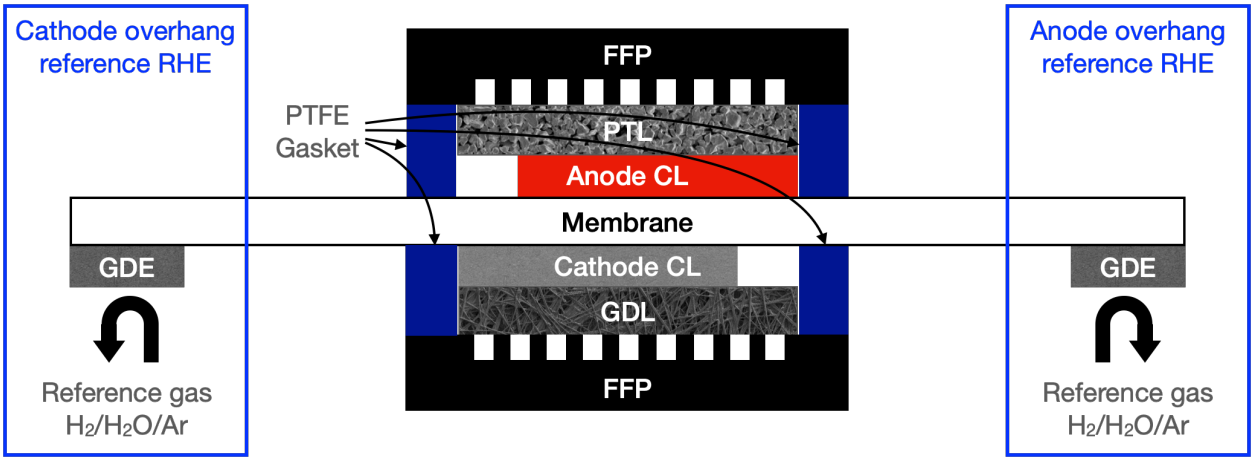

Fig. 3.3 Schematic of electrolysis cell assembly and hydrogen electrodes.

The reference reversible hydrogen electrode (RHE) was a gas diffusion electrode (GDE) in contact with the extended membrane in a dilute hydrogen gas environment. The gas diffusion electrode (GDE) was 0.3 mg/cm^2 40% Platinum on Vulcan - Carbon Cloth (Fuel

Cell Store, W1S1010). This was housed in an assembly of stainless steel current collector, groved Ultem pieces, and tubing for gas flow to and from the GDE. The housing assembly was designed by the National Renewable Energy Laboratory (NREL). The reference gas was a 5% : 95% molar H_2 : Ar mixture, humidified through a glass gas bubbler at room temperature.

3.2.3 Electrolyzer Cell Testing

Cell testing was carried out under dry-cathode condition with an anode water flow of 40 mL min^{-1} at 80 ^oC. The cell was heated to 80 ^oC with control thermocouple and cartridge heaters placed in the titanium FFPs. Before reference electrode testing, a pre-conditioning process was implemented involving a series of current and voltage holds, followed by several polarization curves until the performance stabilized. Pre-conditioning process, also referred to as break-in, is a standard practice in PEM fuel cell to stabilize performance at beginning of life.[152,153]

During reference electrode testing, each reference RHE received a gas flow of approximately 20 sccm. Polarization curves and impedance experiments were conducted using an EnergyLab XM Potentiostat/Galvanostat with a 100A/6V booster. In a polarization experiment, a 4-electrode configuration was employed, measuring the current, cell voltage (between the anode current collector and cathode current collector), anode voltage (between the anode current collector and anode-overhang RHE current collector), and cathode voltage (between the cathode current collector and cathode-overhang RHE current collector). Voltage readings were averaged over the last 10 seconds of 2-minute current holds. In an EIS experiment, after 3 minute current hold to ensure the cell reached steady state, we applied a 20 mV sinusoidal perturbation to the cell voltage. We simultaneously recorded the cell and the two half-cell impedance, measured from anode and cathode to one of the RHEs in 3-electrode configuration. We recorded voltage and impedance measurements for 26 current densities, up to 4 A/cm^2. Nearly a third of these were less than 0.2 A/cm^2, as the lower current density region was expected to be more informative of kinetic.

3.3 Physics Model

3.3.1 Steady state model with Butler-Volmer kinetics

The governing equations and boundary conditions for the 2-D geometry in Fig. 3.3 are similar to those presented in other simulation works.[129,130,132] The governing equation of the electrolyte potential is the conservation of charge:

$$\nabla^2 \Phi = 0 \tag{3.1}$$

Where Φ is the potential in the electrolyte.

The boundary at insulating surfaces is zero flux or zero current:

$$\mathbf{n} \cdot (-k \nabla \Phi) = 0 \tag{3.2}$$

Where $\mathbf{n}$ is the surface normal vector, and k is the membrane conductivity.

The electrode boundary condition is the total current equals the sum of Faradaic and capacitive current density. The electrode-electrolyte interface is expressed as a constant phase element:

$$\mathbf{n} \cdot (-k \nabla \Phi) = j_F + Q \frac{\partial^\beta \eta}{\partial t^\beta} \tag{3.3}$$

Where j_F is the Faradaic reaction current density, Q is the constant phase element area specific capacitance, β is the constant phase element exponent, and η is the kinetic overpotential across the electrode.

We use Butler-Volmer kinetics for both electrodes:

$$j_F = j_0 \cdot [e^{\frac{\alpha_f F}{RT} \eta} - e^{-\frac{\alpha_r F}{RT} \eta}] \tag{3.4}$$

Where j_0 is the electrode exchange current density, α_f is the forward reaction charge transfer coefficient, α_r is the reverse reaction charge transfer coefficient, F is the Faraday constant,

R is the universal gas constant, and T is the temperature.

Assuming the same charge transfer coefficient for the forward and reverse reaction, $\alpha = \alpha_f = \alpha_r$, we get:

$$j_F = 2j_0 \cdot \sinh(\frac{\alpha F}{RT}\eta) \tag{3.5}$$

As denoted in Figure 3.4, we will use the subscript 1 for the top electrode (anode) and 2 for the bottom electrode (cathode), and use the bottom electrode as zero-potential, i.e. $V_2 = 0$. The voltage difference between the top electrode and the bottom electrode, V_1, is thus referred to as MEA voltage. This voltage is not the same as the cell voltage measured between current collectors, due to the Ohmic loss through the non-MEA components, e.g. FFPs, PTL, GDL, etc. The kinetic overpotentials at the electrode boundaries are:

$$\eta_1 = V_1 - E_{EQ} - \Phi \tag{3.6}$$

$$\eta_2 = \Phi - V_2 = \Phi \tag{3.7}$$

Where E_{EQ} is the equilibrium potential of the water electrolysis reaction ($H_2O \rightarrow \frac{1}{2}O_2 + H_2$) at temperature T. Using a temperature of 80 ^{o}C or 353 K, and 1 bar of pressure on both anode and cathode, we calculated an equilibrium potential of 1.17 V.

Substitute Eq. 3.6, 3.7, and symmetric Bulter-Volmer kinetics, Eq. 3.5 into the boundary condition in Eq. 3.3, we get the following equations for the two electrode-electrolyte boundaries:

$$BC\ 1 : \mathbf{n} \cdot (-k\nabla\Phi) = 2j_{0,1}\sinh[\frac{\alpha_1 F}{RT}(V_1 - E_{EQ} - \Phi)] + Q_1\frac{\partial^\beta(V_1 - E_{EQ} - \Phi)}{\partial t^\beta} \tag{3.8}$$

$$BC\ 2 : \mathbf{n} \cdot (k\nabla\Phi) = 2j_{0,2}\sinh[\frac{\alpha_2 F}{RT}\Phi] + Q_2\frac{\partial^\beta(\Phi)}{\partial t^\beta} \tag{3.9}$$

Where $j_{0,1}$, α_1, and Q_1 is the current exchange density, the charge transfer coefficient, and constant phase element's capacitance of the top electrode. Likewise, $j_{0,2}$, α_2, and Q_2 is the current exchange density, the charge transfer coefficient, and capacitance of the bottom

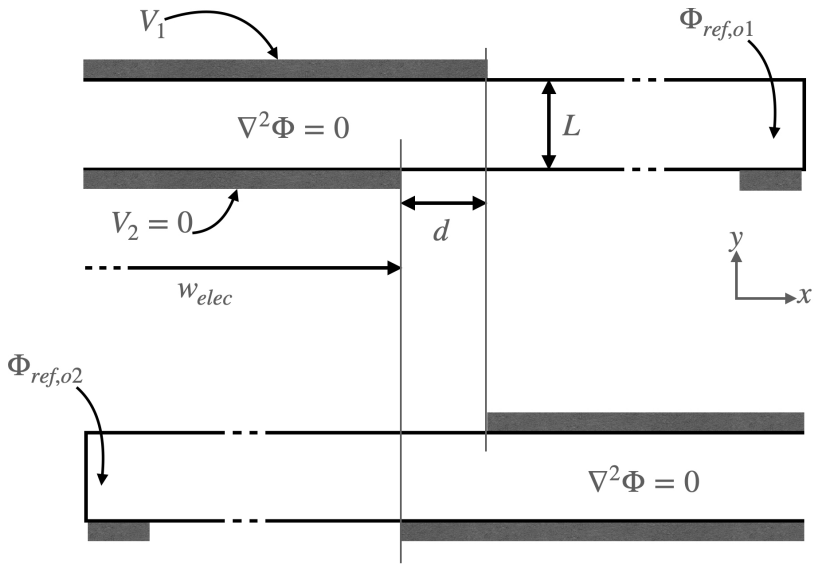

Fig. 3.4 Schematic of reference electrode geometry.

electrode. The time derivative from Eq. 3.8 and 3.9 is 0 under steady state assumption.

The current density, j_Σ, is calculated by integrating over the electrode boundary, divided by the overlapping electrode width, w_{elec}.

$$j_\Sigma = \frac{1}{w_{elec}} \int \mathbf{n} \cdot (-k\nabla\Phi)\, dx \tag{3.10}$$

The CCM has two equipotential zones where the electrolyte potential is measured with the two reference RHEs. As shown on Fig. 3.4, $\Phi_{ref,o1}$ stands for the electrolyte potential on the side where the top electrode is the overhanging electrode. Likewise, $\Phi_{ref,o2}$ is the electrolyte potential on the side where the bottom electrode is the overhanging electrode.

3.3.2 Impedance derivation

An AC oscillating voltage applied across from V_1 to V_2 can be written as:

$$V_1 - V_2 = V_1 = V_{1,ss} + \frac{\bar{V}}{2}(e^{i\omega t} + e^{-i\omega t}) \tag{3.11}$$

Where $V_{1,ss}$ is the steady state MEA voltage, $\bar{V}$ is the voltage perturbation amplitude, ω is the perturbation angular frequency, and i is the imaginary unity. The angular frequency (ω) is proportional to the standard frequency (f) in Hz:

$$\omega = 2\pi f \tag{3.12}$$

Under a steady oscillating cell voltage, with linear approximation to ignore second-order and higher harmonics, we can expect the all system variables to be separable in spatial and time-dependent terms, including electrolyte potential:

$$\Phi(\mathbf{x}, t) = \Phi_0(\mathbf{x}) + \Phi_{11}(\mathbf{x})\frac{\bar{V}}{2}(e^{i\omega t} + e^{-i\omega t}) \tag{3.13}$$

Where $\mathbf{x}$ is the spatial position vector, Φ_0 is the steady state electrolyte potential, and Φ_{11} is the first harmonic response of the electrolyte potential - Φ.

Application of Eq. 3.13 into Eq. 3.1 produces the governing equation for Φ_{11}:

$$\nabla^2\Phi_{11} = 0 \tag{3.14}$$

We can substitute Eq. 3.13 to Eq. 3.2 to get the following insulating surface boundary condition:

$$\mathbf{n} \cdot (-k\nabla\Phi_{11}) = 0 \tag{3.15}$$

Substitution of Eq. 3.11, 3.13 and the Taylor series expansion at the constant term (Φ_0) into Eq. 3.8 and 3.9, produces the following boundary condition at electrode surfaces:

$$BC\ 1 : \mathbf{n} \cdot (-k\nabla\Phi_{11}) = (1 - \Phi_{11})[Q_1(\omega)^\beta \exp(i\beta\frac{\pi}{2}) + \frac{2j_{0,1}\alpha_1 F}{RT}\cosh[\frac{\alpha_1 F}{RT}(V_1 - E_{EQ} - \Phi)]] \tag{3.16}$$

$$BC\ 2 : \mathbf{n} \cdot (k\nabla\Phi_{11}) = \Phi_{11}[Q_2(\omega)^\beta \exp(i\beta\frac{\pi}{2}) + \frac{2j_{0,2}\alpha_2 F}{RT}\cosh[\frac{\alpha_2 F}{RT}\Phi]] \tag{3.17}$$

Just as done with Φ, the cell current density can also be expressed as spatial and time-

dependent terms:

$$j_\Sigma(\mathbf{x},t) = j_{\Sigma,ss}(\mathbf{x}) + j_{\Sigma,11}(\mathbf{x})\frac{\bar{V}}{2}(e^{i\omega t} + e^{-i\omega t}) \tag{3.18}$$

Where $j_{\Sigma,ss}$ is the steady state current density and $j_{\Sigma,11}$ the first harmonic response.

By applying the above harmonic expansion to equation 3.10, we can solve for $j_{\Sigma,11}$:

$$j_{\Sigma,11} = \frac{1}{w_{elec}}\int \mathbf{n}\cdot(-k\nabla\Phi_{11})\,dx \tag{3.19}$$

To get the impedance across the electrodes (from V_1 to V_2), we use the ratio of the voltage harmonic to that of the current density:

$$Z = \frac{1}{j_{\Sigma,11}} \tag{3.20}$$

The half-cell impedance of the top electrode, measured from V_1 to Φ_{ref}, is:

$$Z_1 = \frac{1-\Phi_{ref,11}}{j_{\Sigma,11}} \tag{3.21}$$

The half-cell impedance of the bottom electrode, measured from V_2 to Φ_{ref}, is:

$$Z_2 = \frac{\Phi_{ref,11}}{j_{\Sigma,11}} \tag{3.22}$$

The half-cell impedance can be measured with either RHEs. To distinguish them, $Z_{1,o1}$ refers to the top electrode impedance measured with the top-overhang side reference potential - $\Phi_{ref,o1}$, and $Z_{1,o2}$ refers to the top electrode impedance measured with the bottom-overhang side reference potential - $\Phi_{ref,o2}$. Same convention is used for the bottom electrode half-cell impedance.

3.3.3 Nondimensionalized model for both electrodes with Butler-Volmer kinetics

Steady state model

To abridge the dimensional model, the following scheme is used to make a non-dimensional model. We use the electrolyte thickness (L) as the length dimension. The misalignment factor, ratio between overhang distance and electrolyte, is referred to as λ, i.e. $\lambda = d/L$.

The dimensionless potential, Ψ is:

$$\Psi = \frac{\Phi}{\Phi^*} \tag{3.23}$$

Where Φ^* is:

$$\Phi^* = \frac{RT}{\alpha_1 F} \tag{3.24}$$

This is equivalent to the Tafel slope of the OER kinetic divided by $\ln(10)$.

Replace the Laplace operator with the dimensionless operator, $\tilde{\nabla} = \nabla \times L$, we derive the following governing equation for Ψ from Eq. 3.1:

$$\tilde{\nabla}^2 \Psi = 0 \tag{3.25}$$

The insulating boundary condition derived from Eq. 3.2 is:

$$\mathbf{n} \cdot (-\tilde{\nabla}\Psi) = 0 \tag{3.26}$$

The electrode boundary conditions from Eq. 3.8 and 3.9 become:

$$BC\ 1 : \mathbf{n} \cdot (-\tilde{\nabla}\Psi) = \frac{\kappa_1}{\lambda} \sinh(\gamma - \Psi) \tag{3.27}$$

$$BC\ 2 : \mathbf{n} \cdot (\tilde{\nabla}\Psi) = \frac{\kappa_2}{\lambda} \sinh(\theta\Psi) \tag{3.28}$$

Where:

$$\gamma = \frac{V_1 - E_{EQ}}{\Phi^*} \tag{3.29}$$

$$\kappa_1 = \frac{2j_{0,1}d}{k\Phi^*} \tag{3.30}$$

$$\kappa_2 = \frac{2j_{0,2}d}{k\Phi^*} \tag{3.31}$$

$$\theta = \frac{\alpha_2}{\alpha_1} \tag{3.32}$$

The dimensionless number κ_1 and κ_2 expresses ratios between non-linear kinetic of the electrodes and the lateral ionic conduction, i.e. secondary to primary potential distribution.

From Eq. 3.10, the dimensionless cell current density, $\bar{j_\Sigma}$ is:

$$\bar{j_\Sigma} = \frac{j_\Sigma}{j^*} = \frac{1}{w_{elec}} \int_{w_{elec}} \mathbf{n} \cdot (-\tilde{\nabla}\Psi)\, dx \tag{3.33}$$

Where the dimension for current density is:

$$j^* = \frac{k\Phi^*}{L} \tag{3.34}$$

Impedance derivation

Following a similar process in Section 3.3.2, Ψ_{11}, the nondimensional first harmonic of Ψ, has the following governing equation:

$$\tilde{\nabla}^2\Psi_{11} = 0 \tag{3.35}$$

At the insulating boundary:

$$\mathbf{n} \cdot (-\tilde{\nabla}\Psi_{11}) = 0 \tag{3.36}$$

At the electrode boundary:

$$BC\ 1 : \mathbf{n} \cdot (-\tilde{\nabla}\Psi_{11}) = \frac{\kappa_1}{\lambda}(1 - \Psi_{11})[\sigma \exp{(i\beta\frac{\pi}{2})} + \cosh(\gamma - \Psi)] \tag{3.37}$$

$$BC\ 2 : \mathbf{n} \cdot (\tilde{\nabla}\Psi_{11}) = \frac{\kappa_2}{\lambda}\Psi_{11}[\sigma\chi\frac{\kappa_1}{\kappa_2} \exp{(i\beta\frac{\pi}{2})} + \theta \cosh(\theta\Psi)] \tag{3.38}$$

Where:

$$\bar{\omega} = \frac{2j_{0,1}}{Q_1\Phi^*} = \frac{2j_{0,1}\alpha_1 F}{Q_1 RT} \tag{3.39}$$

$$\sigma = \frac{\omega^\beta}{\bar{\omega}} \tag{3.40}$$

$$\chi = \frac{Q_2}{Q_1} \tag{3.41}$$

The full cell and half-cell impedance spectra are normalized by the electrolyte Ohmic area specific resistance, $Z^* = \frac{L}{k}$:

$$\bar{Z} = \frac{Z}{Z^*} = Z\frac{k}{L} \tag{3.42}$$

$$\bar{Z}_1 = Z_1\frac{k}{L} \tag{3.43}$$

$$\bar{Z}_2 = Z_2\frac{k}{L} \tag{3.44}$$

Where $\bar{Z}$, $\bar{Z}_1$, and $\bar{Z}_2$, are the dimensionless cell, top electrode, and bottom electrode impedance respectively.

The dimensionless full cell impedance, as derived from Eq. 3.19 and 3.20 is:

$$\bar{Z} = \frac{\Phi^*}{j^*\bar{j}_{\Sigma,11}} \times \frac{k}{L} = \frac{1}{\frac{1}{w_{elec}}\int \mathbf{n} \cdot (-\tilde{\nabla}\Psi_{11})\ dx} \tag{3.45}$$

The dimensionless half-cell impedance derived from Eq. 3.21 and 3.22 is:

$$\bar{Z}_1 = \frac{1 - \Psi_{ref,11}}{\bar{j}_{\Sigma,11}} \tag{3.46}$$

$$\bar{Z}_2 = \frac{\Psi_{ref,11}}{\bar{j}_{\Sigma,11}} \tag{3.47}$$

Where $\Psi_{ref,11}$ is the first harmonic response of the dimensionless reference electrolyte potential, Ψ_{ref}.

3.3.4 Voltage breakdown

The voltage of the electrolyzer cell can be treated as a summation of the thermodynamic voltage, and other processes' losses or overpotentials.[154,155]

$$\Delta V = E_{EQ} + (\eta_{Ohmic} + \eta_{kinetic} + \eta_{transport}) \tag{3.48}$$

Where η_{Ohmic} is the Ohmic voltage loss, $\eta_{kinetic}$ is voltage loss from kinetic activation, and $\eta_{transport}$ is the sum of transport-related losses.

The cell overpotential, $\Delta V - E_{EQ}$, subtracted by the Ohmic loss, is called the HFR-free overpotential, $\eta_{HFR-free}$:

$$\eta_{HFR-free} = \Delta V - E_{EQ} - \eta_{Ohmic} = \eta_{kinetic} + \eta_{transport} \tag{3.49}$$

In the physics model, HFR-free overpotential equals to the sum of the two electrode kinetic overpotentials as the model doesn't include any transport process, i.e. $\eta_{transport} = 0$.

$$\eta_{HFR-free} = \eta_{kinetic} = \eta_1 + \eta_2 \tag{3.50}$$

To derive these kinetic overpotentials, we approximate a near uniform current distribution where the electrodes overlap, and zero current at the overhanging edges.[130,132] The anode and cathode electrode kinetic overpotentials, can be derived from dimensionless quantities from boundary conditions Eq. 3.27 and 3.28:

$$\eta_1 \approx \sinh^{-1}\left(\frac{\bar{j}_\Sigma \lambda}{\kappa_1}\right) \times \Phi^* \tag{3.51}$$

$$\eta_2 \approx \sinh^{-1}\left(\frac{\bar{j_\Sigma}\lambda}{\kappa_2}\right) \times \frac{\Phi^*}{\theta} \tag{3.52}$$

The Ohmic loss of the cell is given by:

$$\eta_{Ohmic} = HFR \times j_\Sigma \tag{3.53}$$

Where HFR is the area-specific high frequency resistance (HFR) from impedance measurement or simulation.

For the MEA domain we simulate, HFR is approximately the membrane area specific resistance:

$$HFR_{MEA} \approx \frac{L}{k} = Z^* \tag{3.54}$$

3.4 Simulation Methodology

We used COMSOL Multiphysics to simulate the electrochemical measurements described in Section 3.2.3 from the dimensionless model in Section 3.3.3. We created a model to predict the polarization curve and another model to predict full-cell and half-cell EISs. The values or range of values used in simulation can be found in Table 3.4 and 3.5. The range listed aims to encompass values reported in literature and estimation from experimental data when applicable. To efficiently explore the parameter space, we used the quasi-random Sobol's sampling method.[123] The Sobol's sampling algorithm was taken from SALib open-source python package.[124]

3.5 Results and Discussion

3.5.1 Polarization simulation results

A polarization curve was simulated using parameters from Table 3.7 as the base case to discuss the implications of our physics model. We calculated the kinetic overpotentials from anode and cathode, and compared it to the potential the reference electrodes measure in Fig. 3.5.

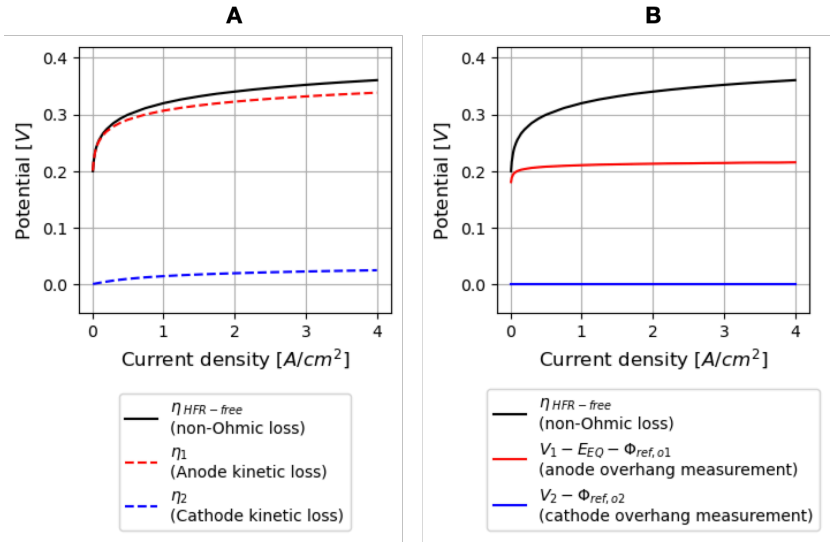

Fig. 3.5 Four-electrode polarization simulation using parameters from Table 3.7. (A) True voltage loss breakdown and (B) 4-electrode measurements.

In Fig. 3.5 A, the two kinetic losses, sum up to the HFR-free overpotential, or the total kinetic loss. In Fig. 3.5 B, the potential difference between the cathode overhang reference and the cathode ($\Phi_{ref,o2} - V_2$) is approximately zero at all current density even as the cathode kinetic loss (η_2) increases with current density. This implies that the cathode-overhang RHE does not provide any meaningful measurement of the cathode kinetic. The sufficiently large misalignment, $d/L = 10$, causes overpotential from the fast cathode HER kinetic to dissipate away from the electrode edge. This agrees with previous situations described in simulation

studies of SOFC and hydrogen oxidation reaction in PEM fuel cell.[130,132] The situation on the anode for oxygen evolution reaction (OER) is different. The anode-overhang measurement ($V_1 - E_{EQ} - \Phi_{ref,o1}$), though does not equal to zero, underestimates the true OER kinetic loss (η_1). These results are similar to what He & Van Nguyen simulated for ORR kinetic in PEM fuel cell.[132]

The anode-overhang measurement depends both on the misalignment factor (d/L) and the anode kinetic dimensionless number(κ_1). We illustrate this on Fig. 3.6 and Fig. 3.7, comparing the simulation results between the base case in Fig. 3.5 against larger overhang and faster kinetic.

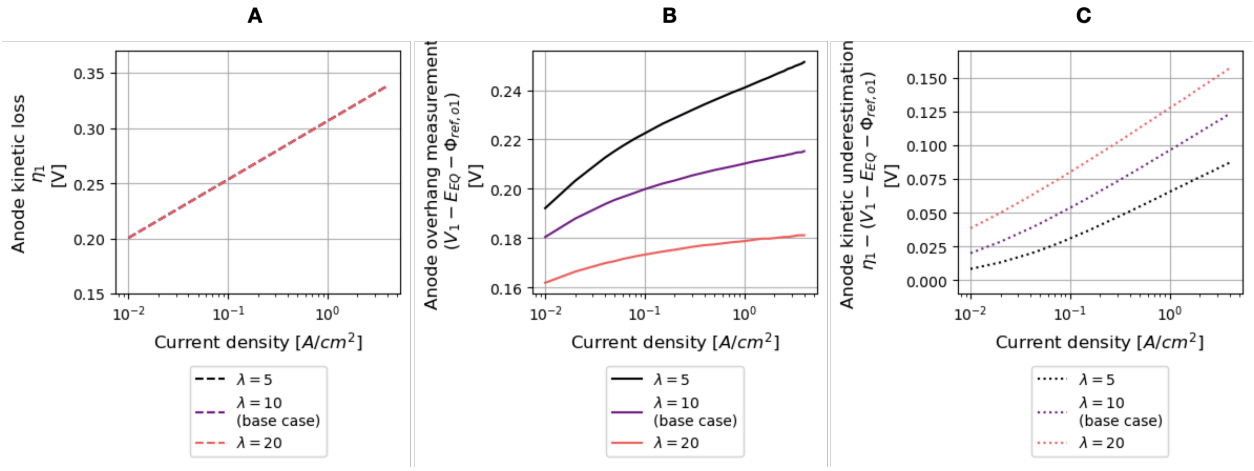

Fig. 3.6 Anode kinetic loss compared to anode-overhang measurement with different misalignment factor - d/L. (A) True kinetic loss, (B) anode overhang reference electrode measurement, and (C) difference between true anode kinetic overpotential and reference measurement.

In Fig. 3.6 (A), as the kinetic of the electrode remains unchanged, the kinetic loss is the same for different overhang distances. As the overhang grows larger, the anode overhang reference reading becomes smaller (Fig. 3.6 (B)), and underestimates more of the true kinetic loss (Fig. 3.6 (C)). Figure 3.7 compares different anode dimensionless kinetic number - κ_1. With faster kinetic, i.e. smaller κ_1, the anode kinetic loss and the anode overhang

measurement get smaller. However, the difference between the two stays same, Fig. 3.7 (C). These simulations meant to illustrate that the electrolyte potential at the overhang reference electrode is a complicated function of both misalignment factor and cell current density or cell voltage for OER electrode in PEM electrolyzer. The non-linear kinetic doesn't follow the linear secondary current distribution analytical solution laid out by Winkler *et al.*.[129] Although these trends can be observed, we were unable to find an analytical solution to the reference electrode measurement without the 2-dimensional FEM model.

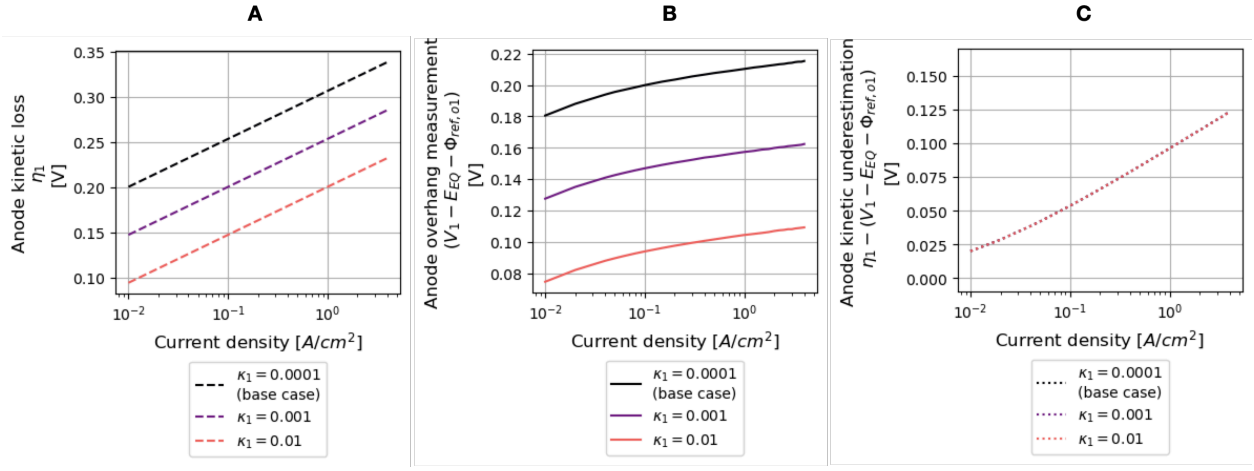

Fig. 3.7 Anode kinetic loss compared to reference electrode measurement with different kinetic rates - κ_1. (A) True kinetic loss, (B) anode overhang reference electrode measurement, and (C) difference between true anode kinetic overpotential and reference measurement.

3.5.2 Polarization experimental data and simulation comparison

The raw experimental data are provided in the supplementary Section 3.8.1. We achieved reproducible performance after preconditioning of the cells as seen in the repeated polarization experiments with different 3-electrode and 4-electrode setups, as well as stable reference electrode voltage readings.

To find OER and hydrogen evolution reaction (HER) overpotentials from the raw polarization curve, we needed RHE potential of the H^+/H_2 redox couple. The electrolyzer was at 80^{o}C, while the Pt reference electrodes outside of the cell assembly were at 25 ^{o}C. We calculated a H^+/H_2(g) RHE potential of 22.5 (mV) for the reference gas, accounting the difference in H_2 partial pressure, and proton activity at the different temperatures:[156,157]

$$\Delta E_{RHE} = -\frac{RT}{F}\ln(\frac{\sqrt{p_{H_2}}}{\sqrt{1}}\frac{a_{H^+,80^oC}}{a_{H^+,25^oC}}) \tag{3.55}$$

where p_{H_2} is H_2 partial pressure in bar, and a_{H^+} is the proton activity. The proton activity for Nafion membrane is 0.8 at room condition and 2.4 at 80^{o}C.[157] The reference gas is a 2%:98% H_2:Ar mixture, humidified through a bubbler at 25^{0}C.

The physics model doesn't account for Ohmic resistances from components of the cell assembly outside the MEA such as PTL, GDL, FFP or current cables. The cell HFR is a summation of HFRs from the MEA, cathode and anode side non-MEA components:

$$HFR_{cell} = HFR_{MEA} + HFR_{anode} + HFR_{cathode} \tag{3.56}$$

These HFRs were determined from 3-electrode EISs for all electrolyzer cells and provided in the supplementary Section 3.8.2. The cathode-side and anode-side non-MEAs HFRs (HFR_{anode} and $HFR_{cathode}$) were unsurprisingly independent of current density. However, the cell HFR (HFR_{cell}) decreased with current density, so we used a 3-degree polynomial fit to derive its value at different current densities. A possible explanation for the current density dependency is that Joule heating can increase membrane temperature and improve

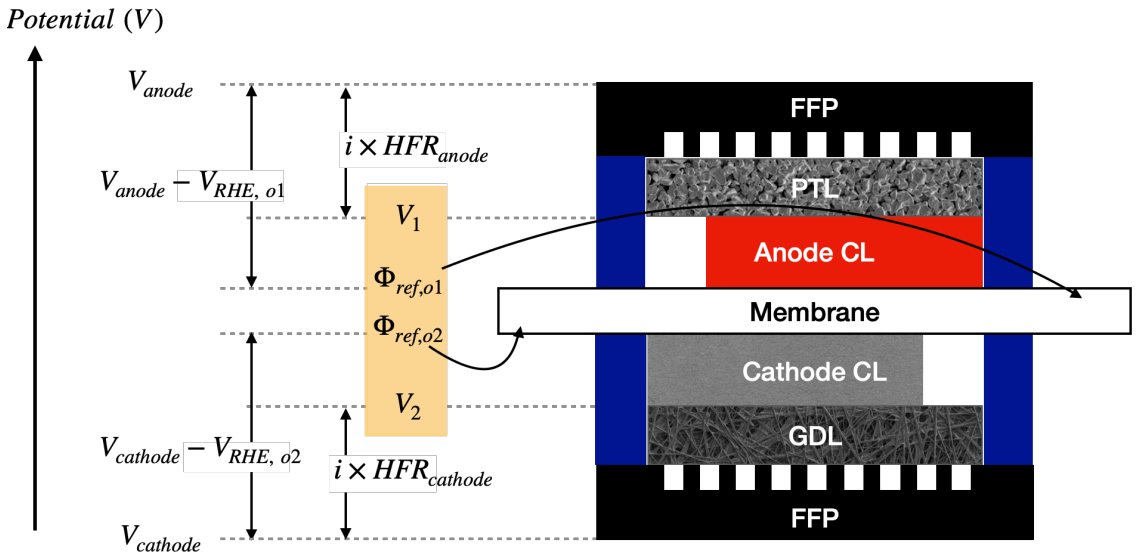

Fig. 3.8 Potential diagram of the electrolyzer cell. Variables highlighted in yellow are simulated with the physics model.

Nafion proton conductivity.[158–161]

From the 4-electrode polarization curve, the anode, cathode and cell overpotentials were calculated by subtracting corresponding reversible potentials and HFRs. For clarity, these different potential levels are shown in Fig. 3.8. The derivation from voltage and HFRs to physics-model potential levels is provided in the following equations:

$$\eta_{cell,\ HFR-free} = V_{cell} - i_{\Sigma} \times HFR_{cell} - E_{EQ} \tag{3.57}$$

$$(V_1 - E_{EQ} - \Phi_{ref,o1}) = V_{anode,o1} - i_{\Sigma} \times HFR_{anode} - E_{EQ} + \Delta E_{RHE} \tag{3.58}$$

$$(\Phi_{ref,o2} - V_2) = V_{cathode,o2} - i_{\Sigma} \times HFR_{cathode} - \Delta E_{RHE} \tag{3.59}$$

Where $\eta_{cell,\ HFR-free}$, equating to the HFR-free voltage subtracted by the reversible electrolysis voltage, E_{EQ}, is a measure of total all non-Ohmic losses, such as kinetics and mass transport.

The HFR or iR-compensated variables we derived from the experimental data is shown

in Fig. 3.9.

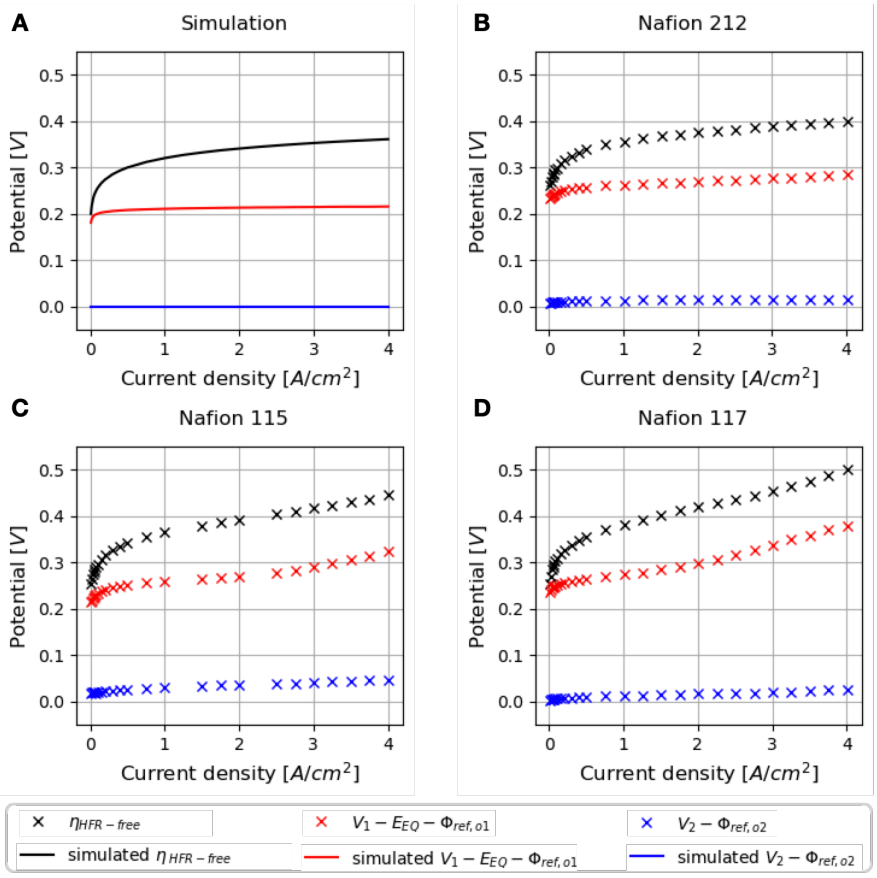

Fig. 3.9 Simulated polarization (A) versus iR-compensated values from experimental data for (B) Nafion 212, (C) Nafion 115, and (D) Nafion 117. Nafion 115 has two data points missing.

The cathode overhang RHE consistently registers approximately 0 V for Nafion 212 and Nafion 117, with no variation with increased current density, aligning with the predictions of the physics model. Unexpectedly, in the case of Nafion 115 (Fig. 3.9 (C)), the cathode overhang measurement ranges from 20-50 mV, higher than the anticipated 0 V. This discrepancy may stem from a worse-than-expected HER kinetic or a deviation in the reference RHE voltage due to an error in conducting the experiment or setting up the reference electrodes. An alternative explanation for the marginal overpotential detected by the cathode overhang

RHE is that the platinum-coated porous transport layer (PTL), though significantly less kinetically active compared to iridium oxide, might have catalyzed the oxygen evolution reaction (OER) and influenced the potential distribution.

Nafion 212 closely mirrors to the behaviors of the physics model simulation. The HFR-free overpotential curve aligns with the simulated Butler-Volmer kinetic, exhibiting a steep increase in voltage loss near 0 current density and plateauing at higher current density. The anode overhang measurement exhibits a non-zero overpotential that rapidly reaches a plateau, consistent with the physics model predictions outlined in Section 3.5.1. However, deviations from predicted behaviors emerge for Nafion 115 and Nafion 117: the HFR-free overpotential and the anode overhang measurements appear to increase linearly at current density above 2 A/cm^2, not plateauing or leveling-off. This could be caused by transport limitation occuring at higher current density, which is not considered in the physics model. At high current density operation, membrane hydration, water transport and catalyst layer transport can affect cell performance.[148,154,162] The qualitative value of using reference electrode to measure transport losses at the overhanging electrode were previously discussed by He & Van Nguyen. The authors simulated tertiary potential distribution where oxygen transfer become limited due to flooding at higher current density operation of PEM fuel cells.

3.5.3 EIS experimental data and simulation comparison

Figure 3.10 presents the results of the full cell and half-cell impedance using the cathode-overhang RHE for Nafion 212 cell at three different current densities. On the anode, large positive imaginary values are observed at high frequencies (f $>$ 1 kHz), likely caused by wire mutual inductance. On the cathode, the artefact of mutual inductance presents as large negative imaginary values for the same frequency range. Mutual inductance from current cables on the sense leads are equal and opposite hence their effects mostly cancelled out on the cell impedance. Using the cathode-side impedance, we determined the Ohmic resistance of non-MEA cathode components(FFP, GDL and current collector) from the HFR.

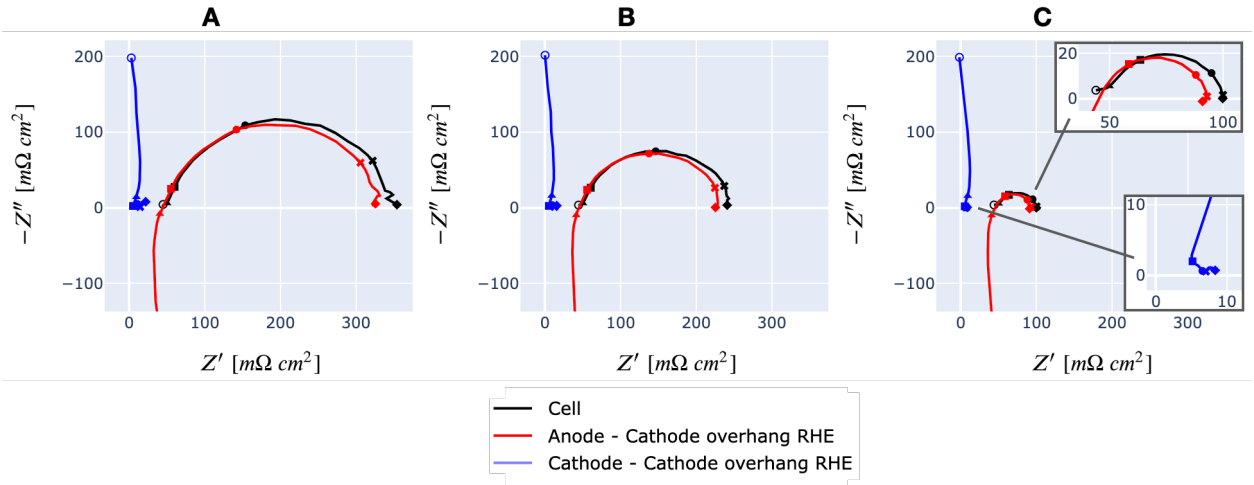

Fig. 3.10 Cathode-overhang EIS of Nafion 212 electrolyzer cell at (A) 0.05, (B) 0.1, and (C) 0.5 A/cm^2. The ○, ▲, ■, ●, ×, ◆, symbols indicate 10 kHz, 1 kHz, 100 Hz, 10 Hz, 1 Hz, and 0.1 Hz respectively.

Figure 3.11 shows the base case EIS simulation at the same current densities, with Nafion 212's anode and cathode HFRs added. The physics model predicts that the equipotential line can be drawn directly from the cathode nonreactive edge to the reference position. Consequently, the cathode impedance exhibits virtually no kinetic or electrolyte Ohmic loss. As a results, in the MEA domain simulated, cathode impedance ($Z_{2,o2}$) would be zero across

frequency and the anode impedance ($Z_{1,o2}$) would be the same as the cell impedance. Without real impedance offset from the non-MEA HFRs, the simulated anode and cell impedance would superimpose.

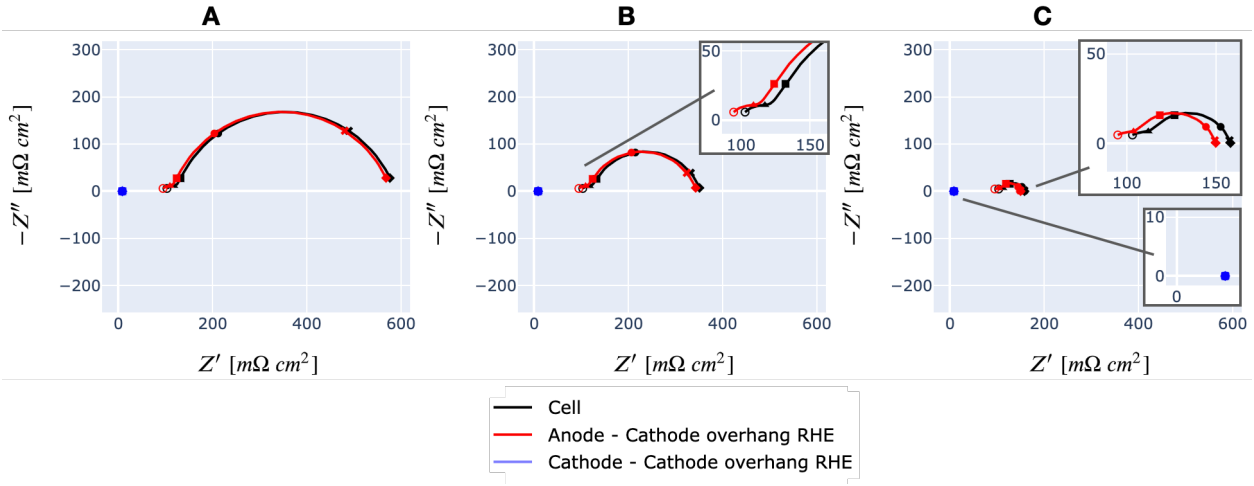

Fig. 3.11 Cathode-overhang EIS simulation using Nafion 212 anode and cathode-side HFR values and parameters in Table 3.7 at (A) 0.05, (B) 0.1, and (C) 0.5 A/cm^2. The ○, ▲, ■, ●, ×, ◆, symbols indicate 10 kHz, 1 kHz, 100 Hz, 10 Hz, 1 Hz, and 0.1 Hz respectively.

The experimental data aligns mostly with the predictions from the physics model. Excluding the high-frequency range affected by mutual inductance, the cathode half-cell real impedance remains at nearly the same magnitude. The Nyquist plot shows one main semicircular shape at low frequency ($f < 100Hz$) in the cell impedance. In the simulated EIS, this is a result of anode's constant phase element in parallel with the OER Bulter-Volmer kinetics. The data and simulation are consistent with the OER kinetic is often the primary contributor to polarization resistance of water electrolysis. At higher frequencies, a smaller semicircle is observed on the left side of the larger semicircle, visible in the zoomed-in views of cell EIS in Fig. 3.10 (C) and of EIS simulation in Fig. 3.11 (C). In the simulated EIS, this comes from the cathode HER kinetic. However, it cannot be determined via visual inspection of experimental EIS which half-cell this polarization resistance belong to.

Figure 3.12 shows EIS impedance using the anode-overhang RHE for Nafion 212 cell, and

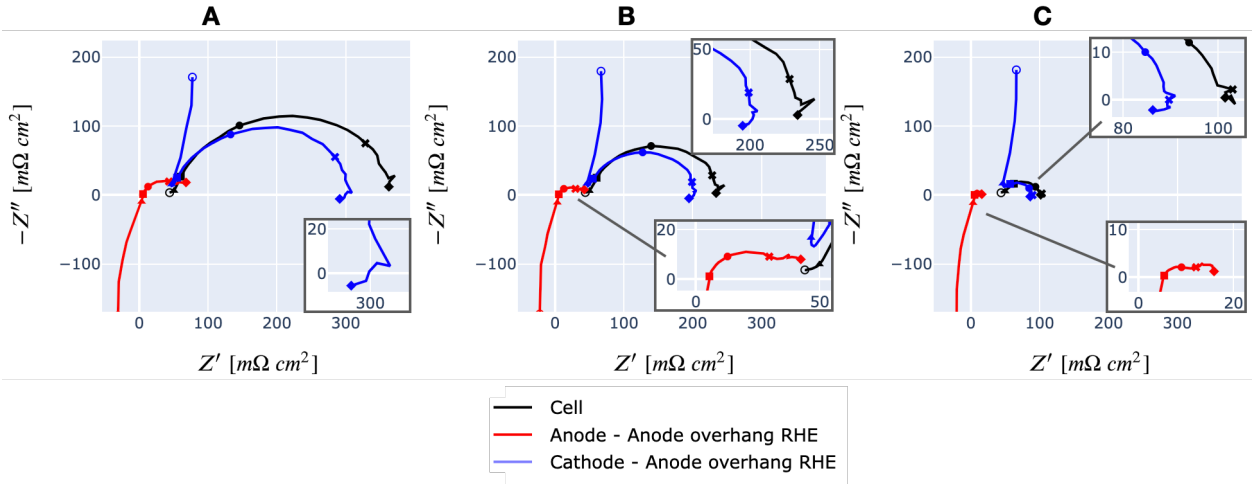

Fig. 3.12 Anode-overhang EIS of Nafion 212 electrolyzer cell at (A) 0.05, (B) 0.1, and (C) 0.5 A/cm^2. The ○, ▲, ■, ●, ×, ◆, symbols indicate 10 kHz, 1 kHz, 100 Hz, 10 Hz, 1 Hz, and 0.1 Hz respectively.

Figure 3.13 the base-case EIS simulation with non-MEA components HFRs added. Both experiment and physics model demonstrates a frequency-dependent non-zero anode impedance. This frequency-dependent behavior is elucidated further in Figure 3.14, plotting the first harmonic of the electrolyte potential (Ψ_{11}) for the base case simulation. At high frequencies, the electrolyte conductivity dominates the potential distribution. The equipotential line shows that the potential measured by the reference electrode equals that at anode surface so anode impedance measures none of the electrolyte resistance. As the frequency decreases ($\omega \to 0$), the anode electrode get polarized, the potential distribution converges toward the steady state solution, and the anode impedance picks up some of OER polarization loss. For both experimental and simulated EIS, the cathode impedance exhibits a small inductive loop at the low frequency end.

The polarization feature of anode impedance has some discrepancies between the Nafion 212 experimental data and the simulation. In Fig. 3.13, at all three current densities, the simulated anode impedance exhibits a spiral shape sometimes observed in non-linear EIS reports,[163–166] and simulated for relative diffusion process.[167] The spiral shape may be

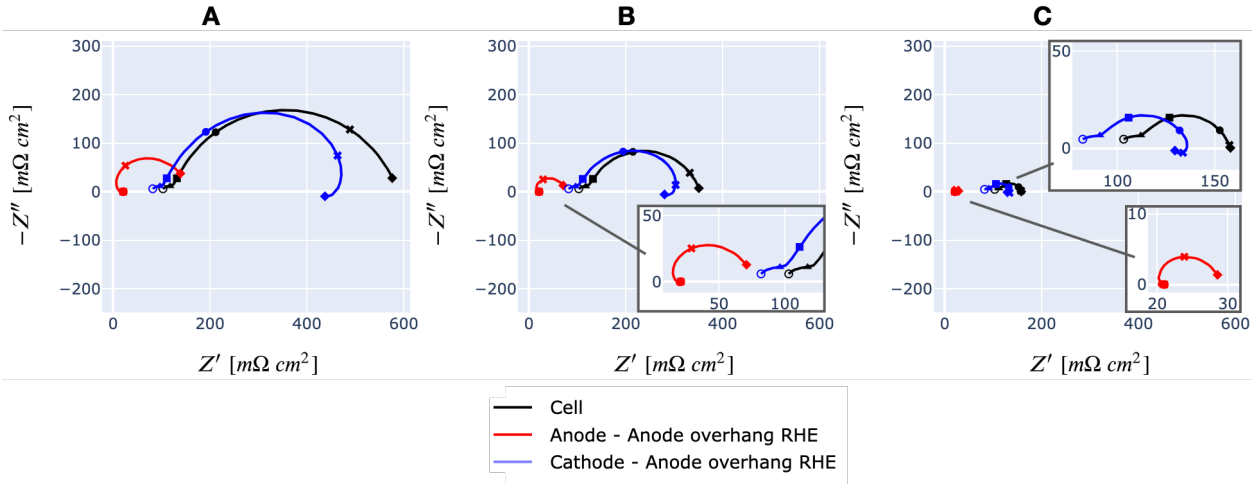

Fig. 3.13 Anode-overhang EIS simulation using Nafion 212 anode and cathode-side HFR values and parameters in Table 3.7 at (A) 0.05, (B) 0.1, and (C) 0.5 A/cm^2. The ○, ▲, ■, ●, ×, ◆, symbols indicate 10 kHz, 1 kHz, 100 Hz, 10 Hz, 1 Hz, and 0.1 Hz respectively.

caused by the non-linear distribution of potential field and potential harmonic. In Fig. 3.12 (B) and (C) zoom-in views, Nafion 212 anode impedance have a more dispersed shape, that could be interpreted as two joined semicircles. To better understand this difference, we need more experimentation with different catalyst layers and better control of the high-frequency system inductance. Our physics model also account for a symmetric Bulter-Volmer kinetics and assume a single capacitance for OER kinetic, which can be inaccurate or insufficient for the studied electrodes.

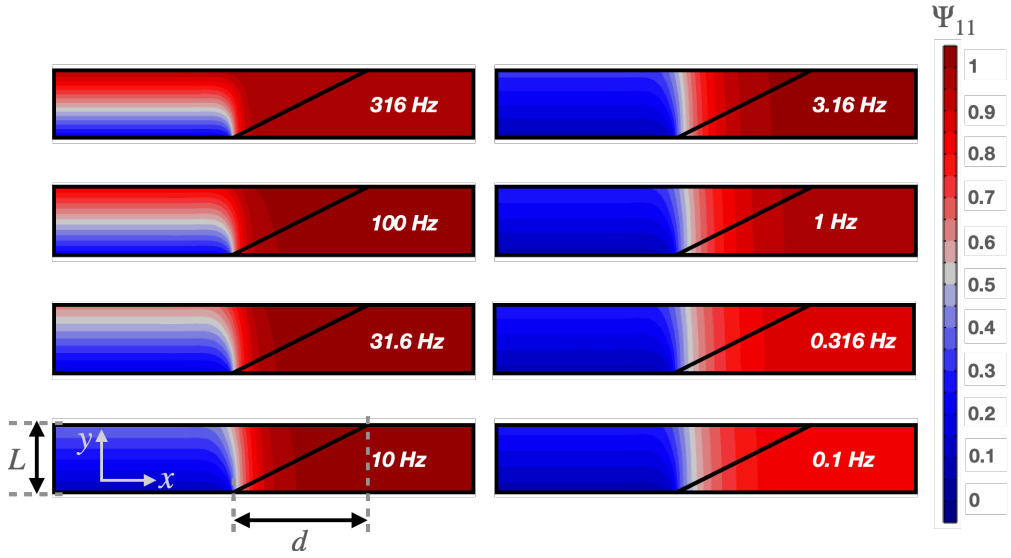

Fig. 3.14 EIS simulation complex potential distribution at 0.05 A/cm^2. The y:x scale is 5:1. The misalignment factor, d/L, is 10.

3.5.4 Machine prediction of kinetic losses from anode overhang RHE measurements

Polarization simulation sensitivity analysis

To examine how various parameters influence potential measurements at each point on the polarization curve, we conducted a variance-based Sobol sensitivity analysis within the explored parameter space. This analysis utilized the built-in function from the SALib open-source Python package.[124] Sobol sensitivty analysis decomposes the model output variance into summands of variances of the input parameters.[168] The total sensitivity index is shown in Fig. 3.15.

The sensitivity analysis of cell potential is consistent with electrochemistry we modeled. At the low current density, the parameters with the highest impact are κ_1 and Φ^*, which are parameters of the OER kinetic (Eq. 3.24 and 3.30). This is probably because kinetic overpotential dominates the overall contribution to the electrolysis voltage at low current density. As current density increases, the importance shifts to Nafion conductivity (k) and thickness (L), which dictates the Ohmic resistance. Toward 4 A/cm^2, the cell measurement becomes predominantly sensitive to these two parameters. In the case of the cathode-overhang measurement, the total sensitivity indexes have large confidence interval, or high variance. This is attributed to the fact that the cathode-overhang potential is nearly, and is mostly insensitive to the HER kinetic, as discussed in Section 3.5.1 and consistent with prior simulation works of fast kinetics.[130,132]

Machine learning model inputs

The steady state model predicts the electrolyte potential at the two reference electrode positions ($\Phi_{ref,o1}$ and $\Phi_{ref,o2}$), and the MEA voltage from the top to bottom electrode ($V_1 - V_2$) for an applied current density (j_Σ). Using one set of physics model parameters whose range is listed in the Appendix Table 3.5, a single simulation returns these potentials at the 26 current densities used in the polarization experiment. Given our goal to characterize anode OER kinetic from polarization curve, the machine learning takes inputs from the anode-overhang

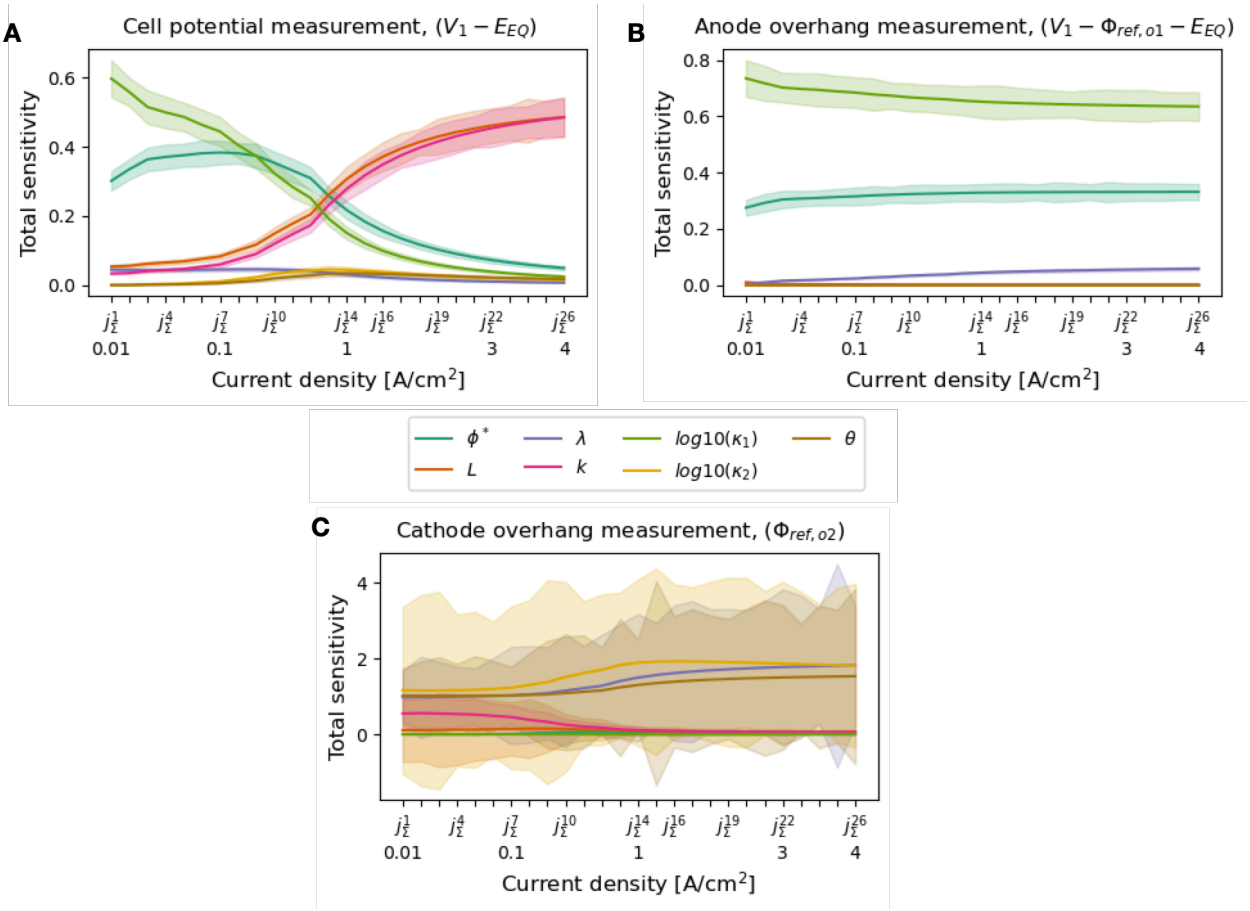

Fig. 3.15 Polarization measurement Sobol sensitivity to simulation parameter for (A) cell measurement, (B) anode-anode overhang RHE measurement, and (C) cathode-cathode overhang RHE measurement. The confidence interval for each parameters coefficient are plotted with lighter color value.

RHE measurements ($V_1 - E_{EQ} - \Phi_{ref,o1}$). To due to deviations between experimental data and simulation from possible transport process discussed in Section 3.5.2, only current densities less than or equal to 1 A/cm^2 are considered, reducing the number to 14 anode-overhang measurement inputs. The cathode overhang RHE measurements are excluded due to their ineffectiveness, as is the cell voltage which are confounded by both HER and OER kinetic. The k/L ratio, the electrolyte total resistance, which equals to the MEA's HFR, is treated as an input. The electrode misalignment distance, $d = L \times \lambda$, is used as an input since the

geometry of the catalyst layer position is known with reasonable confidence. This totals to a number of 16 input features.

Machine learning model outputs

To derive OER kinetic contribution, we needed three parameters: L, κ_1, and Φ^*. These are the unknown electrolyte thickness, the parameters associated with OER electrode kinetic exchange current density ($j_{0,1}$), and charge transfer coefficients (α_1). This results in a total of 3 regression outputs. In addition to the coefficient of determination, i.e. r^2-score for the output prediction, we used another metric to evaluate the machine learning model success which is the OER kinetic overpotential (η_1) calculated at 0.01, 0.1, and 1 A/cm^2 from Eq. 3.51.

Performance with synthetic dataset

The machine learning regressor with the most success was the multi-layer perceptron neural network (NN). These neural networks consist of up to three hidden layers, each with up to 200 neurons with Sigmoid activation function. We used a 60% : 40% training to testing data split of the 24,576 polarization simulations. The results are summarized in Table 3.1.

Table 3.1 Machine model r^2-score of simulated polarization data

Model		Electrolyte thickness L	OER kinetic dimensionless number κ_1	OER Tafel slope divided by ln (10) Φ^*	OER kinetic loss at 0.01 | 0.1 | 1 A/cm^2 η_1
NN	train score	0.885	0.938	0.805	0.967 | 0.973 | 0.978
	test score	0.881	0.931	0.789	0.964 | 0.970 | 0.976

Plots of train and test dataset prediction versus the true values are provided in the supplementary Section 3.8.3. We note that the accuracy of predictions for the three desired outputs may not meet the standard for certain objectives. The r^2-score of around 0.88 for

electrolyte thickness (L) is inadequate for monitoring membrane swelling or thinning. For the OER Tafel slope (Φ^*), the model scores less than 0.8, insufficient for catalyst performance or degradation studies. The dimensionless number κ_1 is a lumped metric of both the exchange current density and Φ^* so inaccurate Φ^* would affect the derived exchange current density. However, the OER kinetic loss at three different current densities derived from the three machine learning outputs, has high accuracy with $r^2 \geqslant 0.96$. Although the separate parameter predictions are not good on their own, they are sufficient at predicting OER kinetic loss.

Although feature importance are not readily available through the parameters of a MLP neural network, we can use permutation importance to evaluate the importance of the input features to the output predictions. Permutation importance calculates how the model performance is affected by random noise added to each features.[169] We used the open python package ELI5 to calculate the permutation importance using the mean squared error metric, and provide the analysis in the supplementary Section 3.8.3.[170] The lowest and largest current density measurements are the two most important features for all three model outputs. Considering the logarithmic relationship from Butler-Volmer equation, it is reasonable that the anode RHE measurement at the lowest current density would has the biggest influence on the prediction of the OER kinetic parameters (κ_1 and Φ^*). Both the permutation feature importance and the sensitivity analysis in Section 3.5.4 show indications that our models could be enhanced by incorporating more measurements at smaller current densities as inputs.

Model evaluation with experimental data

We applied the machine models on the experimental data for Nafion 212, 115 and 117 to create a kinetic breakdown prediction in Figure 3.16. The predicted OER kinetic loss is plotted against the total non-Ohmic loss of the cell, i.e. HFR-free overpotential, and the residual loss, obtained by subtracting the predicted OER loss from the total non-Ohmic loss. We expect this residual loss to be the HER kinetic overpotential. We also plot the prediction

for measurements with a ± 10 mV offset, to examine the effect of a potential offset that was suspected for Nafion 115 data discussed in Section 3.5.2. In practice, an potential offset can come from inadequate temperature control shifting the equilibrium water electrolysis voltage or factors affecting in the reference RHE potential. The RHE potential depends on proton activity in Nafion membrane which is influenced by the hydration state of the membrane, gas concentration and temperature.[157,159]

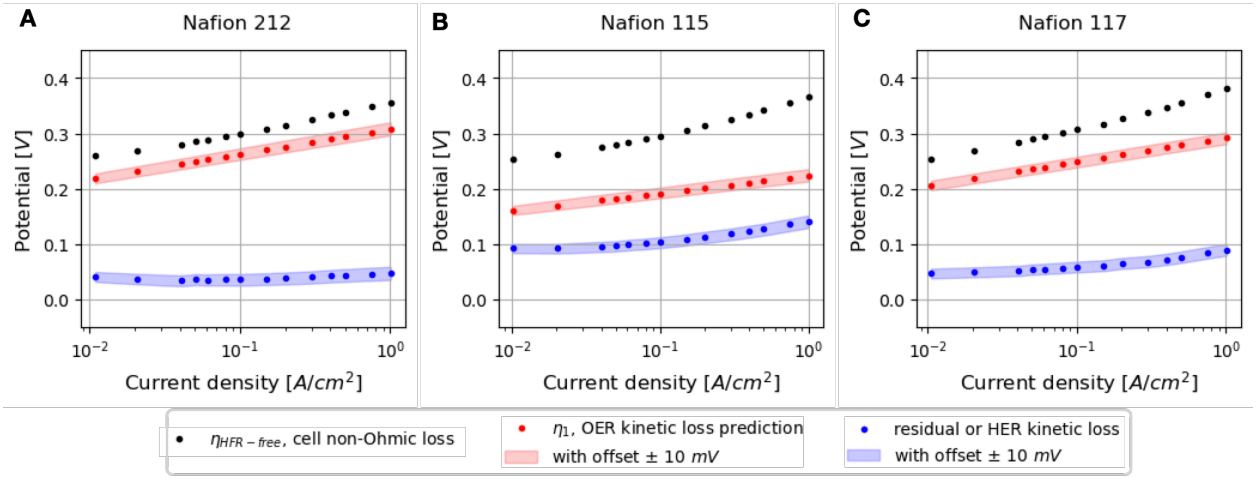

Fig. 3.16 NN OER kinetic prediction from the polarization data for (A) Nafion 212, (B) Nafion 115, and (C) Nafion 117.

The NN prediction indicates similar OER and HER kinetic losses between Nafion 212 and Nafion 117, as expected for similar MEA constructions. The prediction for Nafion 115 appears quantitatively different, with higher HER loss and lower OER loss. However, as mentioned in Section 3.5.2, experimental errors could have affected the RHE potential, thus, affecting the anode overhang measurements. This would have influenced the NN model prediction, causing an underestimation of the OER kinetic loss. Across the parameter space that we covered, at 1 A/cm^2, the OER kinetic overpotential is well-distributed between 100 - 600 mV (seen in the Supplemental Fig. 3.22) and the HER kinetic, between 0 - 300 mV. As the synthetic dataset is not biased towards a particular kinetic breakdown outcome, the NN prediction from the experimental data appears promising.

At present, we lack an internal reference electrode comparison or a catalyst loading study to support these kinetic breakdown results. These should be implemented in future study to confirm the rigor and validity of the NN model. Since we use a fairly standard MEA construction, we may compare our results with other PEM electrolysis studies. From the Nafion 212 and Nafion 117 neural network predictions, we reports a 50-100 mV HER overpotential and about 300 mV OER overpotential at 1 A/cm^2 and 80^{o}C for catalyst loading of 0.1 mg Pt cm^{-2} and 0.4 mg Ir cm^{-2}. Bühre *et al.* used a Nafion salt-bridge internal reference electrode to study PEM water electrolysis. They reports a HER overpotential of about 80 mV for the same current density with a higher Pt-loading (1 mg Pt cm^{-2}) and lower temperature (60^{o}C). Their iR-corrected OER kinetic is 350 mV for 2 mg Ir cm^{-2}. In PEM electrolysis modeling works, authors used values of 0.5-1 for charge transfer coefficient and 0.001-0.09 A/cm^2 for exchange current density, which amounts to 35-200 mV HER overpotential at 1 A/cm^2 and 80^{o}C.[171–174] For OER kinetic, modellers used a charge transfer coefficient of 2 and exchange current density between 1.0×10^{-12} and 1.0×10^{-7} A/cm^2, which amounts to a loss of 250 - 420 mV at 1 A/cm^2. Our HER and OER predictions are within these ranges.

3.6 Conclusions

The extended reference electrode design on thin electrolyte has been controversial due to the challenges in qualitatively interpreting the results. In the context of PEM water electrolyzers, our physics model demonstrates that the extended reference electrode design on an MEA of reproducible anode overhang distance, can be useful for qualitatively evaluating the anode electrode. Our main contribution is create a machine learning model to make quantitative interpretation of the reference measurement. From a synthetic dataset generated with the physics model, we trained a neural network to correlate the reference electrode measurement to its kinetic overpotential. The model works well on the training synthetic dataset and makes sensible kinetic breakdown of the experimental data. The fast and computationally-

inexpensive neural network is an attractive alternative to fitting polarization data into the FEM model.

Several avenues for future works have emerged from the analysis of simulation results and the implications from machine learning. The sensitivity analysis of the synthetic dataset and permutation importance evaluation of the neural networks suggests that they can be improved by including measurements at smaller current density. Observations from EIS simulations with electrode offset have piqued our interest in investigating whether it's possible to separate each electrode's capacitive effect from half-cell EIS. We were unable to examine this due this due to the limitations of the current synthetic dataset, which employs a single capacitance for each electrode. While overpotential readings depend on the reference potential, i.e. knowing and maintaining a steady reversible $H+/H_2$ potential in Nafion membrane, EIS or resistance-based measurements do not face the same constraint. With the current synthetic EIS dataset that consists of only one EIS per set of physics-based parameters, we have yet been successful at predicting the physics parameters. However, the use of multiple EISs at different current densities or a combination of EIS and polarization data may be worth exploring.

3.7 Acknowledgement

This project was made possible by components, materials and testing facility provided by Electric Hydrogen with the company's consent and support. The work is done in collaboration with Dr. Chaiwat Engtrakul, Dr. Sarah Blair and Dr. Elliot Padgett at the National Institute of National Renewable Energy Laboratory (NREL).

3.8 Supplementary

3.8.1 Polarization curve data

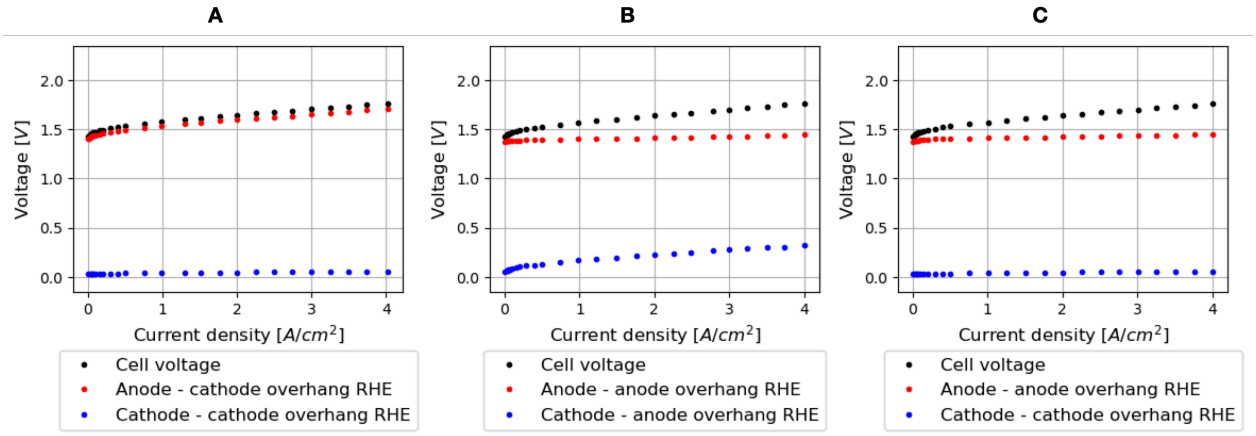

Fig. 3.17 Three-electrode and four-electrode polarization curves of Nafion 212. (A) Three-electrode using the cathode-overhang RHE. (B)Three-electrode using the anode-overhang RHE. (C) Four-electrode.

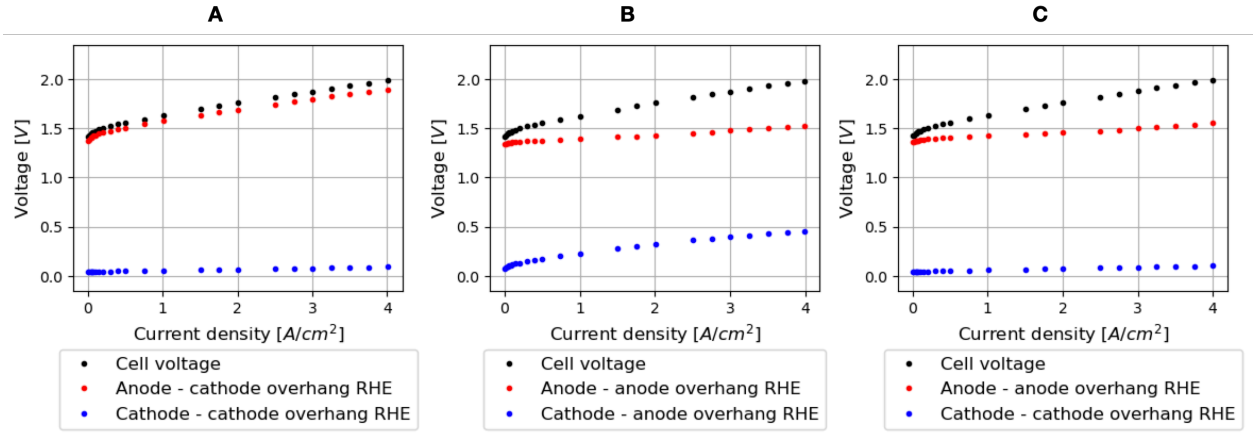

Fig. 3.18 Three-electrode and four-electrode polarization curves of Nafion 115. (A) Three-electrode using the cathode-overhang RHE. (B)Three-electrode using the anode-overhang RHE. (C) Four-electrode. Nafion 115 has two missing current density data points.

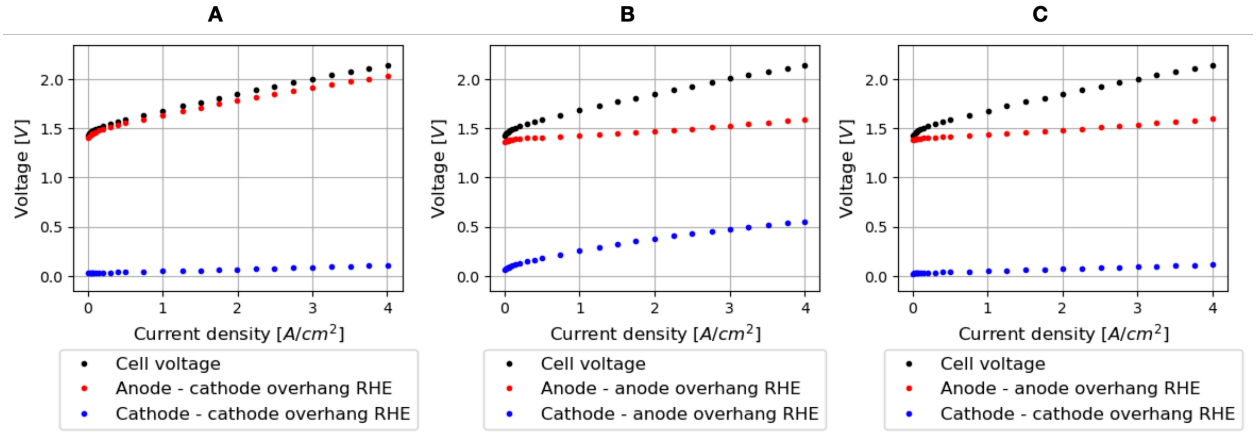

Fig. 3.19 Three-electrode and four-electrode polarization curves of Nafion 117. (A) Three-electrode using the cathode-overhang RHE. (B)Three-electrode using the anode-overhang RHE. (C) Four-electrode.

3.8.2 High frequency resistances

Table 3.2 Anode side high frequency resistance

Nafion ID	HFR value	Units
212	5.23 ± 0.09	$m\Omega.cm^2$
115	21.0 ± 0.5	$m\Omega.cm^2$
117	18.5 ± 0.2	$m\Omega.cm^2$

Table 3.3 Cathode side high frequency resistance

Nafion ID	HFR value	Units
212	5.07 ± 0.13	$m\Omega.cm^2$
115	8.24 ± 0.12	$m\Omega.cm^2$
117	17.3 ± 0.13	$m\Omega.cm^2$

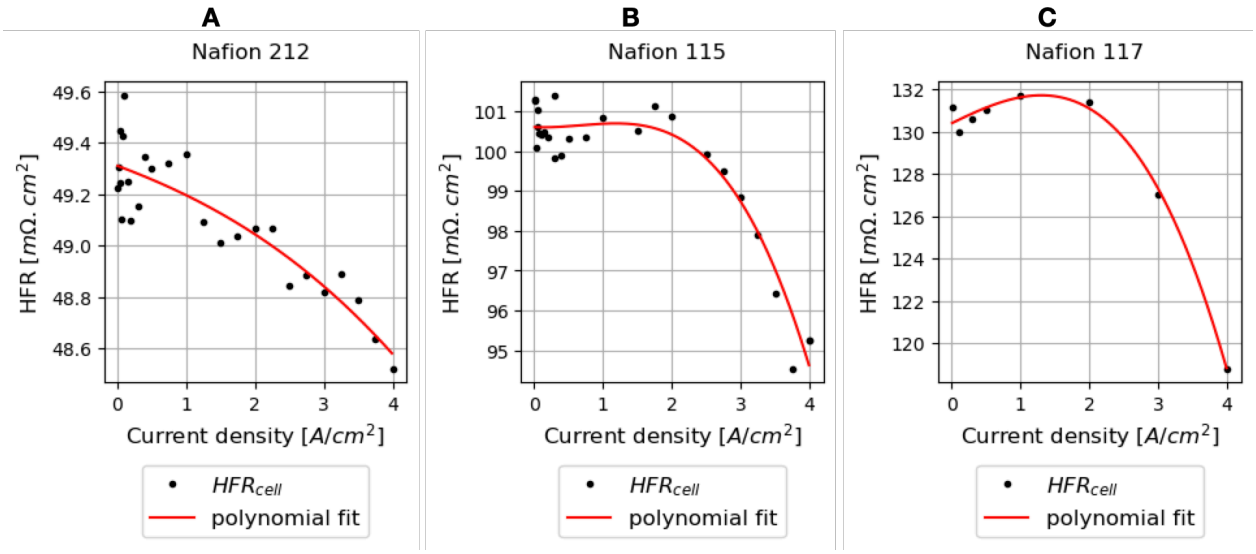

Fig. 3.20 Cell high frequency resistance at different current density for (A) Nafion 212, (B) Nafion 115, and (C) Nafion 117.

3.8.3 Polarization curve machine learning results

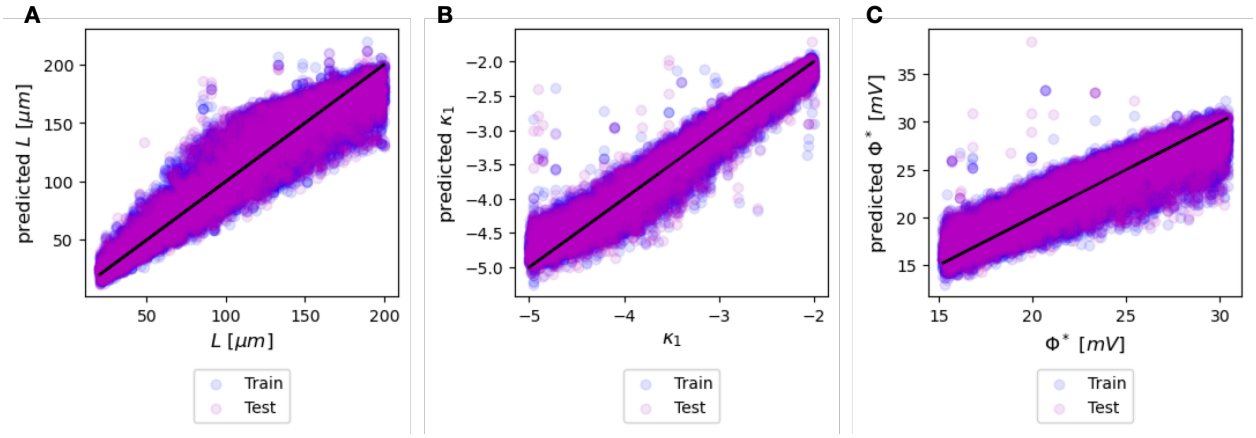

Fig. 3.21 Prediction versus true value - NN model trained on synthetic polarization data. (A) Electrolyte thickness - L, (B) OER kinetic dimensionless number - κ_1 and (C) OER Tafel slope divided by $\ln(10)$ - Φ^*.

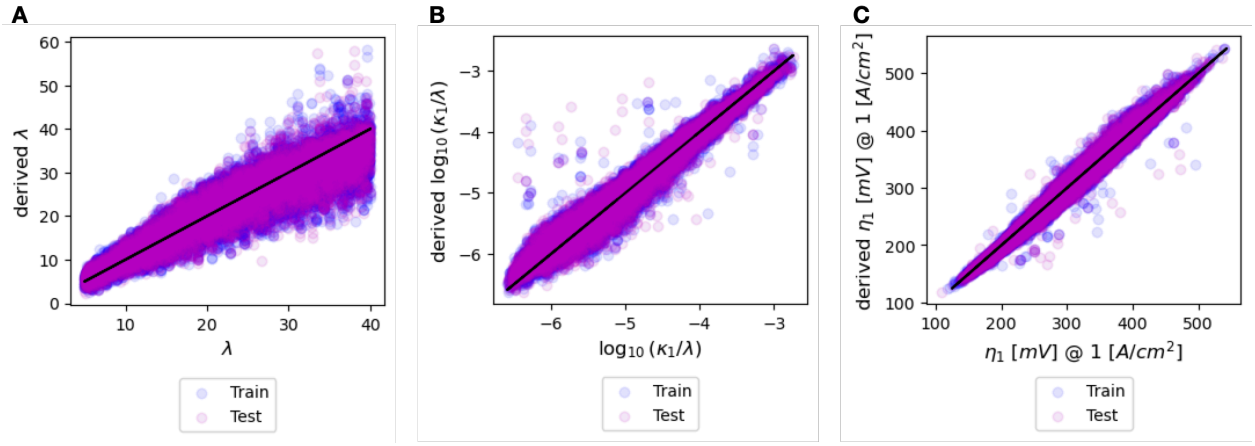

Fig. 3.22 Derived value versus true value - NN model trained on synthetic polarization data. (A) Misalignment factor - λ, (B) OER kinetic over thickness dimension conduction - $\frac{\kappa_1}{\lambda}$ and (C) OER overpotential at 1 A/cm^2 - η_1.

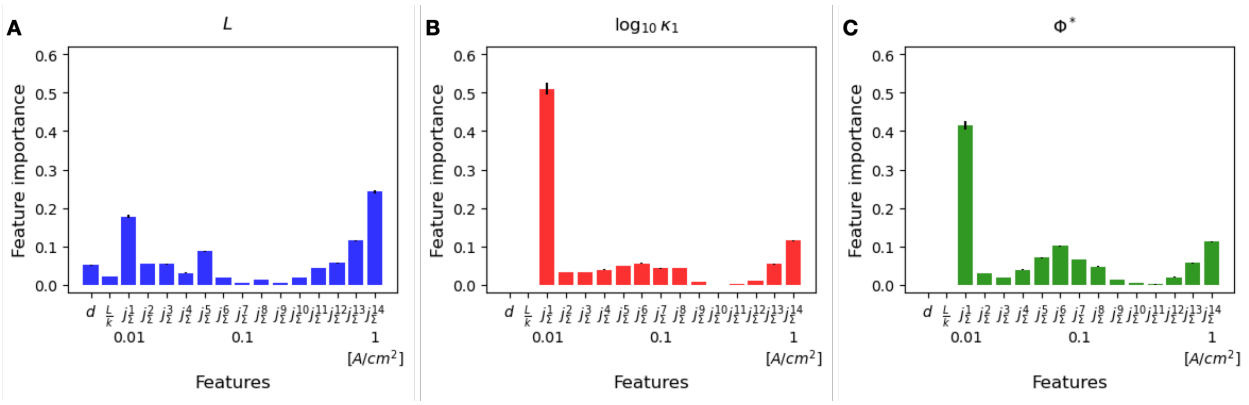

Fig. 3.23 Permutation feature importance for NN model trained on synthetic polarization data for (A) Electrolyte thickness - L, (B) OER kinetic dimensionless number - κ_1 and (C) OER Tafel slope divided by $\ln(10)$- Φ^*.

3.9 Appendix

Table 3.4 Geometry parameters.

Symbol	Parameter	Value or Range	Units
w_{elec}	Electrode width.	1.342	cm
L	Electrolyte thickness, from reported nominal Nafion^{TM} thickness.[150]	[20, 200]	μm
λ	Overhang distance to electrolyte thickness.	[5, 40]	1

Table 3.5 Electrochemistry model parameters in polarization curve simulation.

Symbol	Parameter	Value or Range	Units
E_{EQ}	Equilibrium potential of water electrolysis at 80^{o}C and 1 bar pressure.	1.17	V
Φ^*	OER Tafel slope in the Tafel-kinetic limit divided by ln (10)	[15.21, 30.42]	mV
k	Electrolyte proton conductivity	[5, 25]	S/m
κ_1	Top electrode dimensionless number.[141,148,175]	$[1 \times 10^{-5}, 1 \times 10^{-2}]$	1
κ_2	Bottom electrode dimensionless number.[141,171,176,177]	$[1 \times 10^{1}, 1 \times 10^{3}]$	1
θ	Charge transfer coefficient ratio.	[0.25, 5]	1
j_Σ	Operating current density.	[0.01, 4]	A/cm^2

Table 3.6 Electrochemistry model parameters in EIS simulation.

Symbol	Parameter	Value or Range	Units
E_{EQ}	Equilibrium potential of water electrolysis at 80^oC and 1 bar pressure.	1.17	V
Φ^*	OER Tafel slope in the Tafel-kinetic limit divided by $\ln(10)$	[15.21, 30.42]	mV
k	Electrolyte proton conductivity	[5, 25]	S/m
κ_1	Top electrode dimensionless number.[141,148,175]	$[1 \times 10^{-5}, 1 \times 10^{-2}]$	1
κ_2	Bottom electrode dimensionless number.[141,171,176,177]	$[1 \times 10^{1}, 1 \times 10^{3}]$	1
θ	Charge transfer coefficient ratio.	[0.25, 5]	1
γ	Normalized cell potential, equivalent to $V_1 \in [1.4, 1.7]\ V$.	[7, 17]	1
β	Constant phase element exponent.	[0.75, 1]	1
$\bar{\omega}$	Dimensionless frequency.	$[1 \times 10^{-4}, 1 \times 10^{-2}]$	1
χ	Ratio between the bottom electrode and top electrode capacitance.	$[1 \times 10^{-2}, 1]$	1

Table 3.7 Base case simulation parameters, used to simulate data shown in Section 3.5.2 and 3.5.3.

Symbol	Parameter	Value or Range	Units
w_{elec}	Electrode width.	1.342	cm
L	Electrode thickness, from reported nominal Nafion^{TM} thickness.	120	μm
λ	Overhang distance to electrolyte thickness.	10	1
Φ^*	OER Tafel slope in the Tafel-kinetic limit divided by $\ln(10)$	23	mV
k	Electrolyte proton conductivity	17	S/m
κ_1	Top electrode dimensionless number.	1×10^{-4}	1
κ_2	Bottom electrode dimensionless number.	10	1
θ	Charge transfer coefficient ratio.	3	1
β	Constant phase element exponent.	0.8	1
$\bar{\omega}$	Dimensionless frequency.	7×10^{-4}	1
χ	Ratio between the bottom electrode and top electrode capacitance.	0.1	1

Chapter 4
CONCLUSION

4.1 Summary

This work focuses on the framework of generating synthetic data from mechanistic modeling and leveraging machine learning to uncover underlying patterns. Our first objective is to garner insights into the proposed physics and advise data processing and implementation of electrochemical techniques, without needing extensive experimentation. The second objective is to validate the simulation-informed machine learning models with experimental data to test their applicability. We shall review of these objectives within the specific scopes of our studies and propose avenues for future work.

In Chapter 2, we found that the three different solid oxide fuel cell (SOFC) failure modes (fuel starvation, delamination and gas crossover) are identifiable from synthetic electrochemical impedance spectroscopy (EIS) with support vector machine (SVM) models. To our knowledge, SOFC failures have been a focus of few simulation works,[93–95] so we hope these mechanistic models are helpful to researchers who are interested in the topic. We've shared on GitHub the COMSOL models of nominal planar SOFC and the studied failures to facilitate future use and feedback.[122] Our model's success in identifying failure was dependent upon having information of the nominal system response, which were provided as simulated EIS at the operating condition with a fixed set of physics parameters. Similarly, other diagnostics application can explore the benefits of using a standard state response, generated either through simulation or experimentation. Identifying relevant frequencies with simulation-informed machine learning as we was able to from SVM coefficients, can help reduce dataset dimensionality and the number of EIS frequencies in design of experiments. However, since the work did not extend to experimental data validation, we remain cautious

about the applicability of the developed diagnostic tool.

In Chapter 3, we successfully predicted the oxygen evolution reaction (OER) loss using multi-layer perceptron neural networks with synthetic polarization measurements of an extended reference electrode on a proton exchange membrane (PEM) electrolyzer. The sensitivity analysis and permutation feature importance proved valuable in guiding experimentation decisions, leading to the exclusion of measurements from cathode-overhang reference and the suggestion to incorporate lower current density points. We validated our surrogate model with experimental data from three different electrolyzer cells, attaining reasonable OER overpotential prediction compared to literature. The promising results encourage further validation with more comprehensive experimentation. Additionally, intriguing behaviors observed in EIS experiments and simulations sparked our interests in further exploration. One potential avenue involves the development of a machine learning classifier to label EIS features to the half-cell they originate from, utilizing synthetic training data of half-cell EIS with different number of capacitors or constant phase elements per electrode.

4.2 Outlook

The increasing deployment of larger fuel cell and electrolysis systems spurs the demand for advanced state-of-health monitoring to maximize and optimize usage, or for safety and reliability. Steady-state polarization curves and transient voltage-current responses have been widely utilized to inform control and management systems, and most often reported in failure and degradation studies[15,81–83,178,179]. Furthermore, corresponding steady-state and transient models of fuel cells and electrolyzers has been thoroughly investigated.[111,180–187] The prevalence of steady-state and transient voltage-current data and modeling presents many opportunities for similar simulation-informed machine learning development to act as surrogate for computationally-expensive physics-models. Other analytical techniques such as EIS, thermography,[188–191] magnetotomography,[179,192–194] can offer more advanced information about the electrochemical systems. However, the complex analysis associated and the

uncertainty in their efficacy could prevent deployment. These concerns may be addressed by using simulation-informed machine learning to survey the suitability of the analytical technique and inform the design of diagnostic protocol.

BIBLIOGRAPHY

1. Barsoukov, E. & Macdonald, R. *Impedance Spectroscopy Theory, Experiment, and Applications* doi:10.1002/0471716243.fmatter (Wiley-Interscience, Hoboken, NJ, USA, Jan. 2005).

2. Ross Macdonald, J. *Impedance Spectroscopy: Emphasizing Solid Materials and Systems* 305 (Wiley, New York, 1992).

3. Orazem, M. E. & Tribollet, B. *Electrochemical Impedance Spectroscopy* (Wiley, Apr. 2017).

4. Lazanas, A. C. & Prodromidis, M. I. Electrochemical Impedance Spectroscopy-A Tutorial. en. *ACS Meas Sci Au* **3,** 162–193. doi:10.1021/acsmeasuresciau.2c00070 (June 2023).

5. Kavaliuke, V. *et al.* Combined conductivity and electrochemical impedance spectroscopy study of Na2FeP2O7 cathode material for sodium ion batteries. *Solid State Ionics* **385,** 116024. doi:10.1016/j.ssi.2022.116024 (Nov. 2022).

6. Lanfredi, S. & Rodrigues, A. C. M. Impedance spectroscopy study of the electrical conductivity and dielectric constant of polycrystalline LiNbO3. en. *J. Appl. Phys.* **86,** 2215–2219. doi:10.1063/1.371033 (Aug. 1999).

7. Liu, H., Tao, H. B. & Liu, B. Kinetic Insights of Proton Exchange Membrane Water Electrolyzer Obtained by Operando Characterization Methods. en. *J. Phys. Chem. Lett.* **13,** 6520–6531. doi:10.1021/acs.jpclett.2c01341 (July 2022).

8. Liu, Y. *et al.* Proton Conduction and Oxygen Reduction Kinetics in PEM Fuel Cell Cathodes: Effects of Ionomer-to-Carbon Ratio and Relative Humidity. en. *J. Electrochem. Soc.* **156,** B970. doi:10.1149/1.3143965 (June 2009).

9. Lenz, M., Zabel, J. & Franzreb, M. New Approach for Investigating Diffusion Kinetics Within Capacitive Deionization Electrodes Using Electrochemical Impedance Spectroscopy. *Frontiers in Materials* **7.** doi:10.3389/fmats.2020.00229 (2020).

10. Vedalakshmi, R., Devi, R. R., Emmanuel, B. & Palaniswamy, N. Determination of diffusion coefficient of chloride in concrete: an electrochemical impedance spectroscopic approach. *Mater. Struct.* **41,** 1315–1326. doi:10.1617/s11527-007-9330-1 (Aug. 2008).

11. Cruz-Manzo, S. & Greenwood, P. Low frequency inductive loop in EIS measurements of an open-cathode polymer electrolyte fuel cell stack. Impedance of water vapour diffusion in the cathode catalyst layer. *J. Electroanal. Chem.* **900,** 115733. doi:10.1016/j.jelechem.2021.115733 (Nov. 2021).

12. Mc Carthy, K., Gullapalli, H. & Kennedy, T. Real-time internal temperature estimation of commercial Li-ion batteries using online impedance measurements. *J. Power Sources* **519,** 230786. doi:10.1016/j.jpowsour.2021.230786 (Jan. 2022).

13. Galeotti, M., Cinà, L., Giammanco, C., Cordiner, S. & Di Carlo, A. Performance analysis and SOH (state of health) evaluation of lithium polymer batteries through electrochemical impedance spectroscopy. *Energy* **89,** 678–686. doi:10.1016/j.energy.2015.05.148 (Sept. 2015).

14. Zheng, Z. *et al.* A double-fuzzy diagnostic methodology dedicated to online fault diagnosis of proton exchange membrane fuel cell stacks. *J. Power Sources* **271,** 570–581. doi:10.1016/j.jpowsour.2014.07.157 (Dec. 2014).

15. Gallo, M., Polverino, P., Mougin, J., Morel, B. & Pianese, C. Coupling electrochemical impedance spectroscopy and model-based aging estimation for solid oxide fuel cell stacks lifetime prediction. *Appl. Energy* **279,** 115718. doi:10.1016/j.apenergy.2020.115718 (Dec. 2020).

16. Suboti, V. *et al.* On the origin of degradation in fuel cells and its fast identification by applying unconventional online-monitoring tools. *Appl. Energy* **277,** 115603. doi:10.1016/j.apenergy.2020.115603 (Nov. 2020).

17. Subotic, V. *et al.* Towards a practical tool for online monitoring of solid oxide fuel cell operation: An experimental study and application of advanced data analysis approaches. *Appl. Energy* **222,** 748–761. doi:10.1016/j.apenergy.2018.03.182 (July 2018).

18. Suboti, V. *et al.* Online monitoring tools for SoH diagnostic and prognostic of remaining lifetime of reversible solid oxide cell (rSOC) systems. *Energy Procedia* **158,** 2329–2334. doi:10.1016/j.egypro.2019.01.271 (Feb. 2019).

19. Sadeghi, E., Gholami, M. M., Hamzeh, M., Alavi, S. M. M. & Saif, M. A systematic overview of power electronics interfaced electrochemical impedance spectroscopy for energy storage systems. *Journal of Energy Storage* **62,** 106850. doi:10.1016/j.est.2023.106850 (June 2023).

20. Lyu, Z. *et al.* Prediction of fuel cell performance degradation using a combined approach of machine learning and impedance spectroscopy. *J. Mater. Chem. A Mater. Energy Sustain.* **87,** 32–41. doi:10.1016/j.jechem.2023.08.028 (Dec. 2023).

21. *The modified inductance element La* en. https://www.biologic.net/documents/battery-eis-modified-inductance-element-electrochemsitry-application-note-42/. Accessed: 2023-10-29. Aug. 2019.

22. Shoar Abouzari, M. R., Berkemeier, F., Schmitz, G. & Wilmer, D. On the physical interpretation of constant phase elements. *Solid State Ionics* **180,** 922–927. doi:10.1016/j.ssi.2009.04.002 (June 2009).

23. Córdoba-Torres, P., Keddam, M. & Nogueira, R. P. On the intrinsic electrochemical nature of the inductance in EIS: A Monte Carlo simulation of the two-consecutive-step

mechanism: The flat surface 2 D case. *Electrochim. Acta* **54,** 518–523. doi:10.1016/j.electacta.2008.07.023 (Dec. 2008).

24. Interpretation of the Gerischer impedance in solid state ionics. *Solid State Ionics* **157,** 29–33. doi:10.1016/S0167-2738(02)00185-6 (Feb. 2003).

25. Lu, Y., Kreller, C. & Adler, S. B. Measurement and Modeling of the Impedance Characteristics of Porous La1 x Sr x CoO3 Electrodes. en. *J. Electrochem. Soc.* **156,** B513. doi:10.1149/1.3079337 (Feb. 2009).

26. Huang, J. *et al.* Review - Impedance Response of Porous Electrodes: Theoretical Framework, Physical Models and Applications. en. *J. Electrochem. Soc.* **167,** 166503. doi:10.1149/1945-7111/abc655 (Nov. 2020).

27. Obermaier, M., Bandarenka, A. S. & Lohri-Tymozhynsky, C. A Comprehensive Physical Impedance Model of Polymer Electrolyte Fuel Cell Cathodes in Oxygen-free Atmosphere. en. *Sci. Rep.* **8,** 4933. doi:10.1038/s41598-018-23071-5 (Mar. 2018).

28. Chen, B.-R. *et al.* A mathematical approach to survey electrochemical impedance spectroscopy for aging in lithium-ion batteries. *Frontiers in Energy Research* **11.** doi:10.3389/fenrg.2023.1132876 (2023).

29. Liu, J. & Ciucci, F. The Gaussian process distribution of relaxation times: A machine learning tool for the analysis and prediction of electrochemical impedance spectroscopy data. *Electrochim. Acta* **331,** 135316. doi:10.1016/j.electacta.2019.135316 (Jan. 2020).

30. Meddings, N. *et al.* Application of electrochemical impedance spectroscopy to commercial Li-ion cells: A review. *J. Power Sources* **480,** 228742. doi:10.1016/j.jpowsour.2020.228742 (Dec. 2020).

31. Macdonald, D. D. Reflections on the history of electrochemical impedance spectroscopy. *Electrochim. Acta* **51,** 1376–1388. doi:10.1016/j.electacta.2005.02.107 (Jan. 2006).

32. Bessler, W. G. & Gewies, S. Gas Concentration Impedance of Solid Oxide Fuel Cell Anodes: II. Channel Geometry. en. *J. Electrochem. Soc.* **154,** B548. doi:10.1149/1.2720639 (Apr. 2007).

33. Murbach, M. D. & Schwartz, D. T. Extending Newman's Pseudo-Two-Dimensional Lithium-Ion Battery Impedance Simulation Approach to Include the Nonlinear Harmonic Response. en. *J. Electrochem. Soc.* **164,** E3311. doi:10.1149/2.0301711jes (June 2017).

34. Schneider, I. A., Bayer, M. H., Wokaun, A. & Scherer, G. G. Impedance Response of the Proton Exchange Membrane in Polymer Electrolyte Fuel Cells. en. *J. Electrochem. Soc.* **155,** B783. doi:10.1149/1.2929823 (June 2008).

35. Setzler, B. P. & Fuller, T. F. A Physics-Based Impedance Model of Proton Exchange Membrane Fuel Cells Exhibiting Low-Frequency Inductive Loops. en. *J. Electrochem. Soc.* **162,** F519. doi:10.1149/2.0361506jes (Mar. 2015).

36. Ender, M., Illig, J. & Ivers-Tiffée, E. Three-Electrode Setups for Lithium-Ion Batteries. I. Fem-Simulation of Different Reference Electrode Designs and Their Implications for Half-Cell Impedance Spectra. en. *J. Electrochem. Soc.* **164,** A71. doi:10.1149/2.0231702jes (Dec. 2016).

37. Duan, X., Liu, F., Agar, E. & Jin, X. Parameter Identification of Lithium-Ion Batteries by Coupling Electrochemical Impedance Spectroscopy with a Physics-Based Model. en. *J. Electrochem. Soc.* **169,** 040561. doi:10.1149/1945-7111/ac682f (Apr. 2022).

38. Chen, C.-H. *et al.* Development of Experimental Techniques for Parameterization of Multi-scale Lithium-ion Battery Models. en. *J. Electrochem. Soc.* **167,** 080534. doi:10.1149/1945-7111/ab9050 (May 2020).

39. Tran, N. T. *et al.* A Padé Approximate Model of Lithium Ion Batteries. en. *J. Electrochem. Soc.* **165,** A1409. doi:10.1149/2.0651807jes (May 2018).

40. Lin, M. *et al.* Lithium-ion battery degradation trajectory early prediction with synthetic dataset and deep learning. *J. Mater. Chem. A Mater. Energy Sustain.* **85,** 534–546. doi:10.1016/j.jechem.2023.06.036 (Oct. 2023).

41. Severson, K. A. *et al.* Data-driven prediction of battery cycle life before capacity degradation. en. *Nature Energy* **4,** 383–391. doi:10.1038/s41560-019-0356-8 (Mar. 2019).

42. Zhang, Y. *et al.* Identifying degradation patterns of lithium ion batteries from impedance spectroscopy using machine learning. en. *Nat. Commun.* **11,** 1706. doi:10.1038/s41467-020-15235-7 (Apr. 2020).

43. Love, C. T., Virji, M. B. V., Rocheleau, R. E. & Swider-Lyons, K. E. State-of-health monitoring of 18650 4S packs with a single-point impedance diagnostic. *J. Power Sources* **266,** 512–519. doi:10.1016/j.jpowsour.2014.05.033 (Nov. 2014).

44. Lyu, Z., Li, H., Wang, Y. & Han, M. Performance degradation of solid oxide fuel cells analyzed by evolution of electrode processes under polarization. *J. Power Sources* **485,** 229237. doi:10.1016/j.jpowsour.2020.229237 (Feb. 2021).

45. Zhu, S. *et al.* Equivalent circuit model recognition of electrochemical impedance spectroscopy via machine learning. *J. Electroanal. Chem.* **855,** 113627. doi:10.1016/j.jelechem.2019.113627 (Dec. 2019).

46. Buteau, S. & Dahn, J. R. Analysis of Thousands of Electrochemical Impedance Spectra of Lithium-Ion Cells through a Machine Learning Inverse Model. en. *J. Electrochem. Soc.* **166,** A1611. doi:10.1149/2.1051908jes (May 2019).

47. Zhao, Z. *et al.* EIS equivalent circuit model prediction using interpretable machine learning and parameter identification using global optimization algorithms. *Electrochim. Acta* **418,** 140350. doi:10.1016/j.electacta.2022.140350 (June 2022).

48. Schaeffer, J. *et al.* Machine Learning Benchmarks for the Classification of Equivalent Circuit Models from Electrochemical Impedance Spectra. en. *J. Electrochem. Soc.* **170,** 060512. doi:10.1149/1945-7111/acd8fb (June 2023).

49. Khameneh, M. K. & Babaei, A. Co-electrolysis of CO2 and H2O on LaFe0.6Co0.4O3 promoted La0.75Sr0.25Cr0.5Mn0.5O3/YSZ electrode in solid oxide electrolysis cell. *Electrochim. Acta* **299,** 132–142. doi:10.1016/j.electacta.2018.12.136 (Mar. 2019).

50. Boukamp, B. A. & Rolle, A. Analysis and Application of Distribution of Relaxation Times in Solid State Ionics. *Solid State Ionics* **302,** 12–18. doi:10.1016/j.ssi.2016.10.009 (Apr. 2017).

51. Wang, Q. *et al.* A comparative study of equivalent circuit model and distribution of relaxation times for fuel cell impedance diagnosis. en. *Int. J. Energy Res.* **45,** 15948–15961. doi:10.1002/er.6825 (Sept. 2021).

52. Xia, J., Wang, C., Wang, X., Bi, L. & Zhang, Y. A perspective on DRT applications for the analysis of solid oxide cell electrodes. *Electrochim. Acta* **349,** 136328. doi:10.1016/j.electacta.2020.136328 (July 2020).

53. Huang, J., Sullivan, N. P., Zakutayev, A. & O'Hayre, R. How reliable is distribution of relaxation times (DRT) analysis? A dual regression-classification perspective on DRT estimation, interpretation, and accuracy. *Electrochim. Acta* **443,** 141879. doi:10.1016/j.electacta.2023.141879 (Mar. 2023).

54. Effat, M. B. & Ciucci, F. Bayesian and Hierarchical Bayesian Based Regularization for Deconvolving the Distribution of Relaxation Times from Electrochemical Impedance Spectroscopy Data. *Electrochim. Acta* **247,** 1117–1129. doi:10.1016/j.electacta.2017.07.050 (Sept. 2017).

55. Liu, J. & Ciucci, F. The Deep-Prior Distribution of Relaxation Times. en. *J. Electrochem. Soc.* **167,** 026506. doi:10.1149/1945-7111/ab631a (Jan. 2020).

56. Py, B., Maradesa, A. & Ciucci, F. Gaussian processes for the analysis of electrochemical impedance spectroscopy data: Prediction, filtering, and active learning. *Electrochim. Acta* **439,** 141688. doi:10.1016/j.electacta.2022.141688 (Jan. 2023).

57. Huang, J., Papac, M. & O'Hayre, R. Towards robust autonomous impedance spectroscopy analysis: A calibrated hierarchical Bayesian approach for electrochemical impedance spectroscopy (EIS) inversion. *Electrochim. Acta* **367,** 137493. doi:10.1016/j.electacta.2020.137493 (Jan. 2021).

58. Faraji-Niri, M. *et al.* Accelerated state of health estimation of second life lithium-ion batteries via electrochemical impedance spectroscopy tests and machine learning techniques. *Journal of Energy Storage* **58,** 106295. doi:10.1016/j.est.2022.106295 (Feb. 2023).

59. Wimarshana, B., Bin-Mat-Arishad, I. & Fly, A. Parameter sensitivity analysis of a physico-chemical lithium-ion battery model with combined discharge voltage and electrochemical impedance data. *J. Power Sources* **527,** 231125. doi:10.1016/j.jpowsour.2022.231125 (Apr. 2022).

60. Babaeiyazdi, I., Rezaei-Zare, A. & Shokrzadeh, S. State of charge prediction of EV Li-ion batteries using EIS: A machine learning approach. *Energy* **223,** 120116. doi:10.1016/j.energy.2021.120116 (May 2021).

61. Sin, S. *et al. Data-driven prediction of battery degradation using EIS-based robust features* in *2022 IEEE Energy Conversion Congress and Exposition (ECCE)* (IEEE, Oct. 2022), 1–5. doi:10.1109/ECCE50734.2022.9947788.

62. Lu, Z. Computational discovery of energy materials in the era of big data and machine learning: A critical review. *Materials Reports: Energy* **1,** 100047. doi:10.1016/j.matre.2021.100047 (Aug. 2021).

63. Kang, Y., Li, L. & Li, B. Recent progress on discovery and properties prediction of energy materials: Simple machine learning meets complex quantum chemistry. *J.*

Mater. Chem. A Mater. Energy Sustain. **54,** 72–88. doi:10.1016/j.jechem.2020.05.044 (Mar. 2021).

64. Zahrt, A. F. *et al.* Machine-Learning-Guided Discovery of Electrochemical Reactions. en. *J. Am. Chem. Soc.* **144,** 22599–22610. doi:10.1021/jacs.2c08997 (Dec. 2022).

65. Tamtaji, M. *et al.* Machine learning for design principles for single atom catalysts towards electrochemical reactions. en. *J. Mater. Chem. A Mater. Energy Sustain.* **10,** 15309–15331. doi:10.1039/D2TA02039D (2022).

66. Pederson, R., Kalita, B. & Burke, K. Machine learning and density functional theory. en. *Nature Reviews Physics* **4,** 357–358. doi:10.1038/s42254-022-00470-2 (May 2022).

67. Mistry, A., Franco, A. A., Cooper, S. J., Roberts, S. A. & Viswanathan, V. How Machine Learning Will Revolutionize Electrochemical Sciences. en. *ACS Energy Lett* **6,** 1422–1431. doi:10.1021/acsenergylett.1c00194 (Apr. 2021).

68. Annevelink, E. *et al.* AutoMat: Automated materials discovery for electrochemical systems. *MRS Bull.* **47,** 1036–1044. doi:10.1557/s43577-022-00424-0 (Oct. 2022).

69. Rohr, B. *et al.* Benchmarking the acceleration of materials discovery by sequential learning. en. *Chem. Sci.* **11,** 2696–2706. doi:10.1039/c9sc05999g (Jan. 2020).

70. Duquesnoy, M. *et al.* Machine learning-assisted multi-objective optimization of battery manufacturing from synthetic data generated by physics-based simulations. *Energy Storage Materials* **56,** 50–61. doi:10.1016/j.ensm.2022.12.040 (Feb. 2023).

71. Lv, C. *et al.* Machine Learning: An Advanced Platform for Materials Development and State Prediction in Lithium-Ion Batteries. en. *Adv. Mater.* **34,** e2101474. doi:10.1002/adma.202101474 (June 2022).

72. Mayilvahanan, K. S., Takeuchi, K. J., Takeuchi, E. S., Marschilok, A. C. & West, A. C. Supervised learning of synthetic big data for Liion battery degradation diagnosis. en. *Batter. Supercaps* **5.** doi:10.1002/batt.202100166 (Jan. 2022).

73. Dubarry, M. & Beck, D. Analysis of Synthetic Voltage vs. Capacity Datasets for Big Data Li-ion Diagnosis and Prognosis. en. *Energies* **14,** 2371. doi:10.3390/en14092371 (Apr. 2021).

74. Dubarry, M. & Beck, D. Big data training data for artificial intelligence-based Li-ion diagnosis and prognosis. *J. Power Sources* **479,** 228806. doi:10.1016/j.jpowsour.2020.228806 (Dec. 2020).

75. Thelen, A. *et al.* Integrating physics-based modeling and machine learning for degradation diagnostics of lithium-ion batteries. *Energy Storage Materials* **50,** 668–695. doi:10.1016/j.ensm.2022.05.047 (Sept. 2022).

76. Zhang, G. *et al.* Optimization of porous media flow field for proton exchange membrane fuel cell using a data-driven surrogate model. *Energy Convers. Manage.* **226,** 113513. doi:10.1016/j.enconman.2020.113513 (Dec. 2020).

77. Guarino, A., Trinchero, R., Canavero, F. & Spagnuolo, G. A fast fuel cell parametric identification approach based on machine learning inverse models. *Energy* **239,** 122140. doi:10.1016/j.energy.2021.122140 (Jan. 2022).

78. Brandon, N. P., Ruiz-Trejo, E. & Boldrin, P. *Solid Oxide Fuel Cell Lifetime and Reliability: Critical Challenges in Fuel Cells* (Academic Press, May 2017).

79. Kadowaki, M. Current Status of National SOFC Projects in Japan. en. *ECS Trans.* **68,** 15. doi:10.1149/06801.0015ecst (June 2015).

80. Blum, L. *et al.* Long-term operation of solid oxide fuel cells and preliminary findings on accelerated testing. *Int. J. Hydrogen Energy* **45,** 8955–8964. doi:10.1016/j.ijhydene.2020.01.074 (Mar. 2020).

81. Comminges, C., Fu, Q. X., Zahid, M., Steiner, N. Y. & Bucheli, O. Monitoring the degradation of a solid oxide fuel cell stack during 10,000h via electrochemical impedance spectroscopy. *Electrochim. Acta* **59,** 367–375. doi:10.1016/j.electacta.2011.10.080 (Jan. 2012).

82. Blum, L. *et al.* Recent results in Jülich solid oxide fuel cell technology development. *J. Power Sources* **241,** 477–485. doi:10.1016/j.jpowsour.2013.04.110 (Nov. 2013).

83. Blum, L., Packbier, U., Vinke, I. C. & de Haart, L. G. J. Long-Term Testing of SOFC Stacks at Forschungszentrum Jülich. *Fuel Cells* **13,** 646–653. doi:10.1002/fuce.201200151 (Aug. 2013).

84. Klemenso, T. & Mogensen, M. NiYSZ solid oxide fuel cell anode behavior upon redox cycling based on electrical characterization. en. *J. Am. Ceram. Soc.* **90,** 3582–3588. doi:10.1111/j.1551-2916.2007.01909.x (Nov. 2007).

85. Faes, A., Hessler-Wyser, A., Zryd, A. & Van Herle, J. A Review of RedOx Cycling of Solid Oxide Fuel Cells Anode. en. *Membranes* **2,** 585–664. doi:10.3390/membranes2030585 (Aug. 2012).

86. Pan, J. *et al.* Effect of thermal cycling on durability of a solid oxide fuel cell stack with external manifold structure. *Int. J. Hydrogen Energy* **45,** 17927–17934. doi:10.1016/j.ijhydene.2020.04.260 (July 2020).

87. Khan, M. Z., Mehran, M. T., Song, R.-H., Lee, S.-B. & Lim, T.-H. Effects of applied current density and thermal cycling on the degradation of a solid oxide fuel cell cathode. *Int. J. Hydrogen Energy* **43,** 12346–12357. doi:10.1016/j.ijhydene.2018.04.175 (July 2018).

88. Menzler, N. H., Sebold, D. & Guillon, O. Post-test characterization of a solid oxide fuel cell stack operated for more than 30,000 hours: The cell. *J. Power Sources* **374,** 69–76. doi:10.1016/j.jpowsour.2017.11.025 (Jan. 2018).

89. Bianco, M., Ouweltjes, J. P. & Van herle, J. Degradation analysis of commercial interconnect materials for solid oxide fuel cells in stacks operated up to 18000 hours. *Int. J. Hydrogen Energy* **44,** 31406–31422. doi:10.1016/j.ijhydene.2019.09.218 (Nov. 2019).

90. Sarantaridis, D., Rudkin, R. A. & Atkinson, A. Oxidation failure modes of anode-supported solid oxide fuel cells. *J. Power Sources* **180,** 704–710. doi:10.1016/j.jpowsour.2008.03.011 (June 2008).

91. Madi, H. *et al.* Solid oxide fuel cell anode degradation by the effect of hydrogen chloride in stack and single cell environments. *J. Power Sources* **326,** 349–356. doi:10.1016/j.jpowsour.2016.07.003 (Sept. 2016).

92. Tian, J. & Milcarek, R. J. Investigating the degradation mechanism of the solid oxide fuel cell nickel-yttria stabilized zirconia anode under siloxane contamination. *J. Power Sources* **480,** 229122. doi:10.1016/j.jpowsour.2020.229122 (Dec. 2020).

93. Gazzarri, J. I. & Kesler, O. Non-destructive delamination detection in solid oxide fuel cells. *J. Power Sources* **167,** 430–441. doi:10.1016/j.jpowsour.2007.02.042 (May 2007).

94. Gazzarri, J. I. & Kesler, O. Electrochemical AC impedance model of a solid oxide fuel cell and its application to diagnosis of multiple degradation modes. *J. Power Sources* **167,** 100–110. doi:10.1016/j.jpowsour.2007.02.010 (May 2007).

95. Gazzarri, J. I. & Kesler, O. Short-stack modeling of degradation in solid oxide fuel cells: Part I. Contact degradation. *J. Power Sources* **176,** 138–154. doi:10.1016/j.jpowsour.2007.10.047 (Jan. 2008).

96. Huang, Q.-A., Hui, R., Wang, B. & Zhang, J. A review of AC impedance modeling and validation in SOFC diagnosis. *Electrochim. Acta* **52,** 8144–8164. doi:10.1016/j.electacta.2007.05.071 (Nov. 2007).

97. Gong, X., Dong, C., Xu, J., Wang, L. & Li, X. Machine learning assistance for electrochemical curve simulation of corrosion and its application. en. *Mater. Corros.* **71,** 474–484. doi:10.1002/maco.201911224 (Mar. 2020).

98. Zhang, Z., Li, S., Xiao, Y. & Yang, Y. Intelligent simultaneous fault diagnosis for solid oxide fuel cell system based on deep learning. *Appl. Energy* **233-234,** 930–942. doi:10.1016/j.apenergy.2018.10.113 (Jan. 2019).

99. Li, S., Cao, H. & Yang, Y. Data-driven simultaneous fault diagnosis for solid oxide fuel cell system using multi-label pattern identification. *J. Power Sources* **378,** 646–659. doi:10.1016/j.jpowsour.2018.01.015 (Feb. 2018).

100. Polverino, P., Pianese, C., Sorrentino, M. & Marra, D. Model-based development of a fault signature matrix to improve solid oxide fuel cell systems on-site diagnosis. *J. Power Sources* **280,** 320–338. doi:10.1016/j.jpowsour.2015.01.037 (Apr. 2015).

101. Wu, X. & Ye, Q. Fault diagnosis and prognostic of solid oxide fuel cells. *J. Power Sources* **321,** 47–56. doi:10.1016/j.jpowsour.2016.04.080 (July 2016).

102. Lee, J., Lin, L., Athe, P. & Dinh, N. Development of the Machine Learning-based Safety Significant Factor Inference Model for Diagnosis in Autonomous Control System. *Ann. Nucl. Energy* **162,** 108443. doi:10.1016/j.anucene.2021.108443 (Nov. 2021).

103. Khorasgani, H., Farahat, A., Ristovski, K., Gupta, C. & Biswas, G. Framework for unifying model-based and data-driven fault diagnosis. *Proc. Annu. Conf. Progn. Health Manag. Soc.* **10.** doi:10.36001/phmconf.2018.v10i1.530 (Sept. 2018).

104. Sobie, C., Freitas, C. & Nicolai, M. Simulation-driven machine learning: Bearing fault classification. *Mech. Syst. Signal Process.* **99,** 403–419. doi:10.1016/j.ymssp.2017.06.025 (Jan. 2018).

105. Benkouider, A. M., Kessas, R., Yahiaoui, A., Buvat, J. C. & Guella, S. A hybrid approach to faults detection and diagnosis in batch and semi-batch reactors by using EKF and neural network classifier. *J. Loss Prev. Process Indust.* **25,** 694–702. doi:10.1016/j.jlp.2012.03.005 (July 2012).

106. Deist, T. M. *et al.* Simulation-assisted machine learning. en. *Bioinformatics* **35,** 4072–4080. doi:10.1093/bioinformatics/btz199 (Oct. 2019).

107. Mastropasqua, L., Campanari, S. & Brouwer, J. Solid oxide fuel cell short stack performance testing - Part A: Experimental analysis and -combined heat and power unit comparison. *J. Power Sources* **371,** 225–237. doi:10.1016/j.jpowsour.2017.10.028 (Dec. 2017).

108. Nusev, G., Morel, B., Mougin, J., Juricic, D. & Boskoski, P. Condition monitoring of solid oxide fuel cells by fast electrochemical impedance spectroscopy: A case example of detecting deficiencies in fuel supply. *J. Power Sources* **489,** 229491. doi:10.1016/j.jpowsour.2021.229491 (Mar. 2021).

109. Campanari, S. & Iora, P. Comparison of finite volume SOFC models for the simulation of a planar cell geometry. en. *Fuel Cells* **5,** 34–51. doi:10.1002/fuce.200400057 (Feb. 2005).

110. Lai, K. *et al.* A quasi-two-dimensional electrochemistry modeling tool for planar solid oxide fuel cell stacks. *J. Power Sources* **196,** 3204–3222. doi:10.1016/j.jpowsour.2010.11.123 (Mar. 2011).

111. Shaffer, B. & Brouwer, J. Dynamic Model for Understanding Spatial Temperature and Species Distributions in Internal-Reforming Solid Oxide Fuel Cells. *J. Fuel Cell Sci. Technol.* **9.** doi:10.1115/1.4006477 (Aug. 2012).

112. Todd, B. & Young, J. B. Thermodynamic and transport properties of gases for use in solid oxide fuel cell modelling. *J. Power Sources* **110,** 186–200. doi:10.1016/S0378-7753(02)00277-X (July 2002).

113. Kee, R. J. *Chemically reacting flow: theory and practice* (J. Wiley, New York, 2003).

114. Franssen, J.-M. & Real, P. V. *Fire Design of Steel Structures* 319–345. doi:10.1002/9783433601570 (Wiley, Weinheim, Germany, June 2013).

115. Yuan, J., Rokni, M. & Sunden, B. Three-dimensional computational analysis of gas and heat transport phenomena in ducts relevant for anode-supported solid oxide fuel cells. en. *Int. J. Heat Mass Transf.* **46,** 809–821. doi:10.1016/s0017-9310(02)00357-5 (Feb. 2003).

116. Vargaftik, N. B., Filippov, L. P., Tarzimanov, A. A., Totskii, E. E. & Gorshkov, Y. A. *Handbook of Thermal Conductivity of Liquids and Gases* 1st Edition. doi:10.1201/9781003069287 (CRC Press, Nov. 2020).

117. Murshed, A. M., Huang, B. & Nandakumar, K. Control relevant modeling of planer solid oxide fuel cell system. *J. Power Sources* **163,** 830–845. doi:10.1016/j.jpowsour.2006.09.080 (Jan. 2007).

118. Chaisantikulwat, A., Diaz-Goano, C. & Meadows, E. S. Dynamic modelling and control of planar anode-supported solid oxide fuel cell. *Comput. Chem. Eng.* **32,** 2365–2381. doi:10.1016/j.compchemeng.2007.12.003 (Oct. 2008).

119. Cheddie, D. F. & Munroe, N. D. H. A dynamic 1D model of a solid oxide fuel cell for real time simulation. *J. Power Sources* **171,** 634–643. doi:10.1016/j.jpowsour.2007.06.170 (Sept. 2007).

120. Wilson, J. R., Schwartz, D. T. & Adler, S. B. Nonlinear electrochemical impedance spectroscopy for solid oxide fuel cell cathode materials. *Electrochim. Acta* **51,** 1389–1402. doi:10.1016/j.electacta.2005.02.109 (Jan. 2006).

121. Hill, T. A., Fackrell, J. E., Dubal, M. R. & Stiff, S. M. Understanding the consequences of CO2 leakage downstream of the capture plant. *Energy Procedia* **4,** 2230–2237. doi:10.1016/j.egypro.2011.02.111 (Jan. 2011).

122. Le, G. *SOFC_COMSOL_model: Compilation of different physics-based models of solid oxide fuel cell* en. https://github.com/giangtle/SOFC_COMSOL_model. Accessed: 2023-11-17.

123. Sobol, I. M. On the distribution of points in a cube and the approximate evaluation of integrals. *USSR Computational Mathematics and Mathematical Physics* **7,** 86–112. doi:10.1016/0041-5553(67)90144-9 (Jan. 1967).

124. Herman, J. & Usher, W. SALib: An open-source Python library for Sensitivity Analysis. *J. Open Source Softw.* **2,** 97. doi:10.21105/joss.00097 (Jan. 2017).

125. An, G. The Effects of Adding Noise During Backpropagation Training on a Generalization Performance. *Neural Comput.* **8,** 643–674. doi:10.1162/neco.1996.8.3.643 (Apr. 1996).

126. Bishop, C. M. Training with Noise is Equivalent to Tikhonov Regularization. en. *Neural Comput.* **7,** 108–116. doi:10.1162/neco.1995.7.1.108 (Jan. 1995).

127. Grandvalet, Y., Canu, S. & Boucheron, S. Noise Injection: Theoretical Prospects. *Neural Comput.* **9,** 1093–1108. doi:10.1162/neco.1997.9.5.1093 (July 1997).

128. Guyon, I., Weston, J., Barnhill, S. & Vapnik, V. Gene Selection for Cancer Classification using Support Vector Machines. *Mach. Learn.* **46,** 389–422. doi:10.1023/A:1012487302797 (Jan. 2002).

129. Winkler, J., Hendriksen, P. V., Bonanos, N. & Mogensen, M. Geometric Requirements of Solid Electrolyte Cells with a Reference Electrode. en. *J. Electrochem. Soc.* **145,** 1184. doi:10.1149/1.1838436 (Apr. 1998).

130. Adler, S. B., Henderson, B. T., Wilson, M. A., Taylor, D. M. & Richards, R. E. Reference electrode placement and seals in electrochemical oxygen generators. *Solid State Ionics* **134,** 35–42. doi:10.1016/S0167-2738(00)00711-6 (Oct. 2000).

131. Adler, S. B. Reference Electrode Placement in Thin Solid Electrolytes. en. *J. Electrochem. Soc.* **149,** E166. doi:10.1149/1.1467368 (Apr. 2002).

132. He, W. & Van Nguyen, T. Edge Effects on Reference Electrode Measurements in PEM Fuel Cells. en. *J. Electrochem. Soc.* **151,** A185. doi:10.1149/1.1634272 (Jan. 2004).

133. Ohs, J. H., Sauter, U., Maass, S. & Stolten, D. The Effect of the Reference Electrode Position on the Measurement of Half Cell Polarization in Proton-Exchange Membrane Fuel Cells. en. *J. Electrochem. Soc.* **159,** F181. doi:10.1149/2.006207jes (July 2012).

134. Wiezell, K., Gode, P. & Lindbergh, G. Steady-State and EIS Investigations of Hydrogen Electrodes and Membranes in Polymer Electrolyte Fuel Cells: II. Experimental. en. *J. Electrochem. Soc.* **153,** A759. doi:10.1149/1.2172561 (Feb. 2006).

135. Szendrei, A., Sparks, T. D. & Virkar, A. Three and Four-Electrode Electrochemical Impedance Spectroscopy Studies Using Embedded Composite Thin Film Pseudo-Reference Electrodes in Proton Exchange Membrane Fuel Cells. en. *J. Electrochem. Soc.* **166,** F784. doi:10.1149/2.0771912jes (July 2019).

136. Li, G. & Pickup, P. G. Measurement of single electrode potentials and impedances in hydrogen and direct methanol PEM fuel cells. *Electrochim. Acta* **49,** 4119–4126. doi:10.1016/j.electacta.2004.04.005 (Sept. 2004).

137. Gerteisen, D. Realising a reference electrode in a polymer electrolyte fuel cell by laser ablation. *J. Appl. Electrochem.* **37,** 1447–1454. doi:10.1007/s10800-007-9352-y (Dec. 2007).

138. Hartig-WeiSS, A., Bernt, M., Siebel, A. & Gasteiger, H. A. A Platinum Micro-Reference Electrode for Impedance Measurements in a PEM Water Electrolysis Cell. en. *J. Electrochem. Soc.* **168,** 114511. doi:10.1149/1945-7111/ac3717 (Nov. 2021).

139. Brightman, E., Dodwell, J., van Dijk, N. & Hinds, G. In situ characterisation of PEM water electrolysers using a novel reference electrode. *Electrochem. commun.* **52,** 1–4. doi:10.1016/j.elecom.2015.01.005 (Mar. 2015).

140. Hinds, G. & Brightman, E. In situ mapping of electrode potential in a PEM fuel cell. *Electrochem. commun.* **17,** 26–29. doi:10.1016/j.elecom.2012.01.007 (Apr. 2012).

141. Bühre, L. V. *et al.* Application and Analysis of a Salt Bridge Reference Electrode Setup for PEM Water Electrolysis: Towards an Extended Voltage Loss Break Down. en. *J. Electrochem. Soc.* **169,** 124513. doi:10.1149/1945-7111/ac9ee1 (Dec. 2022).

142. Ender, M., Weber, A. & Ellen, I.-T. Analysis of Three-Electrode Setups for AC-Impedance Measurements on Lithium-Ion Cells by FEM simulations. en. *J. Electrochem. Soc.* **159,** A128. doi:10.1149/2.100202jes (Dec. 2011).

143. Gasper, P., Schiek, A., Smith, K., Shimonishi, Y. & Yoshida, S. Predicting battery capacity from impedance at varying temperature and state of charge using machine learning. *Cell Reports Physical Science* **3,** 101184. doi:10.1016/j.xcrp.2022.101184 (Dec. 2022).

144. Guo, J., Che, Y., Pedersen, K. & Stroe, D.-I. Battery impedance spectrum prediction from partial charging voltage curve by machine learning. *J. Mater. Chem. A Mater. Energy Sustain.* **79,** 211–221. doi:10.1016/j.jechem.2023.01.004 (Apr. 2023).

145. Naaz, F., Herle, A., Channegowda, J., Raj, A. & Lakshminarayanan, M. A generative adversarial networkbased synthetic data augmentation technique for battery condition evaluation. en. *Int. J. Energy Res.* **45,** 19120–19135. doi:10.1002/er.7013 (Oct. 2021).

146. Kim, S., Yi, Z., Chen, B.-R., Tanim, T. R. & Dufek, E. J. Rapid failure mode classification and quantification in batteries: A deep learning modeling framework. *Energy Storage Materials* **45,** 1002–1011. doi:10.1016/j.ensm.2021.07.016 (Mar. 2022).

147. Biggio, L., Bendinelli, T., Kulkarni, C. & Fink, O. Ageing-aware battery discharge prediction with deep learning. *Appl. Energy* **346,** 121229. doi:10.1016/j.apenergy.2023.121229 (Sept. 2023).

148. Padgett, E. *et al.* Catalyst Layer Resistance and Utilization in PEM Electrolysis. en. *J. Electrochem. Soc.* **170,** 084512. doi:10.1149/1945-7111/acee25 (Sept. 2023).

149. Liu, C., Wrubel, J., Padgett, E. & Bender, G. The impacts of membrane pinholes on PEM water electrolysis. *J. Power Sources* **581,** 233507. doi:10.1016/j.jpowsour.2023.233507 (Oct. 2023).

150. *Nafion Membrane Chart* en. https://www.fuelcellearth.com/nafion-membrane-chart/. Accessed: 2023-10-1.

151. Danilovic, N., Bender, G. & Weber, A. *H2NEW LTE: Performance and Benchmarking* https://www.hydrogen.energy.gov/pdfs/review21/p196b_danilovic_2021_p.pdf. Accessed: 2023-9-23.

152. Bender, G. *et al.* Initial approaches in benchmarking and round robin testing for proton exchange membrane water electrolyzers. *Int. J. Hydrogen Energy* **44,** 9174–9187. doi:10.1016/j.ijhydene.2019.02.074 (Apr. 2019).

153. Van Der Linden, F., Pahon, E., Morando, S. & Bouquain, D. A review on the Proton-Exchange Membrane Fuel Cell break-in physical principles, activation procedures, and characterization methods. *J. Power Sources* **575,** 233168. doi:10.1016/j.jpowsour.2023.233168 (Aug. 2023).

154. Gerhardt, M. R. *et al.* MethodPractices and Pitfalls in Voltage Breakdown Analysis of Electrochemical Energy-Conversion Systems. en. *J. Electrochem. Soc.* **168,** 074503. doi:10.1149/1945-7111/abf061 (July 2021).

155. O'Hayre, R., Cha, S.-W., Colella, W. & Prinz, F. B. *Fuel Cell Fundamentals* 3rd ed. doi:10.1002/9781119191766 (Wiley, May 2016).

156. Jerkiewicz, G. Standard and Reversible Hydrogen Electrodes: Theory, Design, Operation, and Applications. *ACS Catal.* **10,** 8409–8417. doi:10.1021/acscatal.0c02046 (Aug. 2020).

157. Umeda, M., Sayama, K., Maruta, T. & Inoue, M. Proton activity of Nafion 117 membrane measured from potential difference of hydrogen electrodes. *Ionics* **19,** 623–627. doi:10.1007/s11581-012-0791-z (Apr. 2013).

158. Barique, M. A., Tsuchida, E., Ohira, A. & Tashiro, K. Effect of Elevated Temperatures on the States of Water and Their Correlation with the Proton Conductivity of Nafion. en. *ACS Omega* **3,** 349–360. doi:10.1021/acsomega.7b01765 (Jan. 2018).

159. Sone, Y., Ekdunge, P. & Simonsson, D. Proton Conductivity of Nafion 117 as Measured by a FourElectrode AC Impedance Method. en. *J. Electrochem. Soc.* **143,** 1254. doi:10.1149/1.1836625 (Apr. 1996).

160. Aouali, F. Z. *et al.* Analytical modelling and experimental validation of proton exchange membrane electrolyser for hydrogen production. *Int. J. Hydrogen Energy* **42,** 1366–1374. doi:10.1016/j.ijhydene.2016.03.101 (Jan. 2017).

161. Falcão, D. S. & Pinto, A. M. F. R. A review on PEM electrolyzer modelling: Guidelines for beginners. *J. Clean. Prod.* **261,** 121184. doi:10.1016/j.jclepro.2020.121184 (July 2020).

162. Maier, M. *et al.* Mass transport in PEM water electrolysers: A review. *Int. J. Hydrogen Energy* **47,** 30–56. doi:10.1016/j.ijhydene.2021.10.013 (Jan. 2022).

163. Kreller, C. R. & Adler, S. Insight into Rate Limiting Mechanisms of Porous La1-xSrxCoO3- Electrodes through Nonlinear Electrochemical Impedance Spectroscopy (NLEIS). en. *ECS Trans.* **25,** 2743. doi:10.1149/1.3205835 (Sept. 2009).

164. Murbach, M. D., Hu, V. W. & Schwartz, D. T. Nonlinear Electrochemical Impedance Spectroscopy of Lithium-Ion Batteries: Experimental Approach, Analysis, and Initial Findings. en. *J. Electrochem. Soc.* **165,** A2758. doi:10.1149/2.0711811jes (Aug. 2018).

165. Wilson, J. R., Sase, M., Kawada, T. & Adler, S. B. Measurement of Oxygen Exchange Kinetics on Thin-Film La0.6Sr0.4CoO3 Using Nonlinear Electrochemical Impedance Spectroscopy. en. *Electrochem. Solid-State Lett.* **10,** B81. doi:10.1149/1.2710178 (Feb. 2007).

166. Fasmin, F. & Srinivasan, R. ReviewNonlinear Electrochemical Impedance Spectroscopy. en. *J. Electrochem. Soc.* **164,** H443. doi:10.1149/2.0391707jes (May 2017).

167. He, Y. Theoretical analysis of relative diffusion impedance in finite layer: Spiral-shaped Nyquist plots in electrochemical impedance spectroscopy. *AIP Adv.* **12.** doi:10.1063/5.0123313 (Nov. 2022).

168. Zhang, X.-Y., Trame, M. N., Lesko, L. J. & Schmidt, S. Sobol Sensitivity Analysis: A Tool to Guide the Development and Evaluation of Systems Pharmacology Models. en. *CPT Pharmacometrics Syst Pharmacol* **4,** 69–79. doi:10.1002/psp4.6 (Feb. 2015).

169. Breiman, L. Random Forests. *Mach. Learn.* **45,** 5–32. doi:10.1023/A:1010933404324 (Oct. 2001).

170. *Overview ELI5 0.11.0 documentation* en. https://eli5.readthedocs.io/en/latest/overview.html. Accessed: 2023-11-3.

171. Han, B., Steen, S. M., Mo, J. & Zhang, F.-Y. Electrochemical performance modeling of a proton exchange membrane electrolyzer cell for hydrogen energy. *Int. J. Hydrogen Energy* **40,** 7006–7016. doi:10.1016/j.ijhydene.2015.03.164 (June 2015).

172. Marangio, F., Santarelli, M. & Calì, M. Theoretical model and experimental analysis of a high pressure PEM water electrolyser for hydrogen production. *Int. J. Hydrogen Energy* **34,** 1143–1158. doi:10.1016/j.ijhydene.2008.11.083 (Feb. 2009).

173. Choi, P., Bessarabov, D. G. & Datta, R. A simple model for solid polymer electrolyte (SPE) water electrolysis. *Solid State Ionics* **175,** 535–539. doi:10.1016/j.ssi.2004.01.076 (Nov. 2004).

174. Harrison, K. W., Hernández-Pacheco, E., Mann, M. & Salehfar, H. Semiempirical Model for Determining PEM Electrolyzer Stack Characteristics. en. *J. Fuel Cell Sci. Technol.* **3,** 220–223. doi:10.1115/1.2174072 (Nov. 2005).

175. Babic, U., Schmidt, T. J. & Gubler, L. CommunicationContribution of Catalyst Layer Proton Transport Resistance to Voltage Loss in Polymer Electrolyte Water Electrolyzers. en. *J. Electrochem. Soc.* **165,** J3016. doi:10.1149/2.0031815jes (July 2018).

176. Neyerlin, K. C., Gu, W., Jorne, J. & Gasteiger, H. A. Study of the Exchange Current Density for the Hydrogen Oxidation and Evolution Reactions. en. *J. Electrochem. Soc.* **154,** B631. doi:10.1149/1.2733987 (May 2007).

177. Babic, U., Nilsson, E., Ptru, A., Schmidt, T. J. & Gubler, L. Proton Transport in Catalyst Layers of a Polymer Electrolyte Water Electrolyzer: Effect of the Anode Catalyst Loading. en. *J. Electrochem. Soc.* **166,** F214. doi:10.1149/2.0341904jes (Feb. 2019).

178. Gerard, M., Poirot-Crouvezier, J.-P., Hissel, D. & Péra, M.-C. Ripple Current Effects on PEMFC Aging Test by Experimental and Modeling. en. *J. Fuel Cell Sci. Technol.* **8,** 021004. doi:10.1115/1.4002467 (Nov. 2010).

179. Akimoto, Y., Izawa, Y., Suzuki, S.-N. & Okajima, K. Experimental investigation of stable the proton exchange membrane fuel cell control using magnetic sensor probes. en. *Fuel Cells* **22,** 2–11. doi:10.1002/fuce.202100057 (Apr. 2022).

180. Mueller, F., Brouwer, J., Jabbari, F. & Samuelsen, S. Dynamic Simulation of an Integrated Solid Oxide Fuel Cell System Including Current-Based Fuel Flow Control. en. *J. Fuel Cell Sci. Technol.* **3,** 144–154. doi:10.1115/1.2174063 (Oct. 2005).

181. Jiang, W., Fang, R., Dougal, R. A. & Khan, J. A. Thermoelectric Model of a Tubular SOFC for Dynamic Simulation. en. *J. Energy Res. Technol.* **130,** 022601. doi:10.1115/1.2906114 (May 2008).

182. Petruzzi, L., Cocchi, S. & Fineschi, F. A global thermo-electrochemical model for SOFC systems design and engineering. *J. Power Sources* **118,** 96–107. doi:10.1016/S0378-7753(03)00067-3 (May 2003).

183. Bhattacharyya, D. & Rengaswamy, R. A Review of Solid Oxide Fuel Cell (SOFC) Dynamic Models. *Ind. Eng. Chem. Res.* **48,** 6068–6086. doi:10.1021/ie801664j (July 2009).

184. Edwards, R. L. & Demuren, A. Regression analysis of PEM fuel cell transient response. *International Journal of Energy and Environmental Engineering* **7,** 329–341. doi:10.1007/s40095-016-0209-1 (Sept. 2016).

185. Natarajan, D. & Van Nguyen, T. A Two-Dimensional, Two-Phase, Multicomponent, Transient Model for the Cathode of a Proton Exchange Membrane Fuel Cell Using Conventional Gas Distributors. en. *J. Electrochem. Soc.* **148,** A1324. doi:10.1149/1.1415032 (Nov. 2001).

186. Adzakpa, K. P. *et al.* PEM Fuel Cells Modeling and Analysis Through Current and Voltage Transient Behaviors. *IEEE Trans. Energy Convers.* **23,** 581–591. doi:10.1109/TEC.2007.914170 (June 2008).

187. Sedghisigarchi, K. & Feliachi, A. Dynamic and transient analysis of power distribution systems with fuel Cells-part I: fuel-cell dynamic model. *IEEE Trans. Energy Convers.* **19,** 423–428. doi:10.1109/TEC.2004.827039 (June 2004).

188. Obeisun, O. A. *et al.* Study of water accumulation dynamics in the channels of an open-cathode fuel cell through electro-thermal characterisation and droplet visualisation. *Int. J. Hydrogen Energy* **40,** 16786–16796. doi:10.1016/j.ijhydene.2015.07.066 (Dec. 2015).

189. Rosso, L., Fernicola, V. & Pedrazzo, F. Multi-channel Optical Fiber Thermometer for PEM Fuel-Cell Applications. *Int. J. Thermophys.* **32,** 1440–1447. doi:10.1007/s10765-011-0976-0 (Aug. 2011).

190. Wilkinson, M. *et al.* In Situ Experimental Technique for Measurement of Temperature and Current Distribution in Proton Exchange Membrane Fuel Cells. en. *Electrochem. Solid-State Lett.* **9,** A507. doi:10.1149/1.2338769 (Aug. 2006).

191. Meyer, Q., Zeng, Y. & Zhao, C. In Situ and Operando Characterization of Proton Exchange Membrane Fuel Cells. en. *Adv. Mater.* **31,** e1901900. doi:10.1002/adma.201901900 (Oct. 2019).

192. Ifrek, L. *et al.* Fault detection for polymer electrolyte membrane fuel cell stack by external magnetic field. *Electrochim. Acta* **313,** 141–150. doi:10.1016/j.electacta.2019.04.193 (Aug. 2019).

193. Hauer, K.-H., Potthast, R., Wüster, T. & Stolten, D. Magnetotomographya new method for analysing fuel cell performance and quality. *J. Power Sources* **143,** 67–74. doi:10.1016/j.jpowsour.2004.11.054 (Apr. 2005).

194. Liu, Z. *et al.* Efficient fault diagnosis of proton exchange membrane fuel cell using external magnetic field measurement. *Energy Convers. Manage.* **266,** 115809. doi:10.1016/j.enconman.2022.115809 (Aug. 2022).